

Ultrasonic Imaging and Therapy using Microbubbles for Deep Vein Thrombosis

A
Dissertation
Presented to
the faculty of the School of Engineering and Applied Science
University of Virginia

in partial fulfillment
of the requirements for the degree

Doctor of Philosophy

by

Yanjun Xie

August 2024

APPROVAL SHEET

This
Dissertation
is submitted in partial fulfillment of the requirements
for the degree of
Doctor of Philosophy

Author: Yanjun Xie



This Dissertation has been read and approved by the examining committee:

Advisor: John A. Hossack

Advisor:

Committee Member: Craig H. Meyer

Committee Member: Alexander L. Klibanov

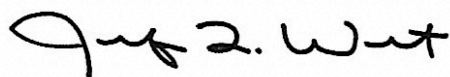
Committee Member: Bowen Wang

Committee Member: Kelsey P. Kubelick

Committee Member:

Committee Member:

Accepted for the School of Engineering and Applied Science:



Jennifer L. West, School of Engineering and Applied Science

August 2024

ABSTRACT

Sonothrombolysis is a therapeutic technique that combines ultrasound, thrombolytic agents and microbubbles to facilitate the dissolution of thrombi. In exposure to ultrasound, microbubbles exhibit therapeutic functions as a result of cavitation or drug delivery. Sonothrombolysis is being explored as an alternative therapy for deep vein thrombosis (DVT), as it can induce bio-effects and lower the risk of bleeding. Microfluidics techniques can generate microbubbles of adjustable diameter and stability. Transiently stable microbubbles have been examined for their ability of recanalization. In this dissertation, sonothrombolysis for DVT using microfluidically produced microbubbles is evaluated in terms of safety and effectiveness. Additionally, ultrasound imaging techniques are applied for the assessment of DVT.

For real-time monitoring of microbubbles to avoid failure cases, a closed-loop feedback control system was implemented in a flow-focusing microfluidic device with integrated on-chip electrodes. The diameter of microbubbles and the production rate were derived from the impedance variations caused by the passage of microbubbles. This measurement method was consistent with the optical diameter benchmark ($R^2 = 0.98$). A proportional-integral controller regulated the diameter of microbubbles in the range of 14 – 24 μm .

In experiments involving a murine model of DVT, a 3D ultrasound imaging approach was developed to quantify the volume of a thrombus. The volumes of fabricated blood clots were correlated with their weight in a flow system, with an R^2 of 0.89. A mouse

model of DVT in the inferior vena cava was imaged using 3D ultrasound, followed by macroscopic observation. The proposed approach was evaluated against macroscopic measurement, showing an R^2 of 0.91, and it was applicable to efficacy experiments.

Mice diagnosed with DVT were randomly divided into experimental and control groups. During therapy, microfluidically produced microbubbles of 18 μm diameter and recombinant tissue plasminogen activator were administered through a tail vein catheter for 30 minutes, while ultrasound was applied to the abdominal region of the mice in the sonothrombolysis group. The sonothrombolysis therapy significantly reduced the residual volume of thrombi to 20%, versus 52% without therapy ($p = 0.012 < 0.05$). The results suggest that large microbubbles produced using microfluidic techniques are effective therapeutic agents in sonothrombolysis.

The stiffness of a thrombus indicates its age and compositions. Ultrasound-based shear wave elastography offers an estimate of tissue stiffness through analysis of the propagation of shear waves. A Fourier feature network-based algorithm was designed to denoise displacement data and improve elasticity reconstruction in shear wave elastography. It was validated in phantom and *ex vivo* studies and shown to outperform a reference filtering method. After enhancement using this algorithm, the root mean square error and the structural similarity index of the reconstruction were 1.76 kPa and 0.949 compared to the ground truth, respectively.

Acknowledgments

Born in Guangzhou, a populated city in southern China, I spent part of my life living and conducting research in Charlottesville. My graduate study at the University of Virginia is a totally different experience from my previous ones.

I express my gratitude to my former and current lab colleagues, Mr. John-Marschner Robert Rickel, Dr. Sunil Unnikrishnan, Dr. Sushanth Govinahallisathyaranarayana, Dr. Adam J. Dixon, Dr. Elizabeth Herbst, Dr. Feifei Zhao and Mr. Yi Huang. Their mentorship and support to me have been indispensable in the completion of my projects and this dissertation in terms of microfluidics technology, ultrasound imaging and contrast agents. Not only in work, their suggestions inspired me to explore my life in Charlottesville. Playing basketball and snowboarding around C'ville have been the most enjoyable activities over the past few years. In addition to my lab, I also appreciate Dr. Li Yin, Dr. Kaijie Zhang and Mr. Jeremy Gatesman for their contributions to animal studies.

I would like to acknowledge my academic advisor Dr. John A. Hossack for his professional and educational mentorship. His guidance in my research and my career is irreplaceable. Through his personal example, I have learned the meticulous approach to writing, reviewing, and presenting. I appreciate my committee members, Dr. Alexander

L. Klibanov, Dr. Craig H. Meyer, Dr. Bowen Wang, and Dr. Kelsey P. Kubelick, for their valuable insights and expertise that greatly aided my projects. Their advice broadens my vision and influences my prospective beyond my own field, as these exchanges of ideas spark new ways of thinking.

I would like to thank my friend and roommate Quan Dou. He and his cat have been with me for the last few years. We have both dedicated ourselves to our studies for our degrees and witnessed our accomplishments.

Finally, I must thank my wife, Jiayong Li. Once she decided, she prepared for graduate school and boarded an oversea flight during the COVID-19 pandemic. The COVID-19 pandemic was an influential event for this generation, affecting the work and lifestyle of most people. Recollections from that period include weekly tests in the central garage, cautious shopping for groceries, and online classes. The routine of our daily lives eventually converted to our mutual commitments. I would also like to thank my parents. My parents have always been supportive of whatever my decision is. Without my family's backing, this dissertation would not have been possible.

This dissertation is funded by NIH R01 HL141752. The opinions presented in this dissertation only represent the perspectives of the authors and do not reflect the official view of the NIH.

Contents

ABSTRACT	i
ACKNOWLEDGMENTS	iii
LIST OF CONTENTS	3
LIST OF FIGURES	9
LIST OF TABLES	10
LIST OF NOMENCLATURE	11
1 INTRODUCTION	14
1.1 Ultrasound imaging and microbubbles	14
1.2 Microfluidically Produced Microbubbles	15
1.3 Deep Vein Thrombosis and Sonothrombolysis	17
1.4 Thrombus Imaging	18
1.5 Deep learning-enhanced Shear wave elastography	19
1.6 Dissertation Summary	20
2 REAL-TIME SIZE CONTROL OF MICROFLUIDICALLY PRODUCED MICROBUBBLES USING A MICRO COULTER COUNTER	22
2.1 Introduction	22
2.2 Methods	25
2.2.1 Device fabrication and microbubble production	25
2.2.2 Finite element analysis	27
2.2.3 Signal acquisition and signal processing	28
2.2.4 Closed-loop feedback control	31
2.3 Results	33

2.3.1	Microbubble production by FFMD	33
2.3.2	FEA results	34
2.3.3	Electrical detection of MB diameter	35
2.3.4	Characterization of FFMD feedback control system	36
2.3.5	Multiple step changes of diameter	41
2.4	Discussion	42
2.5	Conclusion	46
3	IN VIVO QUANTIFICATION OF DEEP VEIN THROMBOSIS USING HIGH-FREQUENCY ULTRASOUND IMAGING	48
3.1	Introduction	48
3.1.1	Deep Vein Thrombosis	48
3.2	Materials and Methods	50
3.2.1	<i>In Vitro</i> Blood Clot Model	50
3.2.2	Mouse Model of Deep Vein Thrombosis	52
3.2.3	Ultrasound Imaging	53
3.2.4	Three-dimensional Segmentation of Blood Clot	53
3.2.5	Data Analysis	55
3.3	Results	56
3.3.1	Three-dimensional blood clot volume and weight	56
3.3.2	Characterization of thrombus in mouse of IVC stenosis model	60
3.4	Discussion	60
3.5	Conclusions	64
4	EFFICACY OF IN VIVO SONOTHROMBOLYSIS USING MICROFLUIDICALLY PRODUCED MICROBUBBLES IN A MOUSE MODEL OF DEEP VEIN THROMBOSIS	65
4.1	Introduction	65
4.2	Methods	68
4.2.1	Fabrication of Microbubbles via Microfluidics	68
4.2.2	Ultrasound Imaging	70
4.2.3	Deliverability Study of Microfluidically Produced Microbubbles in Mice	71
4.2.4	Mouse Model of Deep Vein Thrombosis	71
4.2.5	Histology	74
4.2.6	Statistical Analysis	74
4.3	Results	74
4.3.1	Ultrasound Imaging Assessment of Microfluidically Produced Microbubbles in Mice	74

4.3.2	Mouse Model of DVT	75
4.3.3	Histology results	76
4.4	Discussion	79
5	SHEAR WAVE ELASTOGRAPHY ENHANCEMENT USING FOURIER FEATURE NETWORK	82
5.1	Introduction	82
5.2	Materials and Methods	85
5.2.1	Background and framework of SELFNet	85
5.2.2	Training of SELFNet	90
5.2.3	Data acquisition	91
5.2.4	Phantom and ex vivo tissues	92
5.2.5	Reconstruction	93
5.2.6	Quantification metrics	94
5.3	Results	95
5.3.1	Denosing displacement field	95
5.3.2	Reconstruction results	96
5.3.3	Ablation study	102
5.3.4	Ex vivo tissue results	102
5.4	Discussions	105
5.5	Conclusion	109
6	CONCLUSION AND FUTURE DIRECTIONS	112
6.1	Summary	112
6.2	Future directions	115
6.2.1	Evaluation of post thrombotic syndrome	116
6.2.2	Catheter for sonothrombolysis therapy	116
6.2.3	Dual function ultrasound for deep vein thrombosis	117
6.2.4	Model-based algorithms for ultrasound imaging	117
	PEER-REVIEWED JOURNAL PUBLICATIONS	120
	CONFERENCE ABSTRACTS AND PRESENTATIONS	122
	REFERENCES	125

List of Figures

2.1	Schematic of the closed-loop control flow-focusing microfluidic device (FFMD) system. (a) Working principle of the control system. A proportional-integral (PI) controller regulates input gas pressure based on the measured diameter. (b) The output of the Wheatstone bridge is amplified and connected to a data acquisition system. (c) Image of a benchtop FFMD with micro Coulter particle counter (μ CPC). (d) Produced microbubbles (MBs) traverse the detection region of electrodes. The other electrodes monitor the flooded situation inside the polydimethylsiloxane (PDMS) channel.	25
2.2	(a) Modulated MB signal and (b) a high-speed optical image of MBs were captured simultaneously. (c) Demodulated MB signal were acquired by absolute value of quadrature demodulation. The peaks of the demodulated signal were selected and averaged over the sampling. (d) Optically determined diameter vs. time-averaged maximum voltage.	29
2.3	finite element analysis (FEA) results of MBs travel through detection electrodes. (a) The traverse of a MB through detection region and moved close to the adjacent MB at three different locations. (b) The impedance of 16 and 20 μ m MB passage as described previously. (c) The impedance maxima of 14 to 26 μ m MBs were plotted.	30
2.4	An example of optical and corresponding demodulated electrical data. In (a), it took a MB approximate 13 frames to pass through the detection region (frame 8-21). The imaging speed was at 1 million frames per second, the rough production rate was 77 ± 3 kMBs/s. In (b), there were 56 local peaks in 716 μ s. The production rate using electrical counting was 77 kMBs/s.	32
2.5	Validation data of electrically determined diameter vs. optically determined diameter. $R^2 = 0.98$	35

2.6	Step responses of closed-loop control FFMD system with three different sets of parameters. (a) Increase from 18 to 20 μm . (b) Decrease from 20 to 18 μm	37
2.7	Step response (a) for setpoint of MB diameter changing from 18 to 20 μm and (b) from 20 to 18 μm with a Proportional controller. A variety of proportional gains (K_c) are implemented to determine the optimal proportional gain and integral time to be used in a Proportional-Integral controller.	38
2.8	Step responses of feedback control FFMD with various destination setpoints at flow rate of 22 $\mu\text{L}/\text{min}$ with $K_c = 0.045$ and $T_i = 3.3 \text{ s}$. (a) Measured diameter of different setpoint diameter from 18 μm . The dashed line is the setpoint diameter. (b) Relative measured input gas pressure over time. The lines correspond to the process with same line type and color in (a). (c) Change rate of relative pressure 15 to 36 s vs. setpoint diameter.	40
2.9	Feedback control with multiple steps of electrically determined diameter. (a) MB electrically determined diameters were increased from 18 to 24 μm by increments of 0.5 μm every 30 s. (b) MB electrically determined diameters were increased from 14 to 24 μm by increments of 2 μm every 30 s.	41
2.10	System response of a constant input gas pressure. The initial electrically determined diameter was 15.3 μm and the setpoint gas pressure was 77 kPa.	42
2.11	Comparisons between PI controlled and static input MB production. MB diameter was stabilized at 22 μm for 120 s, after which the system used the constant input flow rate and gas pressure of 103 kPa, in the top row. The same process repeated in the bottom row, but the initial diameter was 18 μm and the constant input gas pressure was 95.4 kPa.	43
3.1	Schematic of experiments and imaging setups. (a) An <i>in vitro</i> blood clots is fabricated and kept in refrigerator for 4 to 7 days. The weights of the blood clots are measured before running in a flow loop. The blood clots in whole bovine blood are imaged by a three-dimensional (3D) ultrasound system. (b) A mouse of inferior vena cava (IVC) stenosis model undergoes surgery at day 0. At day 3, the mouse is imaged using a 3D ultrasound system before sacrifice.	51

3.2	Workflow of the semi-automatic 3D segmentation. First, Ultrasound volume is loaded into 3D Slicer (I). Manual segmentation is performed in multiple slices and angles, based on B-mode signal density and Doppler blood flow signal in (II). A seeding algorithm is run and modifications are applied to extract a 3D volume of a blood clot in (IV). After the segmentation, the volume of the blood clot is calculated for quantifications.	54
3.3	The correlation plot of <i>In vitro</i> blood clot weights versus 3D segmentation volume, where $R^2 = 0.89$. The dashed line represents the linear regression result.	56
3.4	Photographic and ultrasonic examples of a bovine blood clot. (a) A photo of an <i>in vitro</i> blood clot. Each small tick of a ruler equals to 1 mm. (b) One slice across the corresponding 3D US volume approximates the previous photo in (a). This clot has a weight of 101 mg and a volume of 94.1 mm ³ . (c) The output segmentation volume of the clot is shown.	57
3.5	A correlation plot of <i>in vivo</i> results between volumetric measurement using ultrasound and macroscopic observation is plotted, with $R^2 = 0.91$. The dashed line is the linear fitting result.	58
3.6	Example of macroscopic photos and ultrasound imaging on day 3. Each row is the macroscopic photo (a, d, g), the ultrasound image (b, e, h), and the ultrasound image with an overlaid mask of the blood clot (c, f, i), of each mouse. Arrows indicate the location of the detected blood clots in macroscopic photos.	59
4.1	(a) Experiment timeline: the animals underwent surgery of partial ligation to develop thrombus on Day 0; 3D ultrasound imaging was performed on Day 3, followed by a therapy; Another 3D ultrasound imaging was conducted on Day 14. (b) Two-dimensional slices of both long axis and short axis view of the IVC were acquired at different vessel cross-sections. Data were exported to 3D Slicer software for segmentation. (c) A therapy to mouse model of deep vein thrombosis (DVT). Microfluidically produced MBs and thrombolytic drugs were administered through a tail vein catheter, while ultrasound was applied from the top of the mouse abdomen. Comparison of DVT in the IVC was shown in (d) and (e), on Days 3 and 14, respectively. The red region indicated the location of thrombus.	69
4.2	(a) Layout of a flow-focusing microfluidic device. G: gas inlet, L: liquid inlet. O: MB outlet. (b) A photo of generated MBs under a high speed camera. The mean diameter of MBs was 18.0 μm	70

4.3	Flow diagram of mice enrollment.	73
4.4	Ultrasound (US) images of IVC at (a) 0 s, (b) 100 s and (c) 360 s after administration of microfluidically produced MBs into the catheter. Cluster of MBs flow in the IVC in (a) and enhanced the image intensity inside the vein. The arrow in (b) shows a single MB traversing in the IVC. No MBs are detected after 360 s.	75
4.5	Representative ultrasound images in long-axis. The top and bottom rows are the results of Day 3 (a-d) and Day 14 (e-h), respectively. Each column is the same mouse from group A sonothrombolysis using microfluidically produced MBs (a, e), B ultrasound plus recombinant tissue plasminogen activator (rt-PA) (b, f), C rt-PA (c, g) and D no-therapy control (d, h). The red overlaid mask is the segmented blood clot. A scalebar of 2 mm is plotted.	76
4.6	Efficacy results of therapies. The residual volume of thrombus from Day 3 to Day 14 in percentage is plotted. The use of large microfluidically produced microbubbles reduces the residual volume of thrombus. The differences in the residual volume for MBs + US + rt-PA (group A) and the other groups (B: US + rt-PA; C: rt-PA and D: no-therapy control) are all statistically significant ($p < 0.05$, least significant difference (LSD) test). An asterisk denotes statistical significance of comparison to no-therapy control group D ($p < 0.05$). Additional statistical results are listed in the result section.	77
4.7	Hematoxylin and eosin (H&E) staining results in (a) MBs + US + rt-PA, (b) US + rt-PA, (C) rt-PA and (D) no-therapy control groups. Arrows in A-D show the recanalization channels in thrombus. The scale bar responds to 200 μm . H&E, haematoxylin and eosin; MB, microbubble; US, ultrasound; rt-PA, recombinant tissue plasminogen activator.	78

5.1	SELFNet architecture: the input spatial and temporal coordinates $[x, z; t]$ are encoded using Fourier feature embeddings (initialized with different σ) separately, and then the spatial and temporal featurized tensors go through a neural network θ_1 . Point-wise multiplication is applied to the spatial and temporal outputs, and the results are concatenated. The final particle displacement and related field are obtained through an additional linear layer. An auxiliary network θ_2 predicts the shear modulus by providing the spatial coordinates. The whole networks θ_1 and θ_2 are optimized by summation of data-driven loss ℓ_u and physics-informed residual loss ℓ_f , boundary condition loss ℓ_b . MLP: multilayer perceptron; FF: Fourier features.	90
5.2	Workflow for data acquisition and processing. A Verasonics Vantage 256 equipped with a L7-4 transducer was used to collect data on CIRS-049 phantom. The displacement data $w_{original}$ or w_{GT} were extracted from either 5- or 75-angle coherent plane wave compounded (CPWC) images using Loupas autocorrelator, respectively. The displacement data $w_{original}$ from 5-angle CPWC images were fed into a Shear wave ELastography Fourier feature Network (SELFNet) to predict the corrected displacement field \hat{w} . AC: autocorrelator; CPWC: coherent plane wave compounding; GT: ground truth.	93
5.3	Snapshots of normalized displacement field at 1, 2 and 3 ms, in a phantom of a type III lesion. Each row represents the ground-truth, original, Gaussian-filtered or SELFNet-predicted displacement signals. The red dot indicates the location of the point in Figure 4. The scale bar represents 2 mm. GT: ground-truth.	97
5.4	Axial displacement at $x = 8.8, z = 31$ mm from 0 to 5.2 ms. The original data are Gaussian filtered or trained using SELFNet. In comparisons with the ground truth, the relative ℓ_2 errors for the original, Gaussian-filtered, and SELFNet predicted displacement are 0.413, 0.223 and 0.159, respectively. The improved SNRs over the original data are 3.8 and 10.8 dB using a Gaussian filter and SELFNet approaches.	98
5.5	Reconstruction of elasticity mappings, where a type II lesion is included. The dash-dotted circle represents the location of the lesion. A 2 mm scale bar is plotted. Filter: Gaussian filter; MLP: multilayer perceptron; PINN: physics-informed neural network.	99

5.6	Reconstruction of elasticity mappings, where a type VI lesion is included. The dash-dotted circle represents the location of the lesion. A 2 mm scale bar is plotted. Filter: Gaussian filter; MLP: multilayer perceptron; PINN: physics-informed neural network.	100
5.7	The auxiliary network θ_2 generates an approximate elasticity mapping. Displayed are the reconstructed fields of Young's modulus in phantoms with (a) Type I and (b) Type VI lesions. The image from left to right shows the reference, the SELFNet results, and the PINN results. A 2 mm scale bar is included and the dash-dotted line is the boundary of the lesion.	101
5.8	Overview of (a) Relative ℓ_2 error, (b) RMSE, and (c) SSIM metrics for qualitative assessment. The box-plots display original data and data processed by a Gaussian filter, MLP, PINN, and SELFNet. The scatter points' color and size reflect the lesions' stiffness and diameter, respectively. SELFNet provides the second least relative ℓ_2 error and the most accurate reconstruction based on RMSE and SSIM metrics. Outliers are not shown for relative ℓ_2 error above 0.45, RMSE above 12 kPa and SSIM below 0.7.	103
5.9	The ground-truth axial displacement signals w at various lateral positions and $z = 23$ mm in (a) phantom and (b) <i>ex vivo</i> tissue. The width of wavefront in <i>ex vivo</i> tissue increases along the shear wave propagation direction.	105
5.10	<i>Ex vivo</i> reconstruction results using SELFNet. (a) The ground truth reconstruction of Young's modulus in a homogeneous sample. Due to the attenuation and dispersion of the shear wave, reconstruction in the bottom-right area is not reliable. The dash-dotted rectangle of 4×8 mm ² indicates the ROI used for RMSE and SSIM calculation. (b) Relative ℓ_2 error v.s. the number of acquired angles. (c) RMSE v.s. the number of acquired angles. (d) SSIM v.s. the number of acquired angles.	106
5.11	Reconstruction of Young's modulus in phantom of (a) a type VI lesion and (b) a type I lesion. (a) The mismatch of pattern inside the lesion decreases SSIM of reconstructed elasticity, with respect to ground-truth. (b) The artifacts occur when the shear wave leaves the lesion, resulting in increasing RMSE. The lesions are indicated by the dash-dotted circle. A scalebar of 2 mm is included.	111
6.1	Sequence for dual function ultrasound in sonothrombolysis. Ultrasound is switching among SWE ARF, therapeutic ARF and imaging modes.	118

List of Tables

3.1	Ultrasound imaging parameters in B-mode and Doppler mode.	52
4.1	Summary of experimental groups	71
5.1	SELFNet architecture. FFN: Fourier feature network; MLP: Multilayer perceptron.	91
5.2	Quantification summary of phantom data. The unit for RMSE is kPa. $N = 16$. MLP: Multilayer perceptron; PINN: physics-informed neural network; SELFNet: our proposed method; RMSE: root-mean-square error; SSIM: Structural Similarity index.	104

List of Nomenclature

ACRONYMS

μ CPC Micro Coulter particle counter.

2D Two-dimensional.

2D+T Two dimensional + time.

3D Three-dimensional.

ACUC Animal Care & Use Committee.

AD Automatic differentiation.

ANOVA Analysis of variance.

ARF Acoustic radiation force.

BC Boundary condition.

CDT Catheter-directed thrombolysis.

CNN Convolutional neural network.

CPWC Coherent plane wave compounded.

CUSE Comb-push ultrasound shear elastography.

DL Deep learning.

DVT Deep vein thrombosis.

FDM Finite difference method.

FEA Finite element analysis.

FEM Finite element method.

FFMD Flow-focusing microfluidic device.

FFN Fourier feature network.

GPU Graphics processing unit.

GT Ground-truth.

H&E Hematoxylin and eosin.

IQ In-phase and quadrature.

IVC Inferior vena cava.

LSD Least significant difference.

MB Microbubble.

MLP Multi-layer perceptron.

NTK Neural tangent kernel.

ODE Ordinary differential equation.

PCDT Pharmacomechanical catheter-directed thrombolysis.

PDE Partial differential equation.

PDMS Polydimethylsiloxane.

PE Pulmonary embolism.

PI Proportional-integral.

PINN Physics-informed neural network.

PRF Pulse repetition frequency.

PTFE Polytetrafluoroethylene.

PTS Post-thrombotic syndrome.

PW Plane wave.

RMSE Root mean square error.

ROI Region of interest.

rt-PA Recombinant tissue plasminogen activator.

RV Residual volume.

SELFNet Shear wave ELastography Fourier feature Network.

SNR Signal-to-noise ratio.

SSIM Structural similarity.

SWE Shear wave elastography.

UACDT Ultrasound-accelerated catheter-directed thrombolysis.

US Ultrasound.

VTE Venous thromboembolism.

Introduction

1.1 ULTRASOUND IMAGING AND MICROBUBBLES

Ultrasound (US) is one of the most widely used medical imaging modalities for diagnostic and therapeutic purposes^{1,2}. Ultrasound imaging is based on the propagation of mechanical waves, which are free of ionizing radiation, and interactions between ultrasound waves and tissues involve reflection, refraction, and diffraction^{3,4}. The cost-effectiveness and compact size of these instruments make ultrasound imaging to be applicable in various clinical settings. The typical ultrasound frequency of clinical relevance falls within the range of 1-15 MHz⁵.

Ultrasound waves have the ability to propagate through soft tissues and fluids, for example, muscles, vessels, and blood. The frequency-dependent back-scattering coefficient of red blood cells increases at high-frequency ultrasound⁶. Although recent attempts have been made to use red blood cells for contrast-free ultrasound localization microscopy using a synthetic aperture imaging sequence^{7,8}, red blood cells do not dif-

ferentiate from plasma due to a similar acoustic impedance and are considered weak scatterers in clinical imaging⁹. To improve ultrasound imaging contrast in blood flow imaging, contrast agents in blood flow are desirable, to assess smaller vasculature and tissue perfusion^{10,11}. The contrast agents most frequently used for clinical ultrasound imaging are microbubbles (MBs) of 1-6 μm diameter with a gas core and a stabilizing shell, such as phospholipids or albumin.

When exposed to an ultrasound pulse, the oscillations of MBs produce a pronounced reflected echo¹². As a result, the enhancement in signal intensity makes MBs a perfect contrast agent in contrast-enhanced ultrasound imaging¹³. More recently, localized microbubbles can overcome the diffraction limit and image microvasculature in super-resolution ultrasound imaging^{14,15}. If high acoustic pressure is applied, the MBs become unstable and cause a localized release of drugs or gene^{16,17,18,19}. MBs can be triggered by ultrasound to enable versatile applications of diagnostic imaging and/or therapy, tailored to particular needs.

1.2 MICROFLUIDICALLY PRODUCED MICROBUBBLES

Conventionally, microbubbles are fabricated via sonication or agitation of a gas-saturated solution containing the microbubble shell material. The inherent randomness in the mixing method results in high polydispersity in the MB size distribution. Therefore, MBs produced using this technique should undergo particle size sorting and counting, such as electro-impedance sensing, optical microscopy, or laser diffraction²⁰.

Microfluidics offers a different approach for generating controllable microbubbles by designing the shape of the inner channels within a microfluidic device. The microflu-

idic design morphologies for producing microbubbles include T-junction²¹, co-flow²², and flow-focusing techniques²³. For ultrasound imaging or therapy, microbubbles generated from a microfluidic device are monodisperse in terms of size distribution, compared to the commercially available counterparts^{24,25,23}. In the process of microbubble production, a microfluidic channel filled with gas (gas phase) interacts with a microfluidic channel containing liquid (continuous phase), leading to the formation of discrete microbubbles by gas-liquid interfacial instabilities through an orifice. The size of microfluidically generated microbubbles usually has a diameter of 5-10 μm for the use of ultrasound^{24,26}. Through the precise manipulation of the liquid phase and the gas phase within the micrometer-sized channels, it is possible to accurately generate populations of monodisperse bubbles. Another common way to adjust the size of microbubbles in microfluidics is to change the geometry of the microfluidic device.

Microfluidics presents significant benefits in the context of lab-on-chip fabrication, particularly in the generation of microbubbles at need. In this scenario, it has reduced energy consumption and minimal liquid volume requirement²⁷.

The microfluidically produced MBs, similar to traditional ones, can induce biological effects under ultrasound, due to transferred momentum, microstreaming, or collapse events²⁸. In microfluidics, the inner gas phase affects the stability and size of microbubbles. Therefore, one can fine-tune the stability of the generated microbubbles. For example, microbubbles of nitrogen core from a polydimethylsiloxane (PDMS) microfluidic device can dissolve in minutes^{29,30}. As transiently stable microbubbles dissolve rapidly downstream of the target therapeutic site, they can effectively minimize the risk of off-target effects^{31,32}. In this context, the transient stability makes these microbubbles a

potential therapeutic agent for blood clots in venous thromboembolism (VTE).

1.3 DEEP VEIN THROMBOSIS AND SONOTHROMBOLYSIS

Deep vein thrombosis (DVT) occurs when a thrombus forms in deep veins, primarily in the calf of the leg³³. This prevalent VTE condition, along with dislodged thrombi or emboli traveling to the lung, pulmonary embolism (PE), affects more than one million people annually in the United States³⁴. The reasons behind the formation of DVT are not universally agreed upon; however, blood clots may develop as a result of reduced or obstructed blood flow in the veins. The probability of DVT increases when there are risk factors, such as long-term sedentary, a family history of blood clots, obesity, or pregnancy³³. Conventional treatment of VTE, including oral anticoagulants such as warfarin, apixaban and rivaroxaban, reduces the risk of PE but does not dissolve the clot^{35,36}. Therefore, the venous system in patients often has permanent damage due to inflammation that can cause scarring and thickening of the venous wall. Approximately half of patients who use anticoagulants for treatment experience post-thrombotic syndrome (PTS), manifesting symptoms ranging from pain and swelling to edema, skin alterations, and, in extreme cases, venous ulcers³⁷.

Thrombolysis is the resolution of blood clots through systematic or intravenous injection of thrombolytic agents, or through catheter-directed delivery to the site of the thrombus³⁸. However, current thrombolysis techniques are still associated with an increased risk of bleeding and cannot effectively avoid PTS compared to standard anticoagulant treatments^{38,39,40}. There is a need for a safe and efficient therapeutic technique for DVT.

Sonothrombolysis has been investigated as a therapy to accelerate thrombus resolution using the combination of ultrasound, microbubbles, and thrombolytic agents⁴¹. Ultrasound can provide mechanical or thermal effects to improve thrombolysis, where acoustic radiation force (ARF) facilitates the penetration of thrombolytic agent into the thrombus, as well as the cavitation of MBs⁴². The sonothrombolysis technique has been validated in applications of *in vitro* models³¹, stroke^{43,32}, DVT⁴⁴, and myocardial infarction^{45,46}. However, the optimal parameters of US and MB have not yet been determined prior to *in vivo* therapy, and measurement schemes for sonothrombolysis must be investigated.

1.4 THROMBUS IMAGING

Evaluation of thrombus changes in thrombolysis is essential. In the *in vitro* setting, it is possible to weigh the mass of a thrombus pre- and post-therapy. Alternatively, studies are conducted sampling the concentration of blood clots in the flow system and measuring the level of optical absorbance in fluid or D-dimer (by-product protein fragment in the formation and dissolution of blood clots)^{31,47}. However, a standard approach is still lacking for the *in vivo* model of DVT, particularly in the rodent models. For example, *in vivo* models, requires euthanasia of the animals to determine the weight of blood clots. Therefore, imaging techniques that do not require termination are recommended to monitor changes over time. Currently, ultrasound imaging is widely used as a non-invasive method to identify potential DVT^{48,49}.

For sub-acute or chronic DVT, where long-term observation is required, the accuracy of traditional two-dimensional (2D) ultrasound imaging depends on the location

and angle of the transducer. Recent studies suggest the use of volumetric ultrasound, or three-dimensional (3D) ultrasound, in clinical patients of DVT^{50,51}. Reconstructing the thrombus in three dimensions (3D) can minimize errors caused by misalignment of the transducer at various times. To migrate from human to rodent scale, a transducer of higher frequency should be used for higher resolution. To gather additional information about blood clots, elastography-based imaging can be used to improve contrast or estimate phases of blood clots by evaluating tissue stiffness⁵².

1.5 DEEP LEARNING-ENHANCED SHEAR WAVE ELASTOGRAPHY

Shear wave elastography (SWE) provides an estimation of stiffness from the propagation of shear wave in biological tissues, deformed by external or internal stimuli⁵³. Recent advances in ultra-fast plane wave (PW) US imaging has enabled the tracking of shear wave generated from ARFs⁵⁴. SWE has shown advantages in measuring the thrombus^{55,52,56}. The difference in shear wave velocity can enhance the contrast between blood clots and background tissue/blood. However, the number of acquisitions or angles is critical for signal-to-noise ratio (SNR) in the final images. The reduced number of acquisitions results in low SNR. For *in vivo* setting of DVT quantification, SWE is also affected by motion^{57,58}.

Deep learning (DL) has begun to influence scientific computing in physics problems. A neural network in theory can approximate any function according to the universal approximation theorem⁵⁹. The framework of DL facilitates the use of automatic differentiation (AD) for differentiation computation. Consequently, physics-informed neural networks (PINNs) are effectively utilized to address partial differential equations

(PDEs) through optimizing the residual of the physics equations^{60,61}. The governing physics equations were modified and used a term in the loss function to enforce the laws of physics. PINN demonstrates its versatility across multiple fields, from addressing the Navier-Stokes equation^{60,62,63,64,65} to tackling issues in solid mechanics^{66,67,68,69}, and extending to healthcare modeling^{70,71}. Propagation of shear wave also follows the equations of motion similar to these problems, in a highly incompressible medium of biological tissue⁷².

Studies have explored the application of PINN in two dimensional + time (2D+T) shear wave elastography⁷³. These studies indicate that PINN is capable of learning the particle velocity/displacement field and can reconstruct the Young's modulus. However, the effectiveness of PINN has not been confirmed in low-quality data sets, where the number of acquisitions is limited. Consequently, my goal is to utilize PINN for noise reduction in shear wave data and improve its ability to assess thrombus dimensions and stiffness in *in vivo* imaging.

1.6 DISSERTATION SUMMARY

This dissertation explores the application of microfluidically produced MBs to accelerate thrombus dissolution, with a focus on deep vein thrombosis. It examines the use of sonothrombolysis with transiently stable MBs and addresses practical experimental challenges for future clinical translation. This sonothrombolysis therapy is characterized by monitoring and controlling MB production and assessing its effectiveness in an *in vivo* mouse model of DVT. Furthermore, it investigates a novel approach to potentially improve SWE, which could help in thrombus segmentation.

Chapter 2 discusses a closed-loop feedback control system in a flow-focusing microfluidic device with integrated on-chip electrodes. The diameter and count of MBs are measured by the impedance change between the electrodes. A proportional-integral (PI) controller adjusts the input conditions to the microfluidic device and maintains the MB diameter at the setpoint.

Chapter 3 implements high-frequency 3D ultrasound to scan blood clots in a partially ligation mouse model of DVT. The variance in blood clot volume is inherently large and challenging to control in this animal model. Segmentation from 3D B-mode acquisition provides an accurate estimate of thrombus volume and is compared to weight or macroscopic observation.

Chapter 4 reveals the efficacy of microfluidically produced MBs in a sonothrombolysis experiment. The lifetime of MB within the venous circulation is characterized in a mouse. A complete investigation involving microbubbles and the other control groups is performed using the mouse model of pre-existing DVT. The findings are evaluated using the method described in Chapter 3 and confirmed by histological analysis.

Chapter 5 illustrates the use of Fourier feature network (FFN) in shear wave elastography. The proposed method incorporates a sparse representation of input coordinates and approximates the displacement field for the shear wave propagation problem. Data acquired from *in vitro* phantoms of lesions and *ex vivo* tissue are validated. The performance is compared with traditional filtering techniques in terms of displacement and reconstruction accuracy.

Chapter 6 outlines the key contributions of this dissertation and provides directions for future research.

Real-time size control of microfluidically produced microbubbles using a micro Coulter counter

2.1 INTRODUCTION

Microbubbles (MBs) have been developed and widely studied in medical ultrasound applications. For example, MBs can be used for contrast enhancement,^{74,75} therapy,^{76,77} localised drug and gene delivery,^{78,79,80} and sonothrombolysis to promote recanalization in ischemic stroke.^{31,32,81,82,83} The most widely employed method to produce MBs involves agitation or sonication of gas-saturated surfactant dispersions and results in polydisperse MB populations that must often be size-sorted prior to *in vivo* intravenous administration^{84,74,85,86,87,88,89,90}. However, microfluidic designs such as T-junction²¹, co-flow²², and flow-focusing are capable of producing monodisperse populations of microbubbles without the need for size sorting, although at significantly reduced produc-

tion rates relative to agitation and sonication^{24,25,23,91}. MBs produced by microfluidic devices also have the advantages of real-time tunability in terms of size, production rate, and temporal stability^{24,25,91,30}. Flow-focusing microfluidic devices (FFMDs), in particular, focus a gas thread between two liquid flows, and monodisperse MBs are released from an outlet port, at a production rate that is typically between 10^4 and 10^6 MBs/s^{24,31}.

As a practical matter, the limited production rate and the low stability of microfluidic generated MBs have precluded the approach's adoption for most applications. However, in the context of sonothrombolysis, the combination of large MBs, low production rate and low stability are advantageous. This combination provides an optimal design in terms of potential efficacy and safety^{31,32}. However, real-time production of MBs would, logically, require close monitoring of number and diameter of MBs in order to provide adequate quality control and assurance of clinical efficacy and safety. A measure of MB count, diameter and conclusive verification of no fault condition(s) being present (e.g. a "blow through") must be considered.

Additionally, other microfluidic applications may also benefit from real-time control and measurement during production of on-chip particles. Bubble size determines ultrasound resonance frequency as well as selection of imaging frequency. In drug delivery and therapeutic applications, larger MBs are associated with greater bioeffects⁹². For reactions and mixing in microfluidic devices, droplet size is significant to the reaction rate⁹³. In this context, real-time monitoring and control of production parameters is crucial to further adoption of microfluidic devices in various applications.

At high production rates in FFMDs, a feasible way to measure the non-conductive particle size in microfluidics systems is by a resistive method using the Coulter Princi-

ple^{94,95,96,97}. Coulter counters are widely used in sizing and counting cells and colloidal particles^{94,98}. The sensor detects the resistance perturbation that is proportional to a particle's volume while the particle passes through the sensing zone. Miniaturization and integration of the Coulter counter within the microfluidic device results in what is referred to as a micro Coulter particle counter (μ CPC)⁹⁵, enabling real-time particle measurement in a lab-on-a-chip environment^{99,100}. Previous studies have proposed a new FFMD design with integrated μ CPC that succeeded in off-line characterization of MB diameter and production rate⁹⁷. This measurement utilized a compensation method that required a priori knowledge of the device's operating parameters, but the approach can be modified to enable real-time MB diameter control in FFMDs.

A possible control scheme for MB diameter involves real-time measurement of the MB diameter *in situ* and use of a feedback controller to adjust flow and/or pressure conditions and thereby produce MB of a desired diameter^{101,102,103}. In this method, the input parameters are adjusted by comparing the diameter and production rate of the produced MB to the desired diameter. Miller *et al.* demonstrated that the implementation of a proportional-integral (PI) control system enabled droplet production of required size, measured by a high-speed camera, with limited knowledge of the fluid material properties¹⁰¹. Similarly, Fu *et al.* verified electrical detection to be effective for droplet size measurements in a T-junction¹⁰³. However, the production rates in these systems were less than 50 particles per second^{101,103}, which is several orders of magnitude less than the MB production rate of FFMDs.

In this chapter, I propose a real-time measurement method and a closed loop feedback system to control the diameter of MBs produced at the expanding nozzle of an FFMD

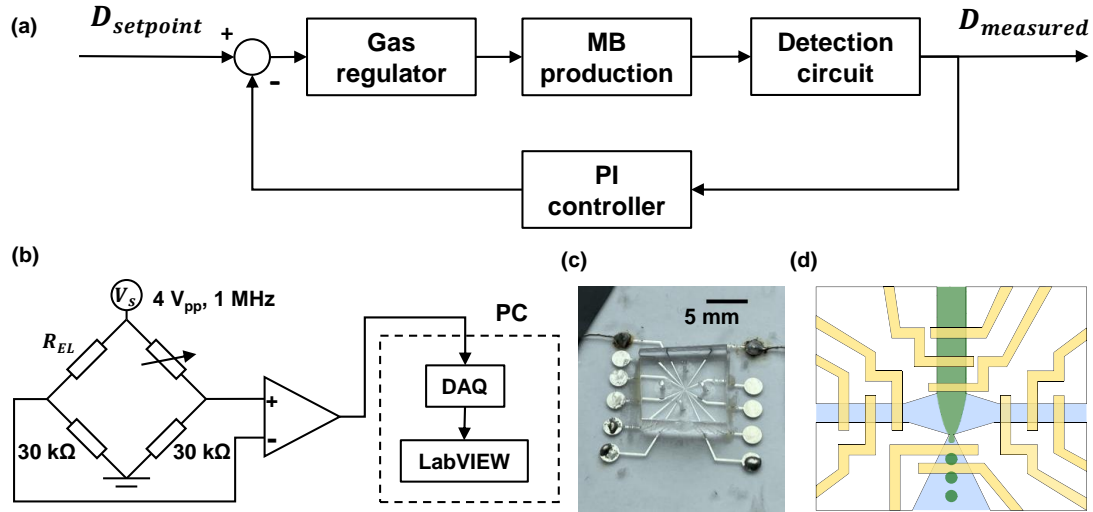


Figure 2.1: Schematic of the closed-loop control FFMD system. (a) Working principle of the control system. A PI controller regulates input gas pressure based on the measured diameter. (b) The output of the Wheatstone bridge is amplified and connected to a data acquisition system. (c) Image of a benchtop FFMD with μ CPC. (d) Produced MBs traverse the detection region of electrodes. The other electrodes monitor the flooded situation inside the polydimethylsiloxane (PDMS) channel.

with an integrated μ CPC. In addition to enabling real-time control over the operating parameters of the FFMD, the control system monitors the production of MBs and detects abnormal operational states of the FFMD. Ultimately, this monitoring system provides real-time feedback regarding the operation of the FFMD, which is required to meet the anticipated safety and efficacy requirements of future clinical translation.

2.2 METHODS

2.2.1 DEVICE FABRICATION AND MICROBUBBLE PRODUCTION

The FFMD was comprised of a microfluidic channel and a 500- μ m thick glass wafer with 11 electrodes. The microfluidic channel was fabricated by a custom SU-8 (3025,

MicroChem, Newton, MA) developed mold. The channel pattern was developed to be 20 μm in height, and cast with PDMS (Sylgard 184, Dow Chemical, Midland, MI, USA), as previously described³⁰. A glass wafer served as a substrate and standard lift-off techniques were used to fabricate the electrodes^{95,97}. Photoresists LOR10B and AZ4110 (MicroChem, Newton, MA, USA) were applied on the glass wafer, which was later patterned with a transparent photomask. An electron beam evaporation system was used to sputter 20 nm Titanium (Ti)/100 nm platinum (Pt) on the substrate. After deposition, the extraneous metal was removed by standard lift-off technique. The PDMS microfluidic device channels were aligned with the electrodes patterned on the glass wafer by a custom 3D positioning stage (Thorlabs Inc., Newton, NJ, USA) and the PDMS channel and the borosilicate glass wafer substrate were plasma bonded and immediately heated at 70°C for 1 h.

MBs were produced using a liquid phase of bovine serum albumin (4% weight/volume BSA) and dextrose (10% weight/volume) dissolved in isotonic saline (0.9% NaCl) and a dispersed phase of 99.995% purified nitrogen (Praxair Inc., Danbury, CT, USA). The liquid phase was administered by a syringe pump (PhD 2000, Harvard Apparatus, Holliston, MA, USA) and the dispersed phase was supplied by an electronic regulator (PC-series, Alicat Scientific, Tucson, AZ, USA). Both phases were introduced to the FFMD channels by microbore polytetrafluoroethylene (PTFE) tubing of 762 μm outer diameter. The FFMD was operated within the field of view of an IX51 microscope (Olympus, Center Valley, PA, USA) and continuously observed in real time.

2.2.2 FINITE ELEMENT ANALYSIS

Finite element analysis (FEA) was performed using COMSOL 4.4 (Burlington, MA, USA) to estimate the impedance between electrodes in the expanding nozzle when excited by a $4 V_{pp}$, 1 MHz signal. The FEA setup was based on the measured geometry from the FFMD image under the microscope. Fig. 2.1(d) depicts the electrode setting of the device. The proximal electrode was $9 \mu\text{m}$ wide and $18 \mu\text{m}$ away from the expanding nozzle. The distal electrode was $10 \mu\text{m}$ wide and $34 \mu\text{m}$ away from the expanding nozzle. The distance between electrodes was $15 \mu\text{m}$. The detection region was $20 \mu\text{m}$ tall with an expanding nozzle that expanded 65° with respect to the nozzle. The electrode design was optimized for MBs between 8 and $25 \mu\text{m}$, so the electrode output was sensitive to MB diameter when using an excitation signal of 1 MHz excitation frequency^{95,104}. The design was fabricated and verified in a previous study⁹⁷.

The impedance between electrodes was simulated using the follow procedures: (1) The newly produced MBs passed through the detection region, while the adjacent MB stayed still; (2) The simulation was designed to model MB aggregation as they flowed through the expanding nozzle. MBs were modeled to exit the expanding nozzle at a constant rate. The center of the MB was at $10 \mu\text{m}$ height, the same as the center of the channel. Diameter of MBs was varied from 14 to $26 \mu\text{m}$, and the location of the center of the adjacent MB was set above both edges and the center of the distal electrode. For MBs of 14 – $20 \mu\text{m}$ diameter, a newly produced MB traverses the detection region and collides with another MB at three different locations (Fig. 2.3(a)). For MBs of $> 20 \mu\text{m}$ diameter, only one MB passage was simulated because MBs of such diameter are larger than detection region and channel height. The maximum impedance change is associ-

ated with the total conductivity in the detection region, so the diameter of the MB dominates this value. The location of the adjacent MB also affects the total non-conductive volume. However, its contribution to the impedance should be less significant than the newly produced MB because it is farther from the proximal electrode⁹⁷.

2.2.3 SIGNAL ACQUISITION AND SIGNAL PROCESSING

The impedance difference between electrodes in the expanding nozzle was detected by a Wheatstone bridge excited by a $4 V_{pp}$, 1 MHz sinusoidal waveform. One branch of the Wheatstone bridge included electrodes within the expanding nozzle and a $30 \text{ k}\Omega$ resistor. The other branch consisted of a potentiometer and a $30 \text{ k}\Omega$ resistor to balance the impedance ratio. The bridge was pre-balanced at each initialization when only the liquid phase passed through the detection region. The output of the bridge was amplified by a LM6171 (Texas Instruments, Dallas, Texas) differential amplifier with a 4-fold gain.

The output of the circuit and the reference excitation signal were sampled using LabVIEW (National Instruments, Austin, TX, USA) by a data acquisition system (ATS460, Alazar Technologies Inc., Pointe-Claire, QC, Canada). The data were acquired at 10M samples/s for a 32768-sample-point record, and coherently demodulated using quadrature demodulation in LabVIEW to extract the impedance signal^{105,95,106}. This signal was filtered using a 10th order Butterworth low-pass filter with 300 kHz cutoff. Subsequently, the maximum voltage in each microbubble transit period was selected by a peak detection algorithm written in MATLAB (Mathworks, Natick, MA, USA) and averaged over the record. The voltage after processing was denoted as time-average maximum voltage, \bar{V}_{max} . The MB production rate was calculated using the time difference between

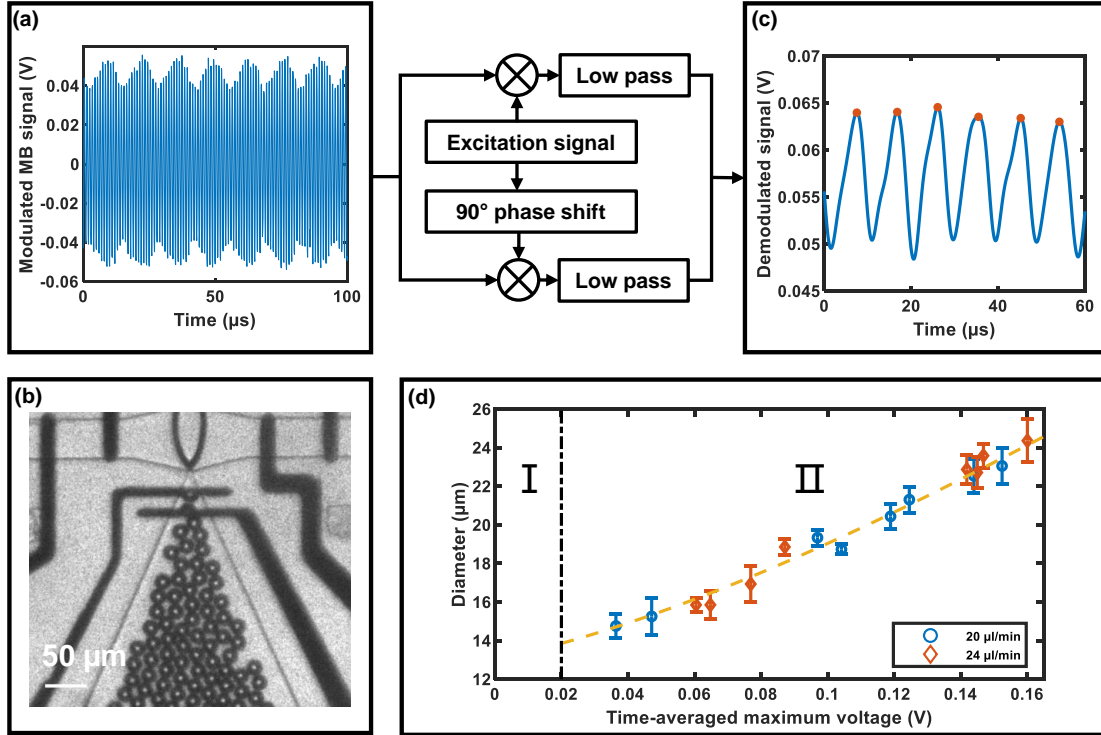


Figure 2.2: (a) Modulated MB signal and (b) a high-speed optical image of MBs were captured simultaneously. (c) Demodulated MB signal were acquired by absolute value of quadrature demodulation. The peaks of the demodulated signal were selected and averaged over the sampling. (d) Optically determined diameter vs. time-averaged maximum voltage.

maxima in each record.

$$\text{production rate} = \frac{\# \text{ of maxima} - 1}{t_{last} - t_{first}} \quad (2.1)$$

where t_{last} is the time of the last maximum signal and t_{first} is the time of the first maximum signal. After collection of both electrical signal and images for 5 flow rates (Q_c), a cubic polynomial function of diameter *versus* time-averaged maximum voltage was computed in MATLAB to permit future monitoring and control of MB diameter. At the same time, I contend that the MB count is accurate. So long as the signal associated

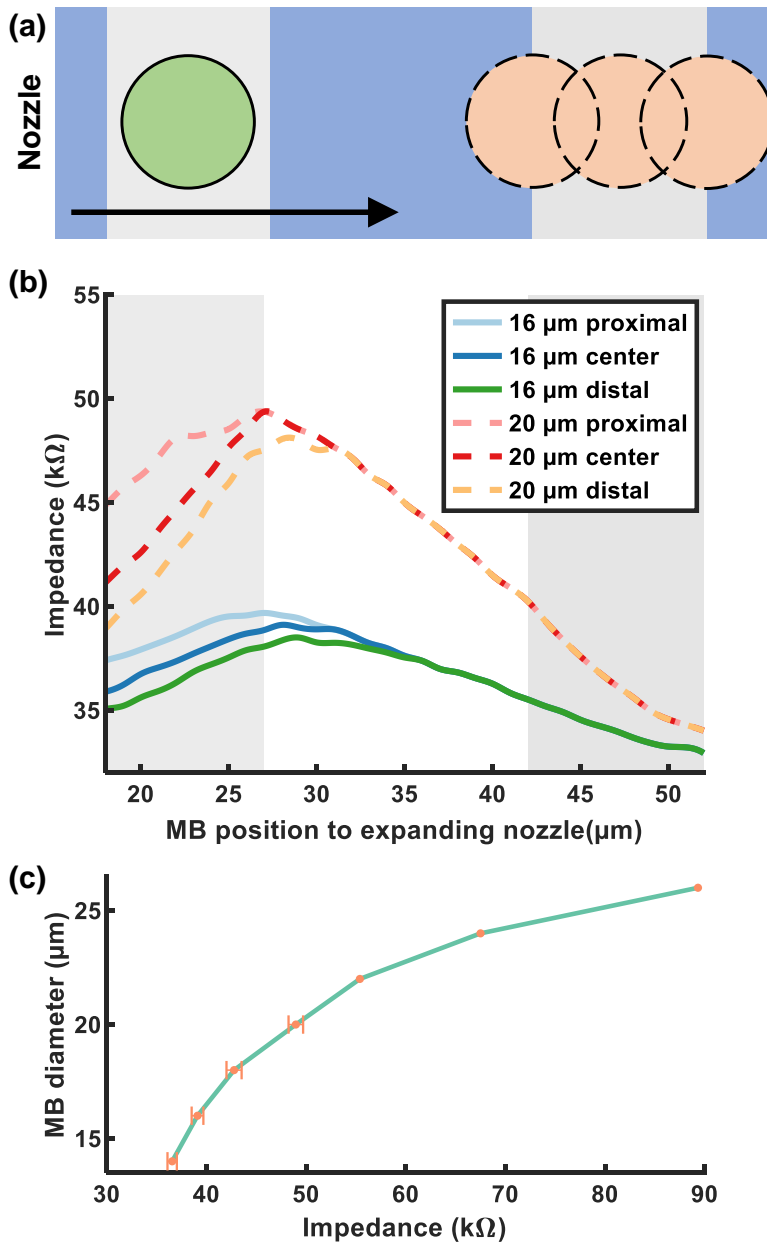


Figure 2.3: FEA results of MBs travel through detection electrodes. (a) The traverse of a MB through detection region and moved close to the adjacent MB at three different locations. (b) The impedance of 16 and 20 μm MB passage as described previously. (c) The impedance maxima of 14 to 26 μm MBs were plotted.

with the MB transit is detectable, there is no plausible error and no ideal reference standard is available. For example, when using optical observation of MB production, the limited frame count in high speed photography (24 frames in our case) is a more serious limitation to accurate counting than exists with continuous Coulter-based measurement of the same production instance⁹⁷. The comparison between our electrical method and optical method is included in Fig. 2.4.

2.2.4 CLOSED-LOOP FEEDBACK CONTROL

Feedback from the real-time diameter measurements of MBs was used to adjust the input pressure of the dispersed phase (Fig. 2.1(a)). A PI controller program written in LabVIEW was used to calculate the adjusted amount of pressure based on the difference between measured diameter and the setpoint diameter. The following equation can be used to parameterize the control schematic:

$$u(t) = K_c \left(e(t) + \frac{1}{T_i} \int_0^t e(\tau) d\tau \right) \quad (2.2)$$

where $e(t)$ is the difference between a setpoint diameter $D_{setpoint}$ and a measured diameter $D_{measured}$, K_c is the proportional gain, T_i is the integral time constant, and $u(t)$ is the adjustment value. To adjust the parameters of the PI controller, the commonly used Ziegler-Nichols method was applied to determine the PI controller's proportional gain K_c and integral time T_i ¹⁰⁷. A range of K_c values were applied on the proportional-only feedback control system to determine the ultimate gain K_u at which the output started to have a stable oscillation with an oscillation period T_u . After the P-only evaluation, the PI controller parameters can be calculated by

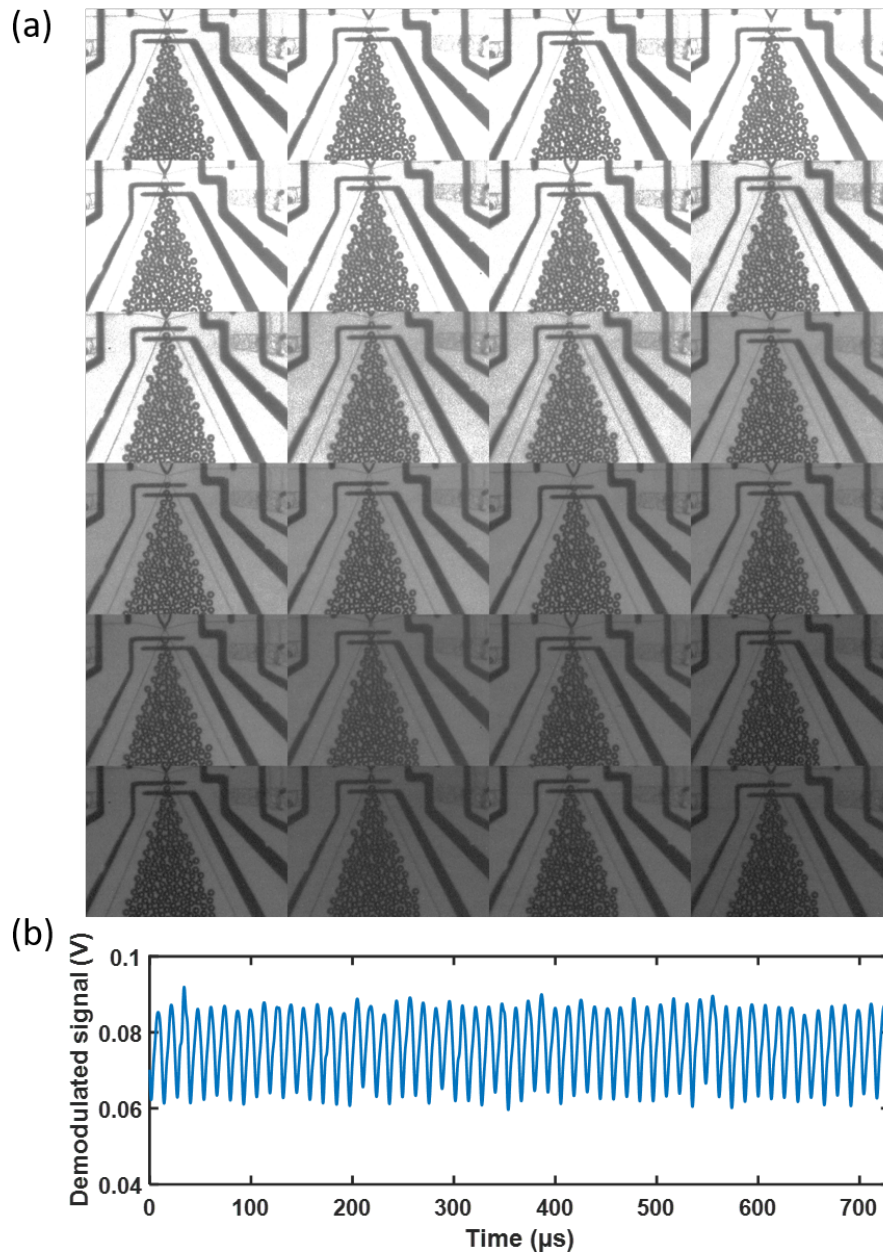


Figure 2.4: An example of optical and corresponding demodulated electrical data. In (a), it took a MB approximate 13 frames to pass through the detection region (frame 8-21). The imaging speed was at 1 million frames per second, the rough production rate was 77 ± 3 kMBs/s. In (b), there were 56 local peaks in 716 μ s. The production rate using electrical counting was 77 kMBs/s.

$$K_c = 0.45K_u \quad (2.3)$$

$$T_i = T_u/1.2 \quad (2.4)$$

In the feedback control system, the electrical signal responsive to instantaneous MB diameter was sampled and the input gas pressure was adjusted every 200 ms in real-time experiments. The step response of MB electrically determined diameter from 18 to 20 μm was recorded using different PI parameters. Another test was performed to ascertain the system response of the feedback control system with different step sizes. MBs stabilized at an electrically determined diameter of 18 μm were increased to between 19 and 24 μm an interval of 1 μm , repeating 3 times for each step size.

Finally, MB diameters were adjusted in a step-wise fashion across a large diameter range ($Q_c = 20 \mu\text{L}/\text{min}$). To assess the precision of our system in specifying MB diameter, diameter was stepped between 18 and 24 μm at a step size of 0.5 μm every 30 seconds. To determine the maximum possible range of specified MB diameters, diameter was stepped between 14 and 24 μm at a step size of 2 μm every 30 seconds.

2.3 RESULTS

2.3.1 MICROBUBBLE PRODUCTION BY FFMD

MBs generated by FFMD are shown in Fig. 2.2(c) and electrical signals collected by the detection circuit illustrated in Fig. 2.1(b). The height of the channel in the FFMD was between 20 and 22 μm and the width of the nozzle was approximately 6 μm . The

input gas pressures and flow rates were varied from 51 to 103 kPa and 16 to 28 $\mu\text{L}/\text{min}$, respectively. The MBs diameters ranged between 13.2 and 28 μm at production rates between 45×10^3 and 140×10^3 MBs/s. The MB production rate was limited by (i) the strength of adherence of PDMS to the glass wafer substrate, (ii) the need to produce monodisperse MBs, as significant jumps in pressure would lead to MBs with noticeably polydisperse populations.

2.3.2 FEA RESULTS

The schematic of a FEA simulation is illustrated in Fig. 2.3(a). The FEA results in Fig. 2.3(b) reveal that the maximum impedance measured for a given MB is affected mostly by the MB diameter, and less so by the locations of adjacent MB. The maximum impedance occurs when the center of a MB enters the inner region between the electrodes and matches our previous findings⁹⁷. The total conductivity is associated with the addition from volume of the adjacent MB, but the adjacent MB being far from the proximal electrode reduces its contribution to total conductivity.

The maximum impedance with varying locations of adjacent MB was simulated from a diameter of 14 to 20 μm . MB from 22 to 26 μm were simulated without an adjacent MB, since MBs of these dimensions were larger than the detection region. The simulation result was plotted in Fig. 2.3(c) to display the relation between MB diameter and maximum impedance induced by MB. As depicted in Fig. 2.3(c), the diameter-impedance relationship is non-linear. To compute the diameter in real-time, a cubic polynomial was used to represent the relation in practical measurements as the change in conductivity is a function of the volume of liquid displaced by the MB.

2.3.3 ELECTRICAL DETECTION OF MB DIAMETER

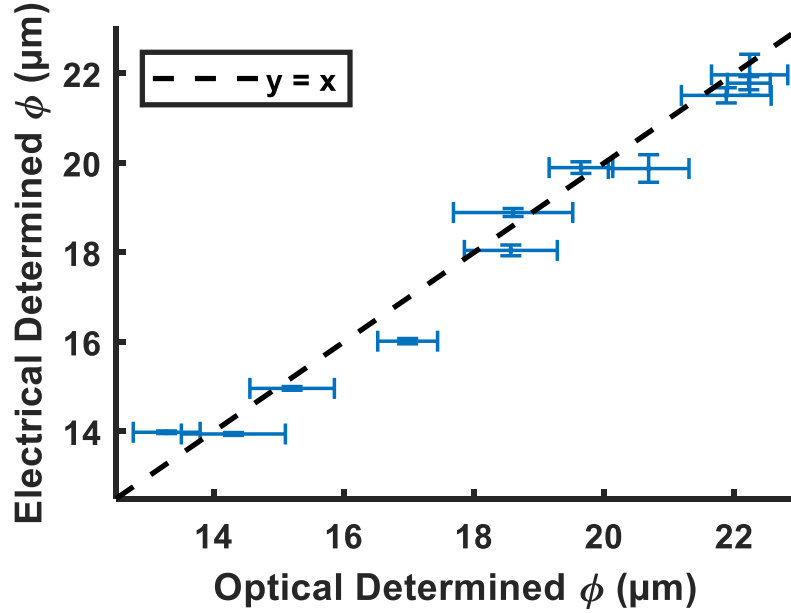


Figure 2.5: Validation data of electrically determined diameter vs. optically determined diameter. $R^2 = 0.98$.

The electrical signal was collected (Fig. 2.2(a)) and demodulated (Fig. 2.2(c)) as described above. The dashed line in Fig. 2.2(d) depicts the fitting function to be used in monitoring MB diameter. Region I is an unstable zone, where there are no MBs but the demodulated signal is larger than 0 V, while region II is the measurable range. A cubic polynomial fit was performed between optically determined diameters and corresponding \bar{V}_{max} . The fitting result is illustrated in Fig. 2.2(d) and is described by the following equation:

$$D_{electrical} = -457.75\bar{V}_{max}^3 + 271.55\bar{V}_{max}^2 + 37.86\bar{V}_{max} + 12.99 \quad (2.5)$$

where $D_{electrical}$ is MB diameter in μm . The equation applies when $0.020 \leq \bar{V}_{max} \leq 0.165\text{V}$.

Validation data were also collected to test the accuracy of the model. Eleven high speed images and corresponding electrical signals were collected with the same method as a validation set. The electrically determined diameters calculated by equation (2.5) were compared to the optical diameters in Fig. 2.5. The root mean squared error of the electrically determined diameters to the optical diameters were $0.53\ \mu\text{m}$, while the R^2 value was 0.98.

The model fit of MB diameter vs. time-averaged maximum voltage was used to attain an equation relating the electrically determined MB diameter and electrical measurement of impedance change. The system acquired measurements of MB diameter every 0.2 seconds, enabling real-time implementation of a feedback controller to adjust the setpoint diameter.

2.3.4 CHARACTERIZATION OF FFMD FEEDBACK CONTROL SYSTEM

A PI controller was implemented as in Fig. 2.1(a). When K_c was increased to 0.1, the system reached ultimate sensitivity¹⁰⁷, and oscillated as shown in Fig. 2.7, with a period of approximately 4 s. From equation (2.3) and (2.4), K_c and T_i were estimated to be: $K_c = 0.045$, $T_i = 3.3\ \text{s}$.

MBs were produced from 18 to 20 μm under 3 sets of parameters in Fig. 2.6. Initially, the electrically determined MB diameter was stabilized at 18 μm and the setpoint diameter was increased to 20 μm , therefore the input gas pressure was adjusted by $e(t)$. With increasing integral time in PI controller, the overshoot decreased as anticipated

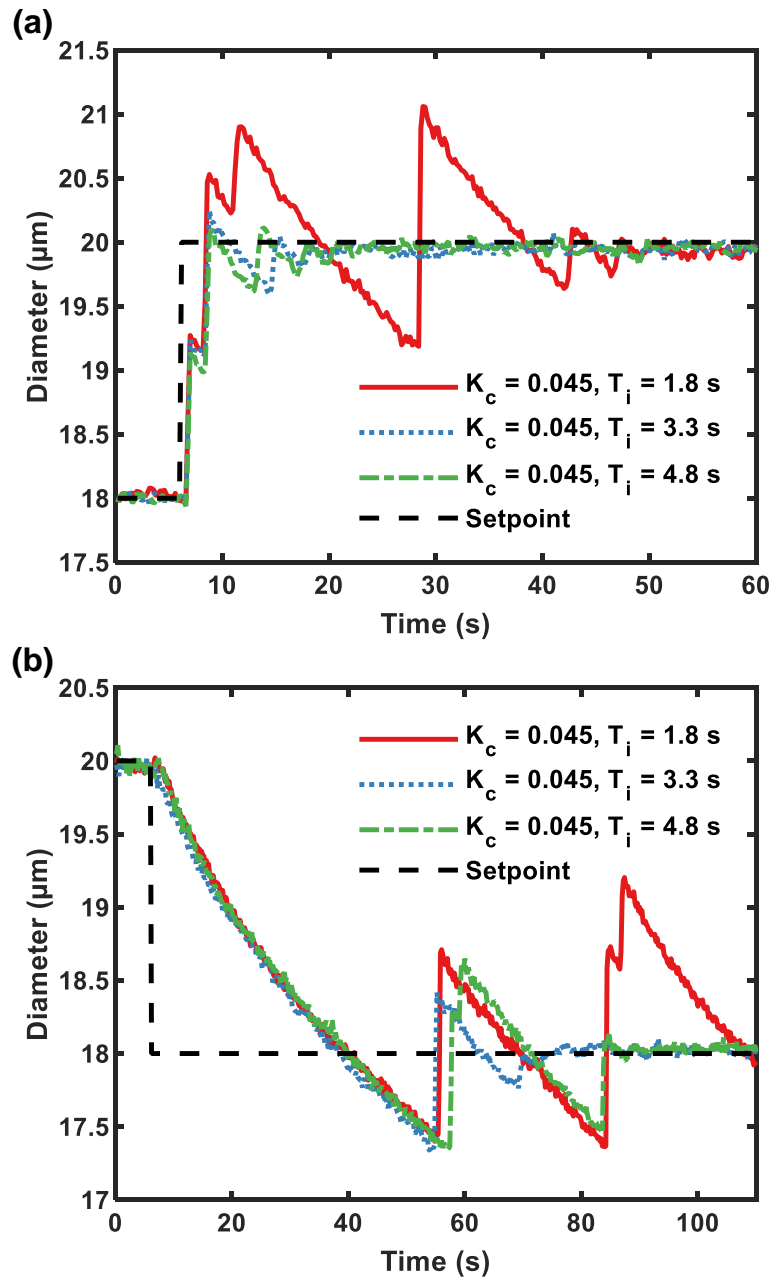


Figure 2.6: Step responses of closed-loop control FFMD system with three different sets of parameters. (a) Increase from 18 to 20 μm . (b) Decrease from 20 to 18 μm .

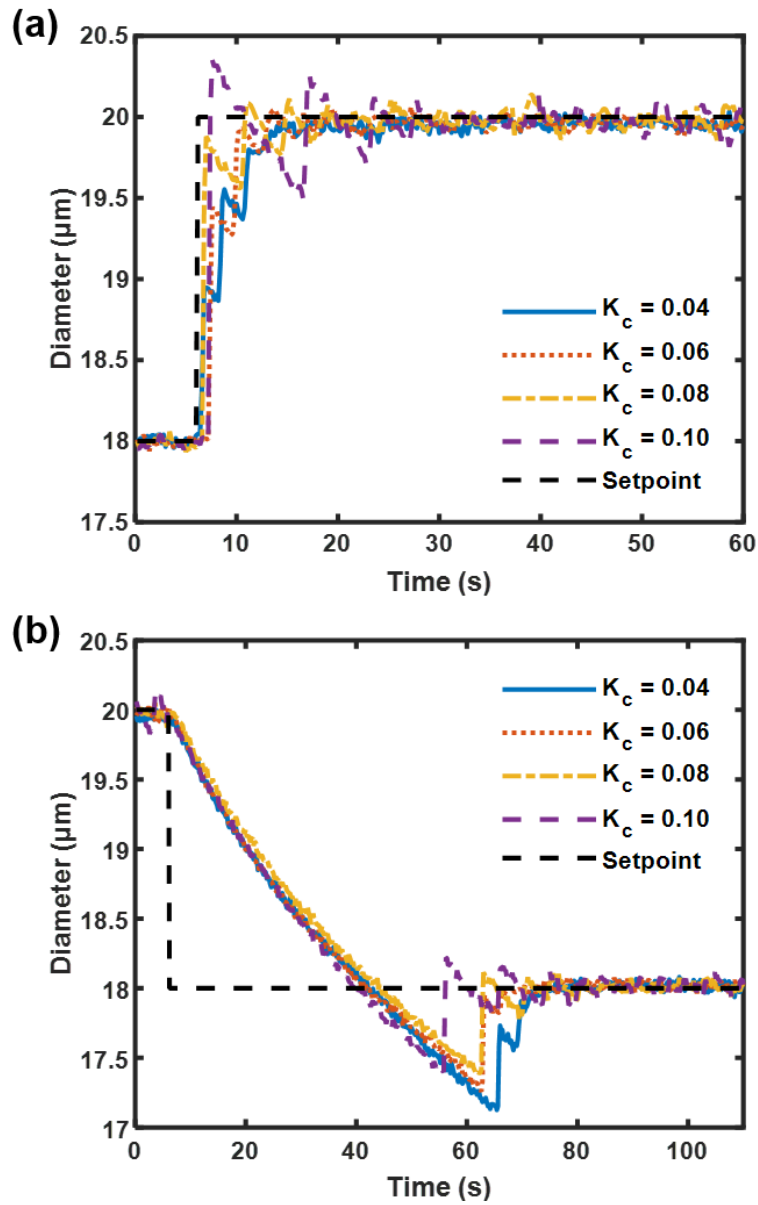


Figure 2.7: Step response (a) for setpoint of MB diameter changing from 18 to 20 μm and (b) from 20 to 18 μm with a Proportional controller. A variety of proportional gains (K_c) are implemented to determine the optimal proportional gain and integral time to be used in a Proportional-Integral controller.

and the system settling time was short (< 20 s) in Fig. 2.6(a). When the integral time constant was too small (1.8 s), the system exhibited a larger oscillation and longer settling time. The result was different when it came to reducing the MB diameter. The time required to reduce MB diameter was shortened by releasing gas pressure of the regulator. The regulation of increasing and decreasing pressure is achieved by different motions of mechanical parts within the regulator, so the control of diameter in Fig. 2.6 (a) and (b) behaves differently¹⁰⁸. It takes longer to reduce the inner pressure of the gas channel than it does to inflate the channel by the same pressure. As expected, the rate of pressure loss in Fig. 2.6(b) using different parameters was basically the same.

Fig. 2.8(a) demonstrates the response of the system at varying setpoints. The difference between the original and destination setpoint diameter determined the requisite gas pressure change and the settling time. The destination setpoint diameter was associated with the pressure that was needed to maintain the MB diameter. As observed, when the MB diameter was changed from 18 to 24 μm , the electrically determined diameter took longer to settle and demonstrated more obvious fluctuations than cases in which the destination diameter was closer to the setpoint diameter.

The relative input gas pressure to the initial pressure at $t = 0$ s was recorded in Fig. 2.8(b). The change in pressure was related to the destination setpoint. A linear fit was performed for pressure *versus* time when the electrically determined diameter became stabilized (> 15 s). The rate of pressure change was linear with respect to the setpoint diameter ($R^2 = 0.99$). This suggests that to maintain a stable diameter in an FFMD, the input pressure should change with a constant rate for a fixed flow rate.

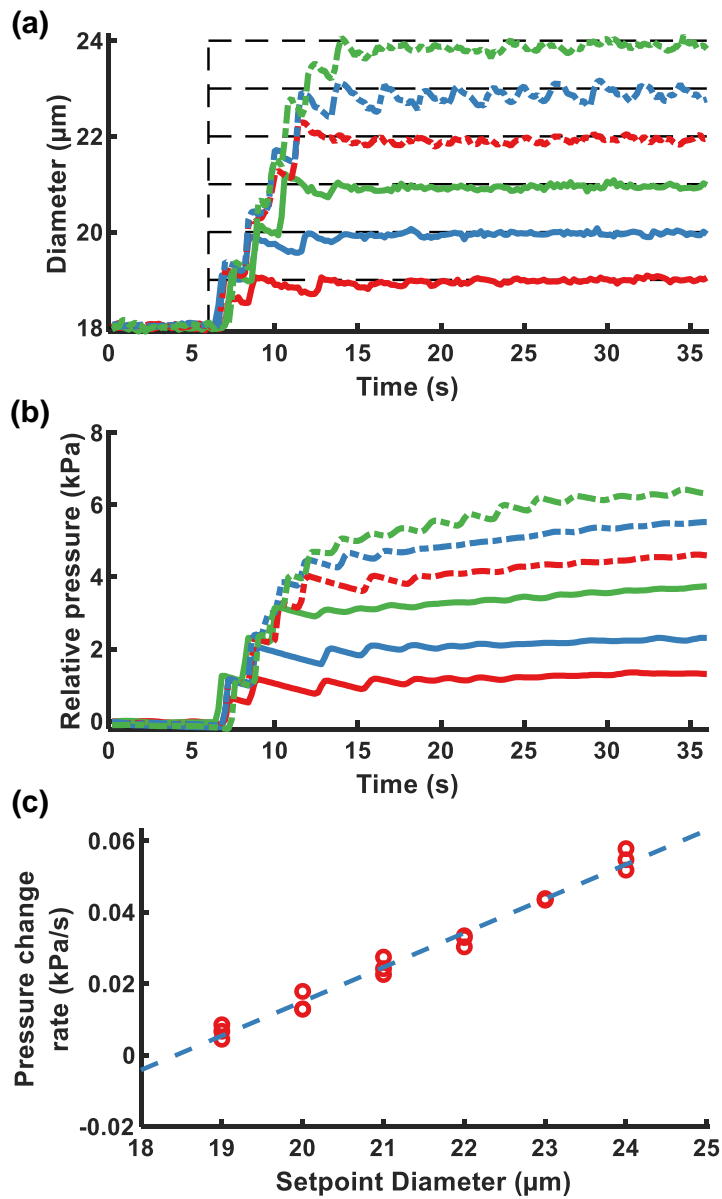


Figure 2.8: Step responses of feedback control FFMD with various destination setpoints at flow rate of $22 \mu\text{L}/\text{min}$ with $K_c = 0.045$ and $T_i = 3.3 \text{ s}$. (a) Measured diameter of different setpoint diameter from $18 \mu\text{m}$. The dashed line is the setpoint diameter. (b) Relative measured input gas pressure over time. The lines correspond to the process with same line type and color in (a). (c) Change rate of relative pressure 15 to 36 s vs. setpoint diameter.

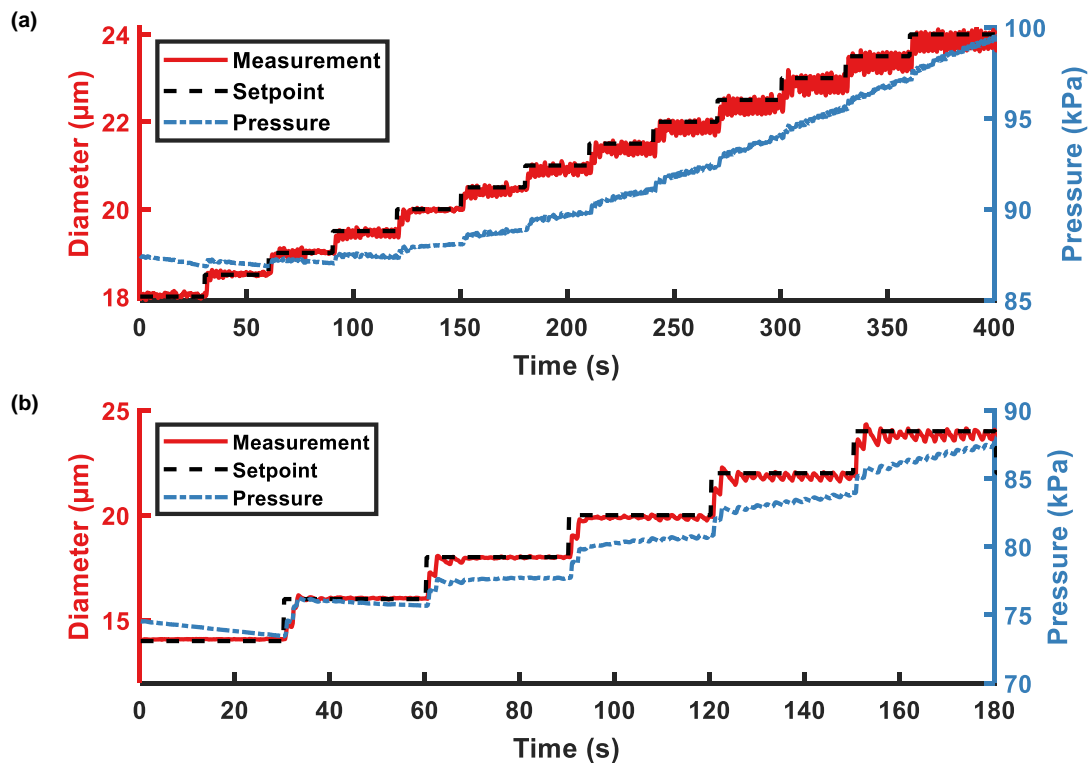


Figure 2.9: Feedback control with multiple steps of electrically determined diameter. (a) MB electrically determined diameters were increased from 18 to 24 μm by increments of 0.5 μm every 30 s. (b) MB electrically determined diameters were increased from 14 to 24 μm by increments of 2 μm every 30 s.

2.3.5 MULTIPLE STEP CHANGES OF DIAMETER

The multiple setpoint experiments used a PI controller with $K_c = 0.045$ and $T_i = 3.3$ s. Electrically determined diameters of MBs and corresponding input gas pressure were recorded, in Fig. 2.9(a), with an increment of 0.5 μm and also in Fig. 2.9(b), with an increment of 2 μm.

With different step size, when the MB diameters were large (> 20 μm), the variation of the electrically determined diameters was significantly higher than those of smaller

MBs. The oscillation in larger MBs was caused by the oscillation in input pressure. As discussed before, the pressure rate of change for larger MB was greater than for smaller MBs.

2.4 DISCUSSION

The FFMD was designed to optimize the detection of impedance changes induced by the passage of large MBs (10 – 25 μm) through the Coulter sensing zone. The electrode spacing and excitation frequency was optimized *in silico* for peak sensitivity when sensing MBs of diameter between 8 – 25 μm , permitting real-time control of MB diameter using a closed-loop feedback control system. Remote monitoring and control of MB diameter within these ranges was successfully demonstrated across MB setpoint values between 14 – 24 μm with effective settling times of less than 10 s.

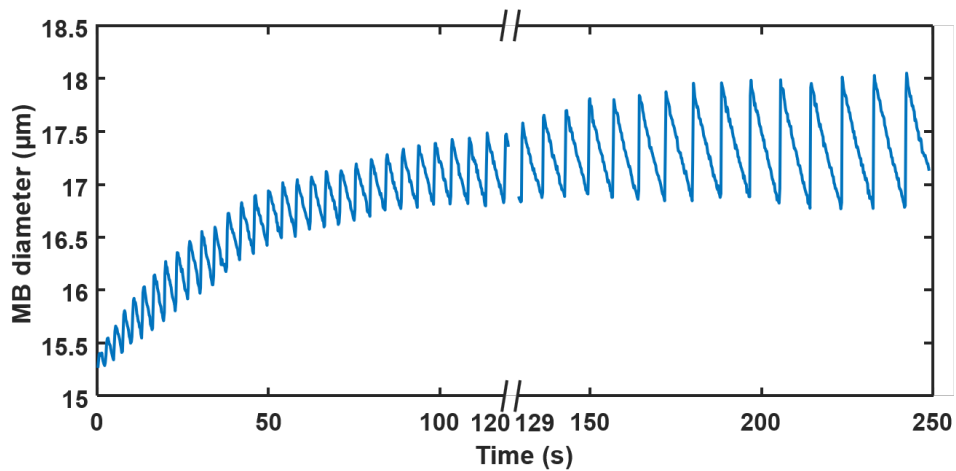


Figure 2.10: System response of a constant input gas pressure. The initial electrically determined diameter was 15.3 μm and the setpoint gas pressure was 77 kPa.

Use of a control system to maintain a constant MB diameter is essential. As suggested

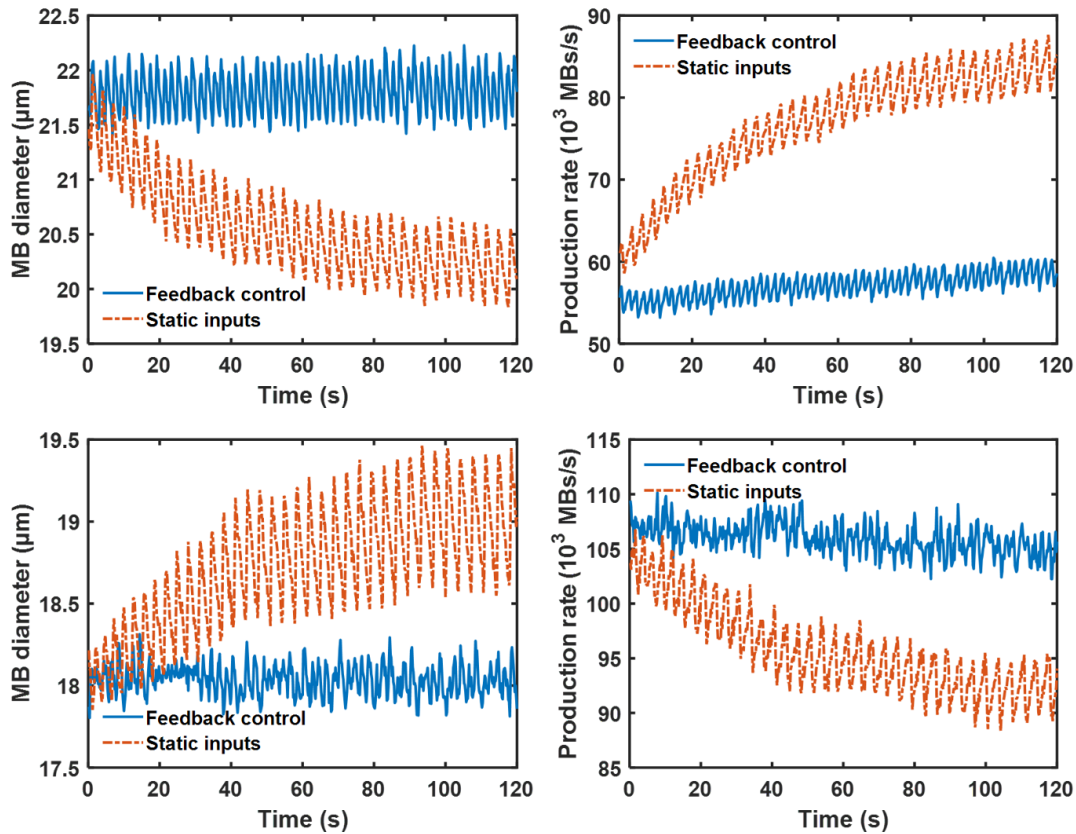


Figure 2.11: Comparisons between PI controlled and static input MB production. MB diameter was stabilized at 22 µm for 120 s, after which the system used the constant input flow rate and gas pressure of 103 kPa, in the top row. The same process repeated in the bottom row, but the initial diameter was 18 µm and the constant input gas pressure was 95.4 kPa.

in Fig. 2.10 and 2.11, when the input pressure of the gas regulator remained constant after disabling the controller, the production of MBs drifted to steady-state and the oscillation of MB diameter tended to increase. These undesirable effects were mitigated by the introduction of the controller, which actively adjusted the input gas pressure to maintain a constant MB diameter.

Unexpectedly, the gas pressure and liquid flow rate required to maintain a specific MB diameter are not static parameters, but rather must be modified dynamically to maintain

stable MB production. In the FFMD design studied, maintaining MB production at large diameters ($> 18 \mu\text{m}$) required a continuously increasing gas pressure. This may be due to material compliance along the length of the gas tubing and gas channel within the FFMD, in addition to a pressure drop when the electronic regulator delivers gas into the microfluidic device's gas orifice. As a result, while MB diameter remained fixed, the MB production rate varied with increasing gas pressure, suggesting that both MB diameter and MB production rate cannot be controlled by only modulating the gas pressure. A potential consequence of continuously rising pressure is that it may lead to either the failure of the FFMD or the inability to exert input gas pressure beyond regulator's range. When designing these systems, the material properties are critical factors to consider. The bond-strength of the PDMS and glass wafer is weakest near the metalized electrodes, which can result in bond failure and leakage of liquid and gas near the electrodes. To improve robustness of the design and to potentially mitigate the need to continually adjust the gas pressure in order to maintain a stable MB diameter, it may be worthwhile to consider alternative materials for liquid/gas phase delivery and FFMD construction. In particular, fused silica capillary tubing exhibits minimal elastic deformation in response to increased pressure, as has been used as conduit in high-pressure FFMD applications³². Similarly, the FFMD channels may be etched in glass or silica to yield a rigid, non-compliant design with high bond strength.

Another noticeable phenomenon observed when modifying the MB diameter was the difference in the system's step response when enlarging or shrinking the MB diameter. When using a step of same size ($2 \mu\text{m}$), the settling time when enlarging the MB diameter was approximately three times less than when reducing the MB diameter. The observed

difference in settling time is due to the working principle of the pressure regulator, which depressurizes much slower than it pressurizes. To rapidly reduce the MB diameter, a quick drop in pressure is required. Therefore, it is possible to insert an electronically controlled pressure-relief valve to accelerate depressurization. However, this scheme requires the coordination of two actuators, and the pressure-relief valve should only be activated when the setpoint diameter is lower than the previous setpoint. This is a feasible extension of the system studied in this chapter, and may be required for some applications.

During MB production, a large change of input gas pressure led to instability of the system. An immediate jump in gas pressure larger than 2 kPa or multiple jumps of pressure larger than 5 kPa resulted in the production of polydisperse microbubbles or gas thread blowing through the nozzle. To avoid the production of polydisperse MBs or gas blow-through, multiple small step increases or decreases in MB diameter (Fig. 2.9) were implemented to address the problem. A more sophisticated control method, not implemented here, could be a ramped transition of MB diameter, rather than a stepped transition. A feasible way to achieve this is to linearly update the setpoint diameter at each measurement. Notably, the demodulated signal is an appropriate indicator of abnormal FFMD operation. The \bar{V}_{max} value and its deviation are useful to determine whether the FFMD is producing monodisperse, polydisperse or no MBs. If the FFMD enters into an abnormal state, one possible recovery method would be to constrain the gas and liquid supply and reinitialize the system.

Alternative on-chip measurement approaches exist for detecting and measuring particle size, including optical techniques based on light-scattering or light-blocking in

the detection region of a FFMD^{109,110}. However, the advantages of using an electrical method are that it enables: (1) miniaturization beyond that which is possible for optical based approaches, (2) robust operation without dependence on precise optical alignment, (3) and facile integration into medical catheters to enable remote operation for intravascular treatment. Additionally, Coulter-based methods are likely lower-cost and more reliably manufactured than optical-based approaches.

I elected to use an electronic gas regulator as the actuator of the feedback control system. Feedback by adjusting the liquid flow rate is an alternative method that was not studied in this chapter, but is likely equally as effective. Though the motivation for the development of a feedback control system stems from our target application of sonothrombolysis, the method can be implemented in any on-chip setting that requires real-time monitoring and control over microfluidic particle production.

2.5 CONCLUSION

In this chapter, a closed-loop feedback control system was implemented in a benchtop FFMD with an integrated μ CPC. The device was fabricated using micro-fabrication methods and demonstrated production of MBs between 13 and 28 μm . The μ CPC detected the passage of MBs and the electrical signal was captured simultaneously with optical images. Simulation informed the relation of the MB diameter and the maximum impedance, so that the time-averaged maximum voltage was extracted from the electrical signal and fit into a cubic polynomial with optically determined diameter. The empirical relationship between electrically and optically determined diameters were measured and validated, enabling the real time measurement of MB diameter. A PI feedback con-

troller was incorporated into the system and adjusted the input gas pressure to control the MB diameter. Different parameters were implemented and the responses were characterized. The recorded pressure indicated the MB diameter from the FFMD design was associated with the change rate of pressure. Further, by multiple setpoint scheme, MB diameters were varied from 14 to 24 μm . The implementation of this method provides the advantage of blind operation without a microscope.

In vivo quantification of deep vein thrombosis using high-frequency ultrasound imaging

3.1 INTRODUCTION

3.1.1 DEEP VEIN THROMBOSIS

Deep vein thrombosis (DVT) is a life-threatening condition that can lead to its sequelae pulmonary embolism (PE) and post-thrombotic syndrome (PTS), affecting over one million people in the United States annually³⁴. The development of a thrombus in DVT obstructs blood flow, induces clinical manifestations such as edema, venous hypertension with pain, ulceration, and has a detrimental effect on the quality of life of a patient¹¹¹. DVT results in the use of extensive health resources and considerable social costs (7 to 10 billion dollars per year in the United States)¹¹².

Ultrasound is widely used in the detection of suspected DVT^{48,49}. Doppler ultrasound or pulsed wave ultrasound is used to determine the existence of blood clots when blood

flow is occluded by blood clots and reduced to approximately zero^{113,114,115}. However, in the field of rodent models of DVT, there is still a lack of a standard approach to the quantification of blood clots. Previous studies have used a recanalization rate or blood flow restoration rate derived from two-dimensional (2D) Doppler/power Doppler ultrasound to qualitatively assess the efficacy of a treatment, such as a recombinant tissue plasminogen activator (rt-PA)^{113,114}. The blood flow velocity in pulsed wave ultrasound has been used to assess the influence of DVT^{116,117}. However, it is highly dependent on the measured location and parameters, such as the Doppler angle. Alternatively, the weight of the blood clots or the macroscopic observation of the length and width of the thrombus can be used as a quantitative measurement. This approach requires the harvest of clots from animals, which is a termination procedure^{118,119}. Recent advances in high-resolution microscopic imaging have enabled the *in vivo* visualization of venous thrombus formation^{120,121,122}. It is suitable for imaging the formation of DVT in a short time frame, since the vessels of mice must be exposed to light excitation. The invasive nature of surgery may restrict the use of this technique in research that involves multiple days of observation, or thrombolysis of sub-acute or chronic DVT.

Researchers frequently use ultrasound imaging-based approaches for the volumetric quantification of blood clots. A novel three-dimensional (3D) imaging protocol has been proposed to evaluate the volume echogenicity of the thrombus and has been validated in clinical patients^{50,51}. Additionally, a flow system was reported to assess *in vitro* thrombus volume during thrombolysis¹²³. These studies obtained sequential 2D slices and generated estimates of 3D volume of blood clots of clinical patients or *in vitro* models. Volumetric quantifications outperform 2D area-based methods, as they

take into account the irregular shape of blood clots and do not require the imaging plane to be exactly aligned with the previous position^{124,116}. Driven by these advantages, this work is the first application of 3D ultrasound examination of DVT assessment in murine models. It is distinct from previous research due to its requirement for a higher resolution than in clinical patients. Compared to existing *in vitro* models, imaging in *in vivo* models is challenging, as the surrounding tissues of the vessels may result in imaging artifacts or reduced contrast for DVT. This non-invasive ultrasound imaging technique can be used to further evaluate the most effective way to remove DVT by conducting thrombolysis studies in murine models.

In this chapter, I present a 3D ultrasound approach for the quantitative assessment of a clot in a mouse model of DVT. To validate this quantification method, blood clots were first made and imaged using 3D ultrasound in an *in vitro* circulating system. The measured volume of blood clots was segmented and compared with their weight. The next step was to apply the approach *in vivo* in a mouse model of DVT and to make a comparison between the 3D volume of the blood clot from ultrasound and the macroscopic measurement at harvest. This work is significant in that it provides the first evidence that 3D ultrasound volume can be used as a non-terminating metric for assessing clot volume in a rodent DVT model.

3.2 MATERIALS AND METHODS

3.2.1 *IN VITRO* BLOOD CLOT MODEL

The experimental apparatus of the *in vitro* flow model is illustrated in Figure 3.1(a). *In vitro* Blood clots were formed using the addition of 15 mM Calcium chloride into 3.8%

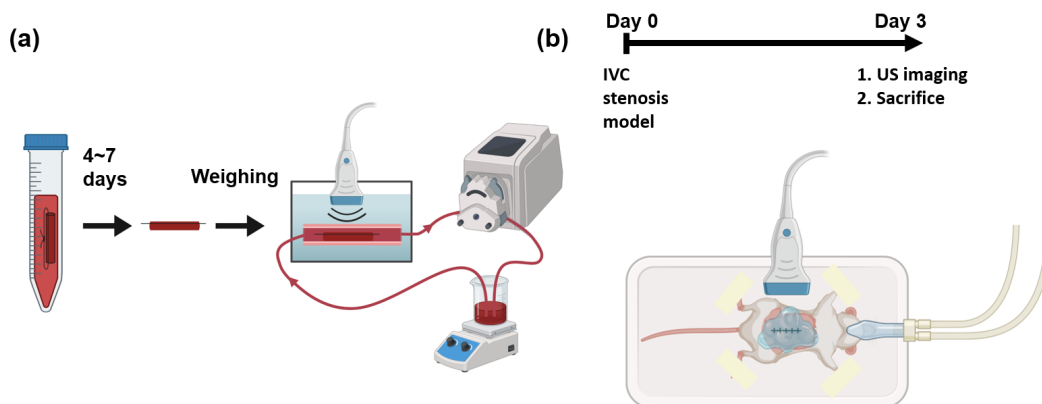


Figure 3.1: Schematic of experiments and imaging setups. (a) An *in vitro* blood clots is fabricated and kept in refrigerator for 4 to 7 days. The weights of the blood clots are measured before running in a flow loop. The blood clots in whole bovine blood are imaged by a 3D ultrasound system. (b) A mouse of inferior vena cava (IVC) stenosis model undergoes surgery at day 0. At day 3, the mouse is imaged using a 3D ultrasound system before sacrifice.

citrated whole bovine blood (HemoStat Laboratories, Dixon, CA) in 15 mL Polypropylene Conical tubes to reverse anticoagulation^{125,31}. The mixture was placed with 2.5 mm diameter Borosilicate glass tubes and sutures were tied through the tubes. The mixture was incubated in 37 °C for 4 h. After 4 h, the samples were kept at 4 °C for 3 to 7 days to promote clot retraction^{126,127}. Before experimentation, the clots were removed from the glass tubes but remained attached to the sutures. The weights of the clots were recorded after subtracting the weights of sutures of the same length that were inside the clots.

An *in vitro* experimental apparatus was employed to simulate the physiological environment of DVT. The apparatus was submerged in 37°C water bath. The blood clot with sutures was fixed in a segment of 3-mm-inner-diameter 0.2-mm-thin-walled polyolefin tube (H&PC-58727, Sopoby, Zhejiang, China). Whole bovine blood (20 ml) was circulated within the flow loop using a peristaltic pump (NE-9000B, New Era Pump Systems, Inc., Farmingdale, NY). The average velocity in the 3mm inner diameter section was

Table 3.1: Ultrasound imaging parameters in B-mode and Doppler mode.

Parameters	B-mode	Doppler
Frequency	40 MHz	30 MHz
Depth	12 mm	
Width	14 mm	
Resolution (width x depth)	512 × 400 pixels	256 × 200 pixels
Step size	0.03 mm (long axis) / 0.1 mm (short axis)	

47 mm/s, which is approximately equal to the blood flow velocity in the mouse vein¹²⁸. An ultrasound transducer was submerged under water in this apparatus.

3.2.2 MOUSE MODEL OF DEEP VEIN THROMBOSIS

All animal procedures conformed to the Guide for the Care and Use of Laboratory Animals¹²⁹ and study protocols approved by Animal Care & Use Committee (ACUC) at the University of Virginia. C57BL/6 male mice (The Jackson Laboratory, Bar Harbor, ME) approximately 8-10 weeks old were used in this chapter. The mouse vein underwent partial restriction of blood flow with minor modifications from previous articles^{119,124,118}. A midline laparotomy was performed to dissect the IVC. Following permanent ligation of all side branches, a 5-0 Prolene suture string was placed on top of IVC as a spacer, followed by ligation. The spacer was then removed, leading to a partial ligation of IVC below the renal vein. The procedure resulted in a reduction in 90% in the lumen cross section area at the ligation site¹²⁴. The side branches were fully ligated and the back branches were cauterized.

Three days after surgery, ultrasound imaging was performed to measure the volume of blood clot. Ultrasound gel was applied to the abdominal region for coupling. After the imaging session, the clot was harvested for macroscopic measurement.

3.2.3 ULTRASOUND IMAGING

Scanning 3D ultrasound volume can be accomplished by mechanically translating a linear transducer and acquiring 2D frames at each location¹³⁰. The Vevo 2100 system (Fujifilm VisualSonics, Inc., Bothel, WA) was used with an external motor module (Fujifilm VisualSonics, Inc., Bothel, WA) that mounted an MS-550D transducer to acquire 3D volumes of blood clots. During the imaging session, each mouse was fixed on a temperature-monitored heated motion stage (TM150, Indus Instruments, Webster, TX) in the supine position while its nose was flushed under 1.0% v/v isoflurane (Henry Schein, Dublin, OH). The transducer was operated at 40 MHz in B-mode, focal zone of 6 to 8 mm with a 12 mm imaging depth. The location and orientation of the transducer were carefully adjusted to align the IVC within the imaging plane and provide the best image quality. During acquisition, the 3D volume of B-mode and Doppler imaging data was collected to segment blood clots from the background⁴⁸. The step size was 0.03 mm in the long axis (sagittal plane) and 0.1 mm in the short axis (transverse plane), respectively. Ultrasound parameters are listed in Table 3.1. The schematic of the *in vivo* imaging setup is shown in Figure 3.1(b).

3.2.4 THREE-DIMENSIONAL SEGMENTATION OF BLOOD CLOT

The workflow employed a semi-automatic GrowCut segmentation workflow¹³¹, as illustrated in Figure 3.2. Volumetric data in the imaging system were exported to a PC and loaded into 3D slicer software for image analysis¹³². Blood clots and background in a few slices of each direction (X-Z, Y-Z, and X-Y planes) were manually annotated, which was supervised by an expert surgeon. The existence of the blood clot was based on the

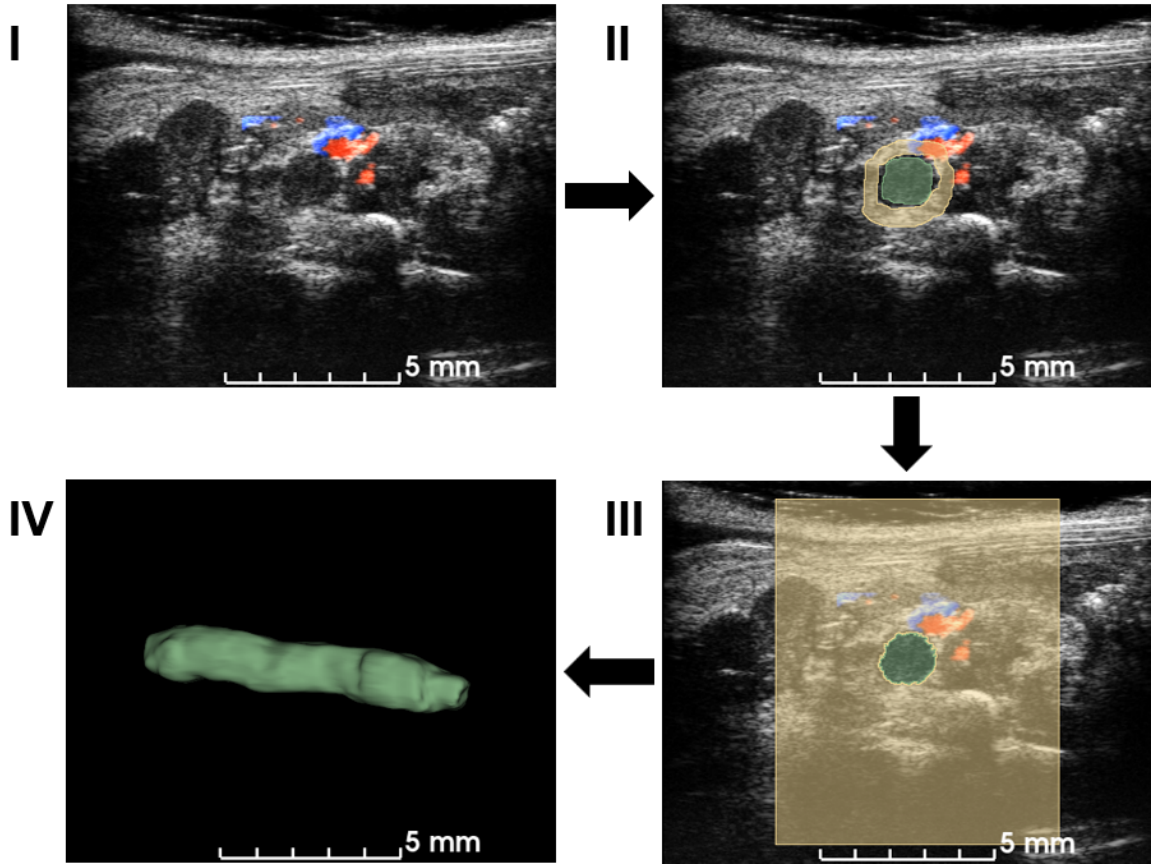


Figure 3.2: Workflow of the semi-automatic 3D segmentation. First, Ultrasound volume is loaded into 3D Slicer (I). Manual segmentation is performed in multiple slices and angles, based on B-mode signal density and Doppler blood flow signal in (II). A seeding algorithm is run and modifications are applied to extract a 3D volume of a blood clot in (IV). After the segmentation, the volume of the blood clot is calculated for quantifications.

static texture and Doppler blood flow signals. After accumulating more than 30 annotations, a growing-from-seeds algorithm was run on a 3D slicer to segment the volume of the 3D blood clot¹³¹. After smoothing the boundary to the volume of 3D blood clots provided in the software, the volume of the blood clots was measured as a quantification metric.

As an alternative, a cylindrical volumetric estimation of the blood clot was used from macroscopic photos. The volume of the blood clot was calculated¹³³

$$V = \frac{\pi}{4} D^2 L \quad (3.1)$$

where D and L are the diameter and length of the blood clot, respectively. The diameter in the macroscopic measurement included the thickness of the vein wall. To correct the blood clot diameter, vein wall thickness was estimated from ultrasound acquisition and subtracted from the macroscopic diameter.

3.2.5 DATA ANALYSIS

The statistical analysis was performed using MATLAB (2021a, Mathworks, Natick, MA). The Pearson correlation coefficient between blood clot volume and weight was calculated using the inbuilt MATLAB *corrcoef* function, so as between *in vivo* blood clot volume and blood clot length from macroscopic measurement¹³⁴.

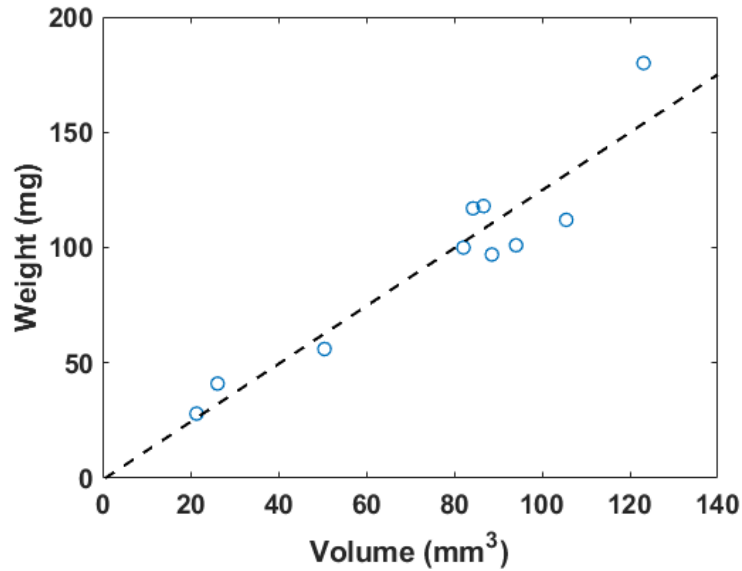


Figure 3.3: The correlation plot of *In vitro* blood clot weights versus 3D segmentation volume, where $R^2 = 0.89$. The dashed line represents the linear regression result.

3.3 RESULTS

3.3.1 THREE-DIMENSIONAL BLOOD CLOT VOLUME AND WEIGHT

The weights measured before the flow loop and the total volumes are plotted in Figure 3.3. The inner diameter of the tubes holding the blood clots was 2.5 mm, to ensure that the blood clots can be placed within the flow loop system. The weights of the blood clots ranged from 28 to 180 mg. The 3D volume measurement of the blood clot generated from the workflow described in Figure 3.2 varied from 21 to 123 mm³. The dimension of blood clots was optimized for the field of view of the transducer and the limit of the 3D motion module.

The fitting linear relation between the weight (W) in mg and the 3D segmentation

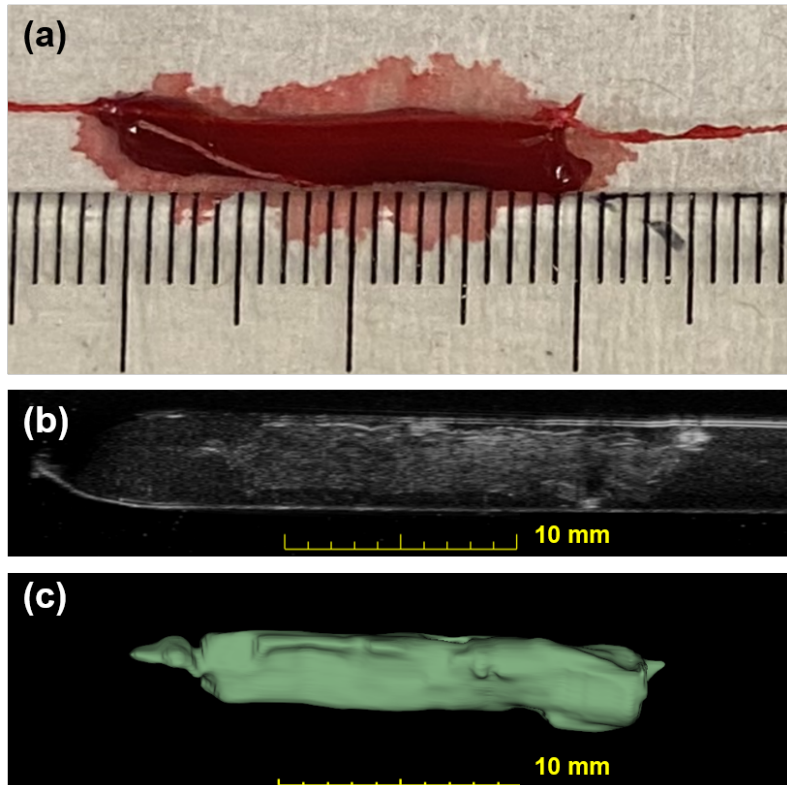


Figure 3.4: Photographic and ultrasonic examples of a bovine blood clot. (a) A photo of an *in vitro* blood clot. Each small tick of a ruler equals to 1 mm. (b) One slice across the corresponding 3D US volume approximates the previous photo in (a). This clot has a weight of 101 mg and a volume of 94.1 mm³. (c) The output segmentation volume of the clot is shown.

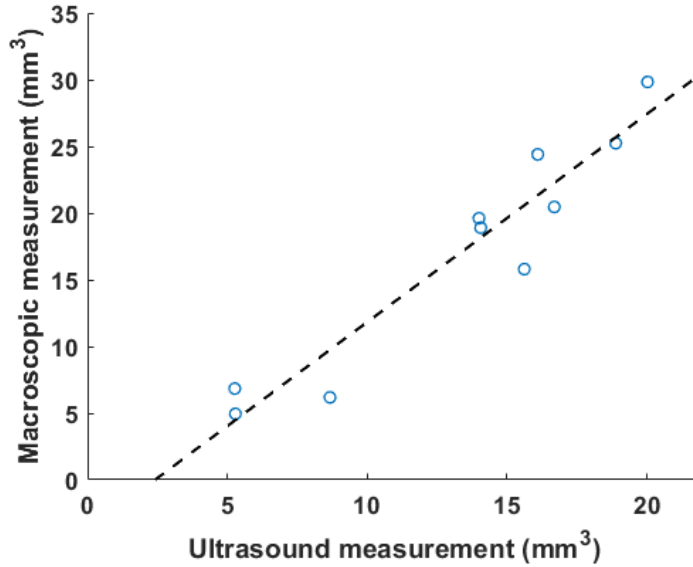


Figure 3.5: A correlation plot of *in vivo* results between volumetric measurement using ultrasound and macroscopic observation is plotted, with $R^2 = 0.91$. The dashed line is the linear fitting result.

volume (V) in mm^3 is described as:

$$W = 1.2556V - 0.7375. \quad (3.2)$$

The R^2 for this linear fitting is 0.89. Figure 3.4 shows a photo of a blood clot, with a mass of 101 mg and a volume of 94.1 mm^3 . A cross-sectional slice is extracted in the 3D ultrasound volume after linear transforms. The texture and intensity difference distinguish the boundary of the blood clot from the background blood flow. The reconstruction of the 3D blood clot preserves correct geometry. Therefore, 3D ultrasound scanning is a suitable quantification readout to assess blood clot volume in non-transparent fluid media.

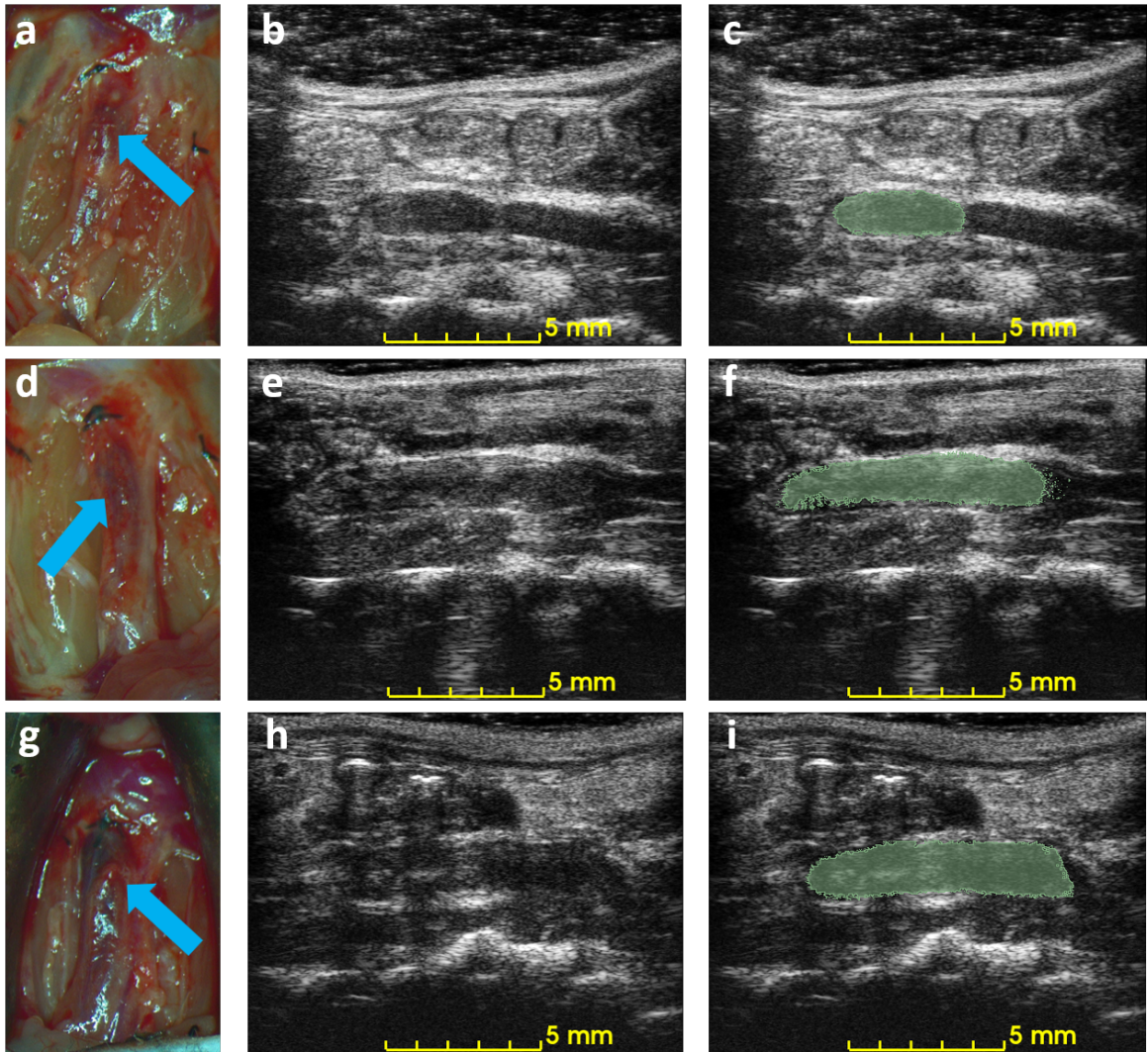


Figure 3.6: Example of macroscopic photos and ultrasound imaging on day 3. Each row is the macroscopic photo (a, d, g), the ultrasound image (b, e, h), and the ultrasound image with an overlaid mask of the blood clot (c, f, i), of each mouse. Arrows indicate the location of the detected blood clots in macroscopic photos.

3.3.2 CHARACTERIZATION OF THROMBUS IN MOUSE OF IVC STENOSIS MODEL

Figure 3.5 shows the correlation between ultrasound volume and macroscopic observation. The volume of blood clots segmented from 3D ultrasound acquisition in mice ($N = 10$) ranged from 5.3 to 20.0 mm³, and the mean volume was 13.5 mm³. Meanwhile, the cylindrical volumes of the macroscopic measurements ranged from 5.0 to 29 mm³, after removing the mean thickness of the vein wall of 105 μm from the macroscopic measurement. The correlation coefficient R^2 is 0.91. The root mean square error for this linear regression is 2.51 mm³. Three examples of ultrasound imaging slices and their corresponding photos are shown in Figure 3.6. The thrombi are indicated with arrows in macroscopic observations and highlighted with light green masks in ultrasound imaging, shown in Figure 3.6.

3.4 DISCUSSION

In this chapter, a blood clot quantification method was developed to measure volume based on 3D B-mode and Doppler ultrasound imaging data. The 3D measurement method was applied to an *in vitro* flow loop model and a murine model with partial ligations. The volume of blood clots using a semiautomatic 3D segmentation algorithm was validated in the *in vitro* flow loop against their weight in volumes of 21.4 to 123 mm³ and weights of 28 to 180 mg, respectively. In the murine model, eight volumes of DVT from 5.3 to 20.0 mm³ were validated with macroscopic measurements.

Blood clots share similar density and incompressibility to water, which is one of the foundations for such a measurement. Vessels such as IVC can be pressed and deformed.

Most previous studies used color Doppler or pulsed-wave ultrasound to qualitatively determine the existence of blood clots^{113,114}. To quantify changes before and after blood clot treatment, two-dimensional area-based measurements have also been performed as an output metric¹²⁴. The selection of 2D slice location is also subject to the operator's expertise, and this benchmarking method does not take into consideration the irregular shape of the DVT outside of the imaging plane. Today, macroscopy is widely used to characterize a clot^{118,119}. In our experiment, the volume of 3D ultrasound acquisition was compared with the macroscopic measurement. The cylindrical model of macroscopic measurement oversimplified the geometry of a blood clot¹³³. The width of blood clots can vary from the center to the edges, and the shape of the cross-section of blood clots in the short-axis view may not be circular. Finally, similar to the weighing method, it required the termination of mice. The above restrictions cause it to be an imprecise measure for quantifying blood clots, resulting in a larger volume than a genuine 3D technique. In Figure 3.5, the slope of the linear regression (1.4) is greater than 1. Unlike existing methods, the 3D volume method proposed in this chapter was deformation-tolerated and was not subject to operations during acquisition. The abdominal area was completely recorded with a small step size and a segmentation algorithm was run after acquisition. The high correlation coefficient (Figure 3.5) of 0.91 suggests that the 3D ultrasound volume method is a reliable measurement of DVT. Though all animals were treated with the same procedures, the blood clot volumes in Figure 3.5 are not evenly distributed within the range of 5 to 20 mm³ due to individual variability in the formation of the thrombus^{119,124}.

The 3D acquisition method can reduce the required number of animal subjects. Ul-

trasound is a non-invasive imaging technique that can be used to observe mouse IVC thrombus without causing any adverse effects, enabling the same subject to be monitored before and after treatment. The difference in volume is a reliable quantification of the efficacy of treatment in mice. A qualitative result or harvesting at each time point requires a larger number of mice in such an experiment. The use of 3D ultrasound in other medical conditions, such as plaque and Abdominal Aortic Aneurysm, is already established^{135,136,137}. However, 3D ultrasound is novel for assessing the rodent model of DVT, in which there is still no standard criterion for assessing DVT in a murine model. The proposed method has the potential to benefit DVT-related pharmacological or therapeutic *in vivo* studies by providing reliable quantified measurements throughout the treatment without any termination procedure. The difficulties of ultrasound imaging in the IVC thrombus are: (1) obstructions from scarring, air, or food, for example, Figure 3.6h; (2) false color Doppler signals from the adjacent aorta; (3) absence of color Doppler signals due to slow blood flow. The challenges mentioned above, if not addressed, can affect the detection of DVT boundary and lead to an inaccurate measurement, especially in traditional 2D B-mode ultrasound¹³⁸. Acquisitions of 3D ultrasound provide additional data for thrombus evaluation, partially alleviating these concerns.

When the contrast of IVC ultrasound images was not sufficient, I employed some alternatives to ensure good imaging quality in mouse imaging. (1) Change the applied pressure of the transducer. The IVC was imaged at a different axial distance; (2) Change the imaging site. Shadowing of the ultrasound signal can be caused by air or food particles swallowed. I tilted the transducer angle away from the original plane where there were degrading imaging artifacts during data acquisition. These compensations miti-

gated the lack of signal contrast, thus reducing the chance of overestimation or underestimation of the volume of blood clots.

Occasionally, Color Doppler imaging produces unreliable results, which can be caused by slow blood flow¹³⁸. B-mode data were considered with color Doppler images simultaneously to avoid inaccurate segmentation. One sophisticated way to separate the static blood clot and tissue region from the dynamic blood flow is to apply a singular value decomposition (SVD) analysis to a multi-frame data set at each position¹³⁹. Therefore, it requires a longer acquisition time and a programmable system, which can collect multiple frames at the same location between each mechanical translation. Another imaging technique that can be used is ultrasound elastography¹⁴⁰. It can differentiate between blood clots and background due to the significant difference in stiffness. Recently, advances in deep learning enable automatic segmentation of DVT without annotations, which can be adopted and applied in the murine model in the future to simplify the procedure^{141,142}.

The seeding algorithm in Figure 3.2 needed a small number of manual annotations for the thrombus and background. It was mainly based on texture and intensity in the volumetric data. Segmentation of the blood clot did not guarantee a smooth boundary. After running the algorithm, I modified the mask to remove discrete clusters and cover the missing region. These modifications can generate a smoother 3D surface for blood clots.

The widely used Duplex ultrasound has been proved to be a reliable and accurate technique to detect DVT^{48,49}. To translate the proposed measurement method into clinical settings, an appropriate 3D ultrasound scheme is recommended. Existing 3D ultrasound

measurements of DVT are based on the mechanical movement of the probe ^{51,50}. This mechanical movement can be achieved by either an internal or external translation module, or by performing a freehand scan. Motion correction techniques can be used in cases where there is substantial motion ¹⁴³. Advances in 2D matrix arrays have the potential to measure the volume of DVT in a single acquisition. However, 3D ultrasound imaging using a matrix array is usually associated with reduced resolution and demanding computational power for beamforming ¹⁴⁴. It is important to address these concerns before clinical applications.

3.5 CONCLUSIONS

I have demonstrated a quantification method for DVT in an *in vitro* model and a murine model. The quantification method involved the use of a 3D ultrasound acquisition system and semi-automatic segmentation of a blood clot. The volume measured by ultrasound was validated with the weight of *in vitro* blood clots and the optical observation of *in vivo*. The correlation coefficients in the *in vitro* and *in vivo* models were 0.89 and 0.91 respectively, indicating a strong correlation. The technique does not require the euthanasia of animals and is non-invasive. The DVT volumes calculated using this method vary from 5 to 20 mm³. We anticipate that 3D ultrasound measurement will be used to quantify pharmacological or therapeutic studies in murine models. The proposed method can accurately measure DVT and improve the data quality of future research.

Efficacy of in vivo sonothrombolysis using microfluidically produced microbubbles in a mouse model of deep vein thrombosis

4.1 INTRODUCTION

It is estimated that there are more than one million cases involving venous thromboembolism (VTE) annually in the United States. These cases include deep vein thrombosis (DVT) and pulmonary embolism (PE)³⁴. DVT not only contributes to high healthcare expenses¹¹², but also remains responsible for a one-year mortality rate of 20%¹⁴⁵. Furthermore, the occurrence of DVT and its sequelae can cause considerable disability and impaired quality of life in individuals after experiencing DVT^{146,147}. Successful treatment of DVT has been shown to be vital in improving long-term outcomes in patients^{148,149}.

Standard therapies for acute VTE include oral anticoagulants and reperfusion¹⁵⁰.

With the wide use of oral anticoagulants in clinics, a common side effect is hemorrhage in patients with VTE^{151,152,153}. Meanwhile, systemic infusion of thrombolytic medications, such as recombinant tissue plasminogen activator (rt-PA), results in major bleeding in approximately 3.5% of the patients^{154,155}. It is now more widely accepted that catheter-directed thrombolysis (CDT) delivers smaller doses of thrombolytic agents than systemic infusion for rapid thrombus dissolution^{156,157}. However, the large-scale randomized ATTRACT trial did not show evidence of improvements in pharmacomechanical CDT (PCDT; CDT with the use of mechanical thrombectomy devices) over oral anticoagulation alone in two-year post-thrombotic syndrome (PTS) occurrence (47% PCDT vs 48% No-PCDT, $p = 0.56$)^{39,40}. PCDT/CDT should be reserved for highly selected patients with severe symptoms and low bleeding risk. In light of the observations in CDT, there is a need for a safer and more efficient catheterization technique to achieve complete or partial resolution of venous thromboembolism without the risk of hemorrhage.

The use of ultrasound (US) has been demonstrated to enhance the delivery of thrombolytic medications and contrast agents, such as microbubbles (MBs), into blood clots, through acoustic radiation force^{158,159}, microstreaming^{160,161} and cavitation^{78,162,163}. In this regard, ultrasound-facilitated thrombolysis, known as sonothrombolysis, has been explored extensively to accelerate blood clot dissolution¹⁶⁴. The safety profile of such ultrasound-assisted approaches, including intravascular catheter-based ones, has been widely documented¹⁶⁵. Multiple studies have documented the potential of sonothrombolytic therapies in the *in vitro*, *in vivo*, and *ex vivo*^{166,167,116,165}. Unfortunately, recent clinical trials have yielded mixed results. While ultrasound-assisted therapies could

similarly dissolve DVT, the available evidence did not show significant advantages over CDT therapies¹⁶⁸. A meta-analysis of clinical trials found that the commercial scheme of ultrasound-accelerated catheter-directed thrombolysis (UACDT) without MBs may not be the preferred option due to its prolonged intervention time and marginal improvement in terms of lysis rate¹⁶⁸. Collectively, the suboptimal efficacy of existing therapies testifies to the need for further research efforts in improving and refining sonothrombolysis.

Recently, our laboratory has reported sonothrombolysis using large microfluidically produced MBs ($>15\ \mu\text{m}$ diameter)^{31,32}. In the *in vivo* study, a 3.3 fold reduction in rt-PA dose was allowed in this stroke model. These studies used a low duty factor ($<10\%$), focusing solely on the mechanical effects of ultrasound, which decreased the thermal effect.

In this context, there is still an unmet need to validate the efficacy and safety in sonothrombolysis using large MBs through the use of *in vivo* models of DVT, as the mechanical properties and aging of thrombus could vary significantly from prior studies^{169,170}.

In this chapter, I investigated the therapeutic efficacy of sonothrombolysis using large microfluidically generated MBs in a mouse model of pre-existing DVT. It was the first *in vivo* study to evaluate the influence of ultrasound and microfluidically produced MBs on venous thromboembolism. For this objective, MBs from a flow-focusing microfluidic device was generated *in situ* and administered to animals through venous catheterization. Microfluidically produced MBs dissolved rapidly in blood flow, thus resulting in limited off-target bioeffects. Changes in blood clot volume were monitored by three-

dimensional (3D) ultrasound imaging. Based on existing research on CDT in DVT therapy, sonothrombolysis using large microfluidically produced MBs was hypothesized to effectively dissolve the venous thrombus.

4.2 METHODS

4.2.1 FABRICATION OF MICROBUBBLES VIA MICROFLUIDICS

The mold for the microfluidic device was fabricated using the photolithography method, as described in previous research^{30,171}. The device was poured into the SU-8 mold with polydimethylsiloxane (PDMS), and assembled with a clean 500- μm -thick glass wafer. The microfluidic channel had a height of 20 μm and a nozzle width of approximately 7 μm .

MBs were produced using a gas phase of 99.995% Nitrogen (Linde Gas, Richmond, VA, USA) and a liquid phase of bovine serum albumin (4% w/v), dextrose (10% w/v) in 0.9% saline¹⁷¹. The flow rate of the liquid phase was 20 $\mu\text{L}/\text{min}$ supplied by a syringe pump (PhD 2000, Harvard Apparatus, Holliston, MA, USA), and the setting pressure of the gas phase was fixed at 84.8 kPa using a gas regulator (PC-series, Alicat Scientific, Tucson, AZ, USA). The inlets and the outlet of the microfluidic device were connected through 30-gauge inner diameter polytetrafluoroethylene (PTFE) tubings (Cole-Parmer, Vernon Hills, IL, USA). The operating parameters were verified to produce MBs in the microfluidic device under a high-speed camera (SIMD24, Specialised Imaging, Tring, UK), optimized as the existing literature³¹.

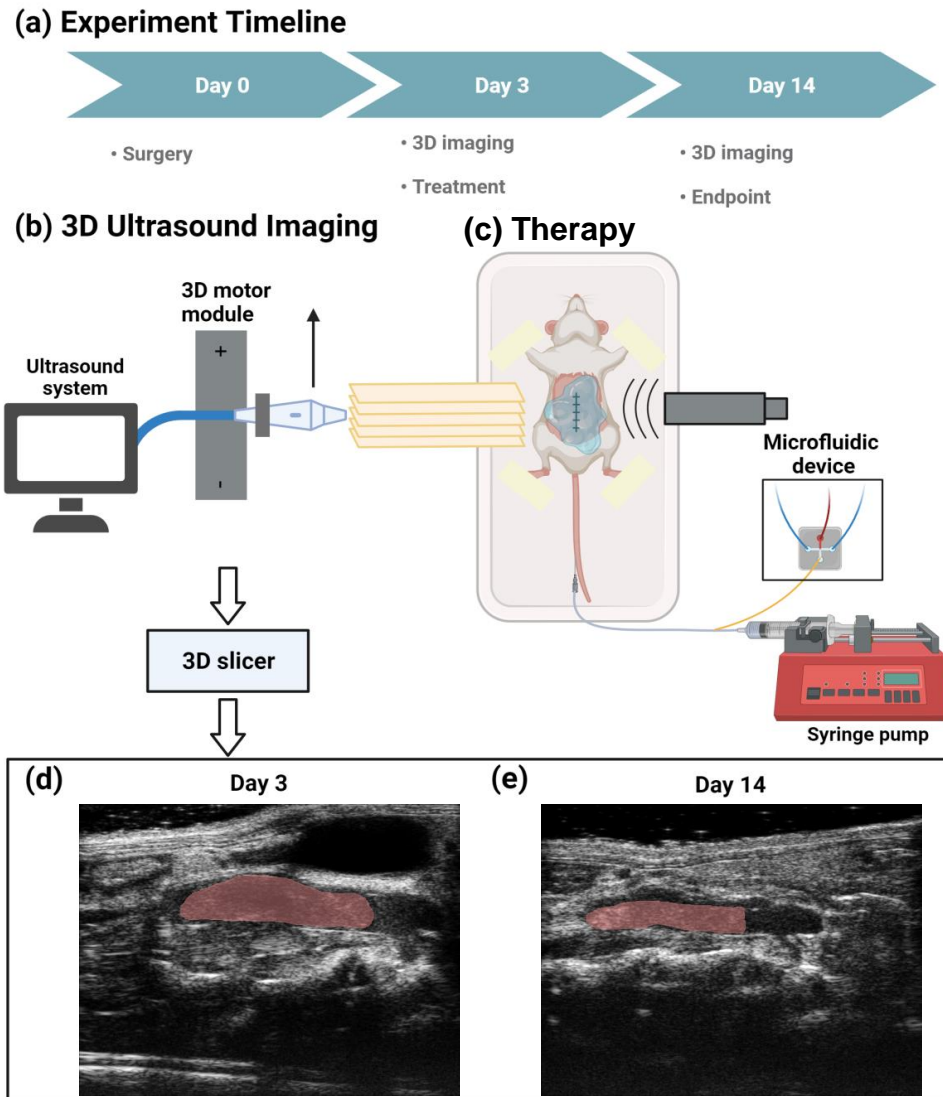


Figure 4.1: (a) Experiment timeline: the animals underwent surgery of partial ligation to develop thrombus on Day 0; 3D ultrasound imaging was performed on Day 3, followed by a therapy; Another 3D ultrasound imaging was conducted on Day 14. (b) Two-dimensional slices of both long axis and short axis view of the inferior vena cava (IVC) were acquired at different vessel cross-sections. Data were exported to 3D Slicer software for segmentation. (c) A therapy to mouse model of DVT. Microfluidically produced MBs and thrombolytic drugs were administered through a tail vein catheter, while ultrasound was applied from the top of the mouse abdomen. Comparison of DVT in the IVC was shown in (d) and (e), on Days 3 and 14, respectively. The red region indicated the location of thrombus.

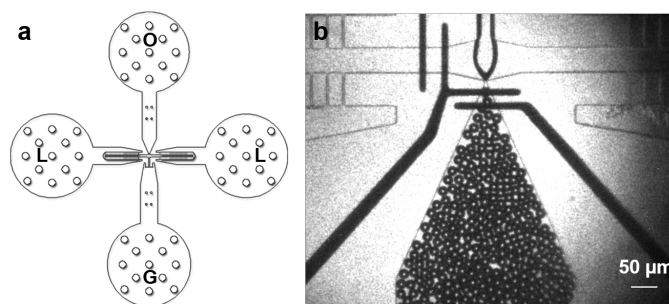


Figure 4.2: (a) Layout of a flow-focusing microfluidic device. G: gas inlet, L: liquid inlet. O: MB outlet. (b) A photo of generated MBs under a high speed camera. The mean diameter of MBs was $18.0 \mu\text{m}$

4.2.2 ULTRASOUND IMAGING

All animal experiments followed the guidelines outlined in the Guide for the Care and Use of Laboratory Animals¹²⁹ and were conducted in accordance with the approved study protocols by the Animal Care & Use Committee (ACUC) at the University of Virginia (Protocol 4327-09-23). As described in previous literature¹⁷², a high-frequency ultrasound imaging system, Vevo 2100 (FUJIFILM VisualSonics, Toronto, ON, Canada), equipped with a linear array probe MS-550D (40 MHz center frequency) was used to acquire data. The animals were placed on a $37 \text{ }^{\circ}\text{C}$ temperature control platform and anesthetized with 1.5% v/v isoflurane. The abdomen of the mice was shaved and treated with ultrasound gel to improve imaging quality. The transducer mounted on a 3D motor module (VisualSonics, Toronto, ON, Canada) captured long-axis slices of mice at a step size of 0.03 mm using B-mode and color Doppler mode. The acquisition was also repeated for the short-axis slice at a step size of 0.1 mm. The 3D data collected were saved for further image analysis.

The saved 3D data were exported to 3D Slicer software¹³² for annotation and segmen-

tation. After manually labeling multiple two-dimensional (2D) slices for a blood clot and background at each view, a grow-from-seeds algorithm was run to semi-automatically segment the blood clot¹³¹. The volume of the blood clot was then calculated as an output metric.

4.2.3 DELIVERABILITY STUDY OF MICROFLUIDICALLY PRODUCED MICROBUBBLES IN MICE

A preliminary investigation was conducted to determine the deliverability of microfluidically produced MBs from a venous catheter to the IVC. Healthy male C57BL/6 mice (8-12 weeks old) were anesthetized with 1.5% isoflurane and placed on a heated 37 °C platform. Microfluidically produced MBs were administered to the tail vein through a catheter for 30 seconds. B-mode videos were recorded using the ultrasound imaging system described above at 0, 100 and 360 seconds after administration.

Table 4.1: Summary of experimental groups

Group	N	rt-PA	ultrasound	microbubbles
A	4	+	+	+
B	4	+	+	-
C	4	+	-	-
D	4	-	-	-

4.2.4 MOUSE MODEL OF DEEP VEIN THROMBOSIS

A murine IVC partial ligation model was utilized to mimic the venous stenosis/insufficiency and induce the development of DVT, as previously described^{119,124,118}. In total, forty 8-to-12-week old male C57BL/6 mice (The Jackson Laboratory, Bar Harbor, ME, USA)

were anesthetized and underwent a midline laparotomy on Day 0. A 30-gauge needle was placed above the IVC as the spacer, and a suture was used to ligate the IVC immediately below the venal vein. The ligation allowed for a 90% closure of the IVC lumen, which resulted in thrombosis without endothelium denudation. After removal of the needle/spacer and wound closure, the mice were recovered and monitored for postoperative care.

The animals were randomly divided into four different therapeutic treatments upon confirmation of DVT development on Day 3 post IVC stenosis, an intermediate time point suggested by¹¹⁴. After 3D ultrasound scanning and reconstruction of the thrombi volume, animals were subjected to the aforementioned therapy session lasting 30 minutes. Animals in groups A, B, and C were catheterized by an experienced technician and received an injection of 2 mg/kg rt-PA (Activase, Genentech, South San Francisco, CA, USA)¹¹³, while group D was a no-therapy control. The rt-PA dose was administered for a period of 30 min, with an initial bolus of 10%. In groups A and B, a 1-MHz center frequency Panametrics ultrasound transducer (A303S, Olympus Panametrics, Waltham, MA, USA) was placed on the abdomen of mice coupled with ultrasound gel and continuously transmitted energy at a pulse repetition frequency (PRF) of 1 kHz and a duty factor of 2% during the therapy session. The low duty factor allowed for the perfusion of MBs and avoided thermal effects. The transducer was calibrated in a water tank and observed to produce a peak-negative pressure of 574 kPa, at a distance of 7 mm from the transducer surface. US parameters remained consistent with the calibration. Group A received microfluidically produced MBs for 30 s, every 5 min, as illustrated in Fig. 4.1. The average diameter of the MBs was measured as $18.0 \pm 1.1 \mu\text{m}$ (mean \pm SD),

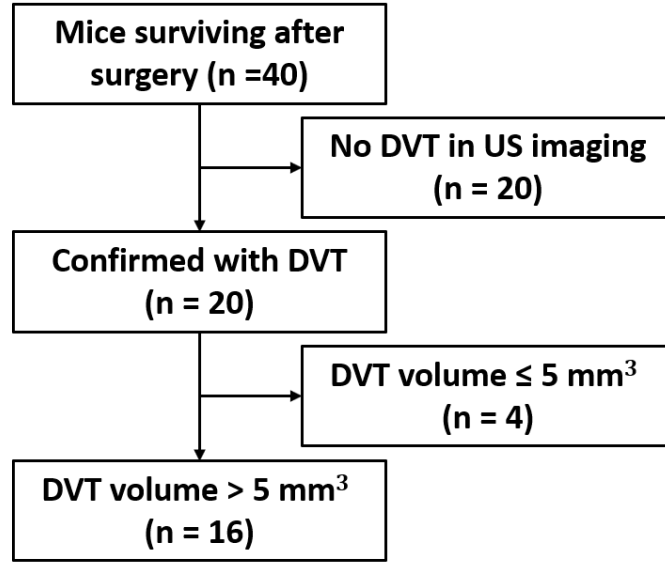


Figure 4.3: Flow diagram of mice enrollment.

while the production rate was estimated to be 90.3×10^3 MBs per second. Therefore, the total gas volume was approximately $50 \mu\text{L}$.

On Day 14, a second imaging was performed for the animals under anesthesia, followed by euthanasia. IVC were harvested and preserved in formalin for histological purposes. The residual volume (RV) is defined as:

$$\text{RV}(\%) = V_{\text{Day14}}/V_{\text{Day3}} \times 100\%, \quad (4.1)$$

where V_{Day3} , V_{Day14} are the DVT volume segmented from acquired 3D ultrasound data on Days 3 and 14, respectively.

4.2.5 HISTOLOGY

Excised IVC specimens were formalin-fixed and paraffin embedded. Sections of 5 μm were obtained at an interval of 0.1 mm across the samples and stained with hematoxylin and eosin (H&E) stain. Slices were scanned with a Leica microscopic camera (DMi8, Leica Microsystems, Durham, NC, USA). Representative photos of each group were selected and demonstrated.

4.2.6 STATISTICAL ANALYSIS

Statistical analysis was performed using RStudio software (R version 4.2.1). Significance in means among all groups was determined using one-way analysis of variance (ANOVA), followed by post hoc Fisher's least significant difference (LSD) test^{173,174}. The significance level was set at 0.05.

4.3 RESULTS

4.3.1 ULTRASOUND IMAGING ASSESSMENT OF MICROFLUIDICALLY PRODUCED MICROBUBBLES IN MICE

Fig. 4.4 shows the B-mode imaging results in mouse IVC. Microfluidically produced MBs injected from a tail vein catheter enhanced the intensity of the B-mode image at 0 s. Due to circulation and gas dissolution, contrast enhancement weakened along with a reduction in the number of detectable MBs 100 seconds after injection. Eventually, there were no MBs passing through the IVC in 360 seconds, indicating total absorption of the MBs. Microfluidically produced MBs can be delivered to the IVC and serve as a

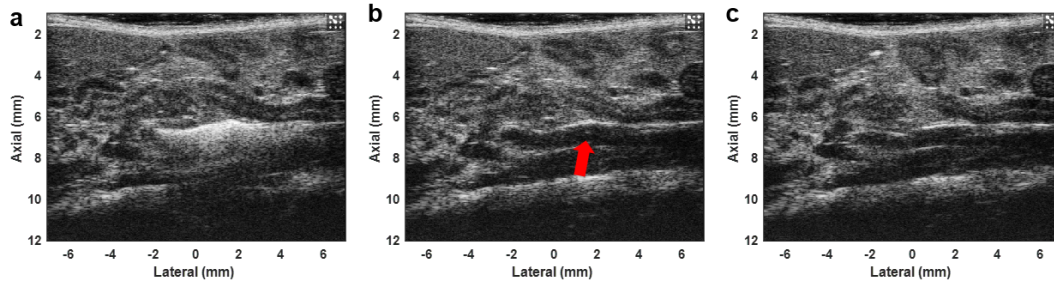


Figure 4.4: US images of IVC at (a) 0 s, (b) 100 s and (c) 360 s after administration of microfluidically produced MBs into the catheter. Cluster of MBs flow in the IVC in (a) and enhanced the image intensity inside the vein. The arrow in (b) shows a single MB traversing in the IVC. No MBs are detected after 360 s.

thrombolytic agent in sonothrombolysis.

4.3.2 MOUSE MODEL OF DVT

Due to the variability inherent to murine models of DVT, not every experimental animal develops thrombosis nor uniformly. In order to focus our studies on animals with pre-existing DVT, a pre-therapy US imaging can screen those mice without DVT. The flowchart of the enrolled mice is presented in Fig. 4.3. In total, 20 mice were confirmed with DVT by color Doppler ultrasound. Only 16 mice with $>5 \text{ mm}^3$ DVT were selected in the experiments. Smaller blood clots can be completely lysed without interventions and the image resolution for them may not be sufficient. The mean volume of DVT in all four groups was 15.9 mm^3 on Day 3.

The volume of DVT was evaluated for mice in each experimental group. Representative differences in DVT volume on Days 3 and 14 are shown in Fig. 4.5, and RVs are plotted in Fig. 4.6. The average RVs of each group were (mean \pm SD): A, microfluidically produced MBs, ultrasound and rt-PA, $20.0 \pm 10.9\%$; B, ultrasound and rt-PA,

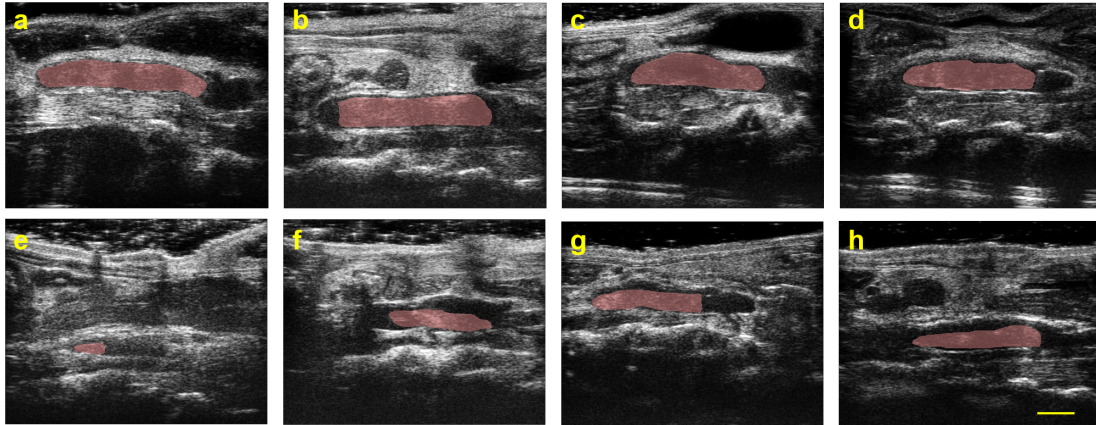


Figure 4.5: Representative ultrasound images in long-axis. The top and bottom rows are the results of Day 3 (a-d) and Day 14 (e-h), respectively. Each column is the same mouse from group A sonothrombolysis using microfluidically produced MBs (a, e), B ultrasound plus rt-PA (b, f), C rt-PA (c, g) and D no-therapy control (d, h). The red overlaid mask is the segmented blood clot. A scalebar of 2 mm is plotted.

45.3 ± 18.0%; C, rt-PA, 50.0 ± 16.1%; D, no-therapy control, 52.2 ± 15.7%.

According to the ANOVA analysis, the average RV for each group was significantly different ($p = 0.0406$). The RV for group A of sonothrombolysis using MBs was significantly different from group B of ultrasound plus rt-PA ($p = 0.0387$), group C of rt-PA alone ($p = 0.0158$) and no-therapy control group D ($p = 0.0121$). Among groups B, C, and D, the RV for group B ultrasound plus rt-PA was not significantly different from group C rt-PA alone ($p = 0.636$) and no-therapy control group D ($p = 0.539$), neither between group C rt-PA alone and no-therapy control group D ($p = 0.886$).

4.3.3 HISTOLOGY RESULTS

Representative images of circumferential IVC samples are shown in Fig. 4.7. The lumen in Fig. 4.7A was observed with a larger space because the residual blood clot was the smallest among all sections. All residual blood clots in Fig. 4.7A-D were attached to the

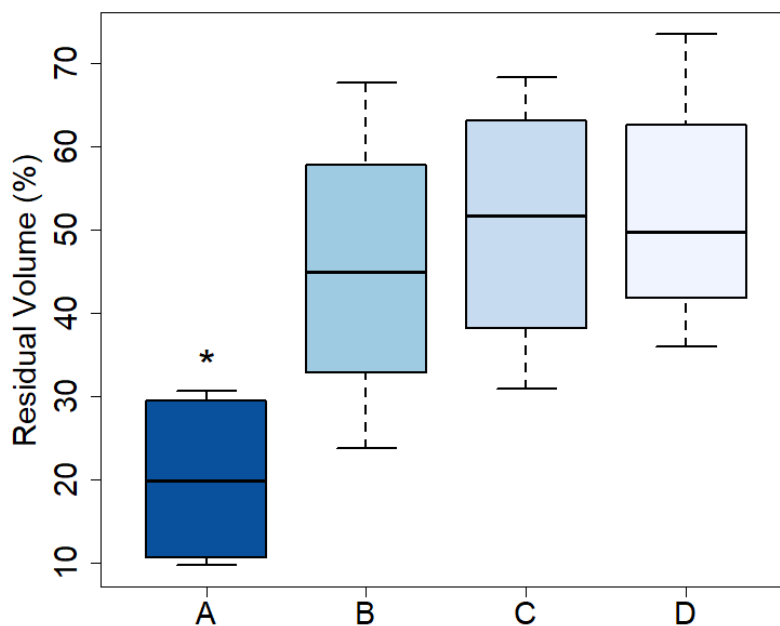


Figure 4.6: Efficacy results of therapies. The residual volume of thrombus from Day 3 to Day 14 in percentage is plotted. The use of large microfluidically produced microbubbles reduces the residual volume of thrombus. The differences in the residual volume for MBs + US + rt-PA (group A) and the other groups (B: US + rt-PA; C: rt-PA and D: no-therapy control) are all statistically significant ($p < 0.05$, LSD test). An asterisk denotes statistical significance of comparison to no-therapy control group D ($p < 0.05$). Additional statistical results are listed in the result section.

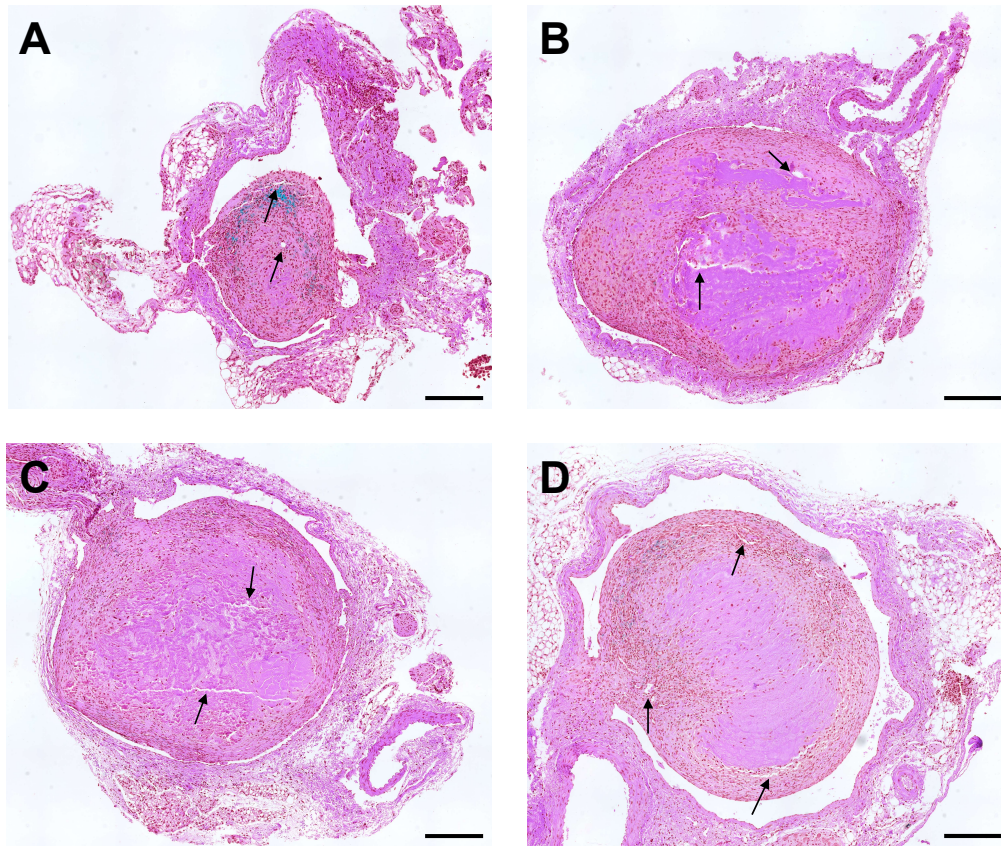


Figure 4.7: H&E staining results in (a) MBs + US + rt-PA, (b) US + rt-PA, (C) rt-PA and (D) no-therapy control groups. Arrows in A-D show the recanalization channels in thrombus. The scale bar responds to 200 μm . H&E, haematoxylin and eosin; MB, microbubble; US, ultrasound; rt-PA, recombinant tissue plasminogen activator.

IVC vessel walls. The channels within the thrombi were found to allow recanalization, as indicated by the arrows, similar to previous studies^{175,176,177}, and the fibrin-rich region within the blood clot decreased in group A of sonothrombolysis.

4.4 DISCUSSION

This chapter was the first to evaluate the efficacy of sonothrombolysis using microfluidically produced microbubbles ($>15 \mu\text{m}$) in a murine model of DVT. Microbubbles from a microfluidic device were transiently stable, dissolved in the circulation system in minutes (Fig. 4.4). The use of microbubbles of large diameter in sonothrombolysis applications has previously been proven safe³². However, conditions (such as blood flow velocity) in the arteries and veins are not comparable. In addition to differences in arterial and venous thrombus, the age of the thrombus can also affect the therapeutic efficacy of a certain therapy. Catheter-directed intervention for DVT does not show clinical improvement over anticoagulant medications in early-stage DVT, but it is at increased risk of vein injury^{178,179,180,40}. An appropriate intervention time point for intravenous therapy should be selected for thrombolysis studies. Li *et al.* propose that patients with intermediate DVT may experience better clinical outcomes when treated with catheter-directed thrombolysis¹¹⁴. Therefore, our sonothrombolysis was performed on Day 3 post DVT formation.

Our mouse model of DVT was created by partial ligation of the IVC, leading to venous stenosis and hemodynamic instability. This model allows for DVT formation while preserving blood flow as observed in clinical DVTs, thereby enabling the delivery of thrombolytic drugs and microbubbles to blood clots. Therefore, it is a suitable animal model for thrombolysis studies. However, this model is associated with a large variance in thrombus size¹⁸¹. To mitigate differences in blood clot size, in this chapter, blood clots less than 5 mm^3 were excluded after pre-therapy ultrasound imaging, as in Fig. 4.3,

since smaller clots were generally easier to remove and low risk, even without interventions. In the *in vivo* experiments, the residual volume rate in rt-PA (group C) was not significantly different from the no-therapy control group D, which was consistent with the results of rats with acute carotid artery occlusion¹¹³. The thrombus volume in the no-therapy control group D decreased by approximately 50% over a period of 14 days, which aligns with the findings of previous studies^{182,183}. Furthermore, sonothrombolysis using large microbubbles (group A) displayed significantly improved therapeutic efficacy compared to other control groups in Fig. 4.6, matching results in the *in vitro* model and the arterial model^{32,31}.

The microfluidically produced microbubbles were of 18.0 μm diameter at a production rate of approximately 90×10^3 MBs/s. Large microbubbles have been shown to have stronger bioeffects in applications of blood brain barrier disruption⁹², stroke³², and DVT^{166,31}. A possible explanation for this phenomenon is the increased transfer of momentum induced by acoustic radiation force^{158,159}, and higher-energy cavitation events^{160,161}. The administration of microbubbles and thrombolytic agents was performed through a tail vein catheter. Therefore, the routes of intravenous administration should be chosen between a tail vein³² or femoral veins^{184,185}, as they were physically close to the location of the thrombus in the IVC. However, femoral vein injections presented technical difficulties and were not suitable for a study involving long-term survival of mice¹⁸⁶. Given the number of animals, I use the current scheme to evaluate our performance. Notably, in our experiments, the administration of microbubbles and rt-PA did not result in any mouse fatalities.

Ultrasound applied to cavitate the microbubbles was implemented by an Olympus

Panametrics transducer on the abdomen. Catheter-based ultrasound has also been investigated to enable human-compatible dimensions, such as a forward-looking transducer that generates vortex ultrasound^{187,188,165}, or a side-looking transducer^{116,189,156,190}. These therapeutic ultrasound designs can be combined with real-time control of the on-chip microbubbles generation¹⁷¹. Advances in the miniaturization of therapeutic ultrasound and microfluidic technology will provide effective therapies for thrombus-related conditions, in the field of catheter-directed therapy. This is an important step towards the miniaturization of human-compatible microfluidic devices for DVT therapy.

Shear wave elastography enhancement using Fourier feature network

5.1 INTRODUCTION

Biological tissues or organs with different levels of stiffness can serve as biomarkers of developing diseases¹⁹¹. Ultrasound (US) elastography is an imaging technique to estimate stiffness from soft tissue deformation developed by Ophir *et al.*¹⁴⁰. This non-invasive imaging technique enhances morphological contrast and identifies diseased tissue based on deviations from background or normal stiffness. Consequently, US elastography has become a common approach to screen and diagnose conditions such as deep vein thrombosis (DVT)^{52,192}, prostate cancer¹⁹³, breast cancer^{194,195}, thyroid cancer^{196,197} and liver disease^{198,199}.

Shear wave elastography (SWE) uses external vibrators or acoustic radiation forces (ARFs) to induce deformation of the soft tissue^{200,201,202,203,204}. Recent advances in co-

herent plane wave compounded (CPWC) imaging enable the tracking of shear wave propagation at a high frame rate after ARF pushes⁵⁴. Imaging schemes, such as comb-push ultrasound shear elastography (CUSE) invented by Song *et al.*, allow the characterization of the entire imaging field^{205,206,207}. The shear wave velocities can be extracted from 2D ultrasound image series to evaluate tissue stiffness. However, the stiffness estimated by SWE can be affected by respiratory/cardiac motion and vessel pulsation^{57,58,208}. Although a decrease in the number of acquisitions can alleviate the impact of motion on stiffness and lower ARF push energy, it may also be associated with a low signal-to-noise ratio (SNR) and an increase in time estimation errors in elastography^{209,210,211}. Exploring methods to increase SNR for noisy SWE displacement signals is essential for velocity estimation and stiffness reconstruction²¹².

Deep learning (DL) has been extensively researched in a variety of fields in the last decade, including computer vision^{213,214} and natural language processing^{215,216}. Recent progress in DL has started to have an impact on scientific computation and physical system modeling. It has been shown that a neural network trained to approximate the solution to ordinary differential equations (ODEs)/partial differential equations (PDEs) has the potential to replace traditional numerical methods, such as the finite difference method (FDM) and finite element method (FEM). Deep learning, in contrast to traditional methods, uses automatic differentiation (AD)²¹⁷ to derive derivatives, and ODEs/PDEs are regularization terms to be added to loss functions.

Raissi *et al.* founded a general physics-informed neural network (PINN) framework to solve the system with a limited dataset or even without training data^{61,60}. Since then, researchers have shown that PINN can be applied to various physical problems, such

as the Navier-Stokes equation^{60,62,63,64,65} and solid mechanics^{66,67,68,69}. PINNs are also extended to medical applications, including prediction of thrombus properties⁷⁰, blood flow modeling⁷¹, transcranial ultrasound propagation^{218,219}, and measurement of tissue properties²²⁰.

Significant advances in PINNs have also expanded their applications in learning the motion of biological tissues. Shear wave elastography is complex in biological tissue due to biological tissue's high incompressibility and high dimensions²²¹. In articles involved with biological tissue mechanics with PINNs, an energy-based hyper-elastic model has been proposed to analyze the response of loading^{222,223,224}. However, they do not include temporal motion estimation, which is essential for dynamic elastography. Recently, Thakur *et al.* has proposed using only the velocity field of a viscoelastic fluid to learn the pressure field and model parameters, motivating us to apply a similar strategy to tissue and its temporal displacement field²²⁵. Yin *et al.* has used a wave-equation-based SWENet for shear wave elastography with the introduction of a stream function, and the network can be trained to produce an elasticity mapping from the average of in-phase and quadrature (IQ) data in multiple acquisitions⁷³. However, recent researchers have pointed out that deep fully connected networks weaken PINNs' ability to learn high-frequency functions^{226,227,228}. The feature of over-smoothness can undermine the use of PINN for high-frequency ultrasound problems. For this limitation, a Fourier feature network (FFN) supported by neural tangent kernel (NTK) theory was proposed to handle multi-scale problems^{229,230}. Multi-scale random Fourier features can prevent biased learning along the dominant eigen-directions, and assist PINN to solve challenging problems such as wave propagation²³⁰.

Inspired by the FFN architecture, this research introduces an approach using both data-driven and physics-informed methods, termed Shear wave ELastography Fourier feature Network (SELFNet). SELFNet, described in Fig. 5.1, incorporates an auxiliary network to the original multi-scale spatial-temporal FFN to approximate shear modulus. SELFNet is designed to denoise and correct the displacement field from limited acquisitions in shear wave elastography, based on wave equations. It employs a simple form of scalar wave equations to uphold the physics laws during shear wave propagation, while preserving detailed temporal features through a Fourier representation of the input coordinates. In this chapter, the performance of SELFNet was evaluated using displacement data from phantom experiments and compared to a filtering method. Subsequently, an ablation study was conducted to validate the use of FFN to improve the reconstruction of shear wave elastography. Additionally, SELFNet was also tested in *ex vivo* tissues to test its robustness.

5.2 MATERIALS AND METHODS

In this section, the proposed SELFNet to solve shear wave propagation in elastography imaging is introduced.

5.2.1 BACKGROUND AND FRAMEWORK OF SELFNET

Following the original PINN framework⁶¹, I formulate a time-dependent PDE problem in a domain $\Omega \subset \mathbb{R}^d$ parameterized by λ with a spatial-temporal coordinate vector

$\mathbf{z} := [x_1, \dots, x_{d-1}; t]$ and its solution \mathbf{u} as the following format:

$$\mathcal{F}(\mathbf{u}(\mathbf{z}); \boldsymbol{\lambda}) = \mathbf{f}(\mathbf{z}), \mathbf{z} \in \Omega, \quad (5.1)$$

$$\mathcal{B}(\mathbf{u}(\mathbf{z})) = \mathbf{g}(\mathbf{z}), \mathbf{z} \in \partial\Omega, \quad (5.2)$$

where \mathcal{F} represents the nonlinear differential operator, \mathbf{f} describes the PDE problem, \mathcal{B} is the operator for initial or boundary conditions (BCs) on the boundary $\partial\Omega$ and \mathbf{g} is the boundary function.

A feed-forward neural network, also known as multi-layer perceptron (MLP), is one of the basic neural network architectures. It consists of an input layer, hidden layers and an output layer. For an L -layer neural network, the MLP is expressed as follows:

$$f_{\boldsymbol{\theta}}(\mathbf{x}) = \mathbf{W}^{[L]} \phi(\mathbf{W}^{[L-1]} \phi(\dots (\mathbf{W}^{[2]} \phi(\mathbf{W}^{[1]} \mathbf{x} + \mathbf{b}^{[1]}) + \mathbf{b}^{[2]}) \dots) + \mathbf{b}^{[L-1]}) + \mathbf{b}^{[L]}, \quad (5.3)$$

where $\mathbf{W}^{[i]}$ denotes the weights layer of the i -th layer, and $\mathbf{b}^{[i]}$ is the bias of the i -th layer, $\phi(\cdot)$ the non-linear activation function.

In PINN, the parameters of the neural network $\boldsymbol{\theta}$ are optimized by minimizing a loss function defined as the sum of the prediction error and the ℓ_2 norm of PDE and boundary condition residuals for collocation points and boundary points, respectively. The total loss ℓ is defined as below:

$$\ell = W_u \|\hat{\mathbf{u}}(\mathbf{z}) - \mathbf{u}\|^2 + W_f \|\mathcal{F}(\hat{\mathbf{u}}(\mathbf{z})) - \mathbf{f}(\mathbf{z})\|^2 + W_b \|\mathcal{B}(\hat{\mathbf{u}}(\mathbf{z})) - \mathbf{g}(\mathbf{z})\|^2, \quad (5.4)$$

$$\ell = W_u \ell_u + W_f \ell_f + W_b \ell_b, \quad (5.5)$$

where W_u , W_f and W_b are the weights for each term in the loss function, \hat{u} represent the neural network estimated solution to the PDE problem, $\|\cdot\|^2$ is the mean squared error. Optimization of neural network parameters θ is often performed using gradient descent, Adam and L-BFGS optimizers^{231,232}.

The difference between FFN and PINN is the introduction of the Fourier feature mapping module²³⁰. The input to a spatial-temporal FFN is to encode the input spatial and temporal coordinates using a random Fourier feature mapping followed by a conventional MLP θ_1 . The original input to a spatial-temporal problem is $z = [\mathbf{x}; t] = [x_1, \dots, x_{d-1}; t]$, after a random Fourier mapping γ , the input to the L -layer MLP θ_1 becomes

$$\gamma_{\mathbf{x}}^{(i)}(\mathbf{x}) = \begin{bmatrix} \cos(2\pi \mathbf{B}_{\mathbf{x}}^i \mathbf{x}) \\ \sin(2\pi \mathbf{B}_{\mathbf{x}}^i \mathbf{x}) \end{bmatrix}, \text{ for } i = 1, 2, \dots, M_x, \quad (5.6)$$

$$\gamma_t^{(j)}(t) = \begin{bmatrix} \cos(2\pi \mathbf{B}_t^j t) \\ \sin(2\pi \mathbf{B}_t^j t) \end{bmatrix}, \text{ for } j = 1, 2, \dots, M_t, \quad (5.7)$$

where the coefficients $\mathbf{B}_{\mathbf{x}}^i$ and \mathbf{B}_t^j are not trainable. The spatial and temporal coordinates are mapped and fed into a L -layer MLP θ , resulting in intermediate vectors

$$\mathbf{H}_{\mathbf{x}}^{(i)} = f_{\theta}(\gamma_{\mathbf{x}}^{(i)}(\mathbf{x})), \text{ for } i = 1, 2, \dots, M_x, \quad (5.8)$$

$$\mathbf{H}_t^{(j)} = f_{\theta}(\gamma_t^{(j)}(t)), \text{ for } j = 1, 2, \dots, M_t. \quad (5.9)$$

According to the original FFN, these outputs are then point-wise multiplied and con-

catenated to create a merged variable,

$$\mathbf{H}^{(i,j)} = \mathbf{H}_x^{(i)} \odot \mathbf{H}_t^{(j)} \text{ for } i = 1, 2, \dots, M_x \text{ and } j = 1, 2, \dots, M_t, \quad (5.10)$$

which is fully connected to the final output of FFN,

$$\hat{\mathbf{u}}_{\theta}(\mathbf{z}) = \mathbf{W}^{[L+1]}[\mathbf{H}^{(1,1)}, \dots, \mathbf{H}^{(M_x, M_t)}] + \mathbf{b}^{[L+1]}. \quad (5.11)$$

In ultrasound imaging, only the z-component of displacement w can be calculated from the correlation algorithms. The scalar wave equations can be written as²³³

$$\nabla \cdot (\mu \nabla w) - \rho \frac{\partial^2 w}{\partial t^2} = 0, \quad (5.12)$$

where ρ is the density of tissue, μ is the shear modulus and ∇ is the nabla operator. In our study, the density is a constant of 1000 kg/m³. To customize FFN's application to a 2D shear wave elastography problem, I build a SELFNet composing of two sub-networks, one FFN θ_1 and one auxiliary MLP θ_2 . The FFN θ_1 takes spatial and temporal coordinates as inputs and approximates $\hat{\mathbf{w}}_{\theta_1}(x, z; t) = [\hat{w}, \hat{w}_x, \hat{w}_z, \hat{w}_t]$, where \hat{w}_{\square} is the network-predicted derivative of axial particle displacement with respect to a variable. The MLP θ_2 estimates the shear modulus field $\hat{\mu}_{\theta_2}(x, z)$ during training. The auxiliary network receives only the spatial coordinates x, z as input because the shear modulus remains constant over time.

Since only the second-order derivatives along the x and z axes can be calculated in 2D ultrasound imaging, it is assumed that the derivatives related to the y-axis are negligible.

The physics-informed loss ℓ_f for equation 5.5 should be

$$\ell_f = \left\| \frac{\partial}{\partial x}(\hat{\mu}\hat{w}_x) + \frac{\partial}{\partial z}(\hat{\mu}\hat{w}_z) - \rho \frac{\partial}{\partial t}\hat{w}_t \right\|^2. \quad (5.13)$$

The data-driven loss ℓ_u is the mean square error to the input training displacement data

$$\ell_u = \|\hat{w} - w^{train}\|^2 + W_{dif}(\|\hat{w}_t - w_t^{train}\|^2 + \|\hat{w}_z - w_z^{train}\|^2 + \|\hat{w}_x - w_x^{train}\|^2), \quad (5.14)$$

where w_t^{train} , w_z^{train} and w_x^{train} are the derivatives of training displacement signals w^{train} using the central differential scheme. The parameter W_{dif} regulates the differential component to approximate the magnitude of the original component.

The network architecture of SELFNet is illustrated in Table 5.1 and in Fig. 5.1. The size of a MLP is defined as the number of hidden layers \times the number of hidden neurons per layer. Both sub-networks used tanh as the activation function⁶⁰. I applied one Fourier feature mapping initialized with $\sigma_x = 1$ to spatial coordinates $[x, z]$ and two Fourier feature mappings initialized by $\sigma_t = 1, 10$ to temporal coordinate t , consistent with²³⁰. Two Fourier feature mappings were designed to preserve temporal details in the displacement data and provide a sparse feature map, thereby avoiding over-smoothing. All featurized spatial and temporal inputs were fed into a 80×7 MLP. After point-wise multiplication of the spatial and temporal outputs of the MLP, the outputs were concatenated and converted to participle displacement \hat{w} and its derivatives $\hat{w}_t, \hat{w}_x, \hat{w}_z$ through an additional fully connected layer. An auxiliary network θ_2 of 60×6 hidden neurons was trained to predict the shear modulus simultaneously during training. The auxiliary network constrained the shear modulus output between 1 and 33.3 kPa using a

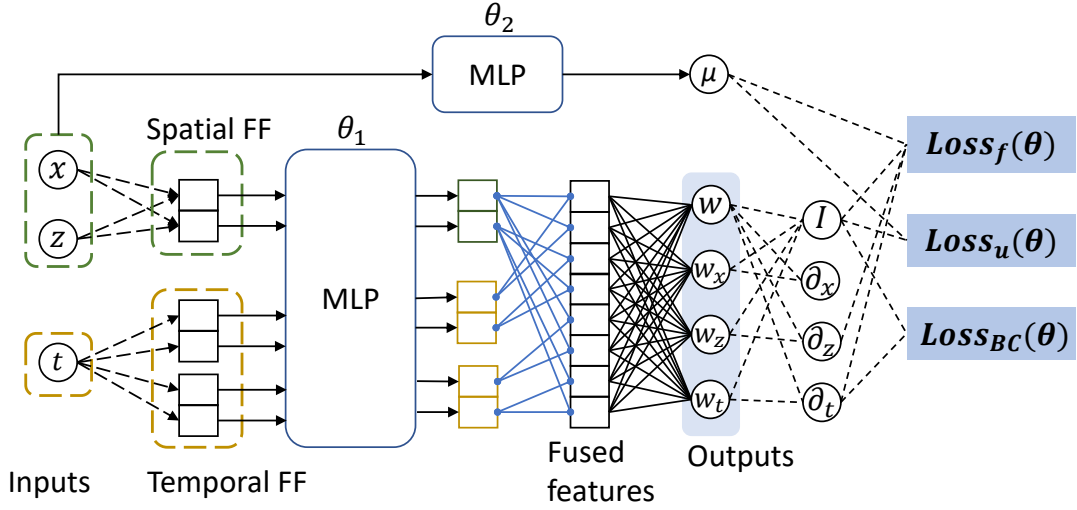


Figure 5.1: SELFNet architecture: the input spatial and temporal coordinates $[x, z; t]$ are encoded using Fourier feature embeddings (initialized with different σ) separately, and then the spatial and temporal featurized tensors go through a neural network θ_1 . Point-wise multiplication is applied to the spatial and temporal outputs, and the results are concatenated. The final particle displacement and related field are obtained through an additional linear layer. An auxiliary network θ_2 predicts the shear modulus by providing the spatial coordinates. The whole networks θ_1 and θ_2 are optimized by summation of data-driven loss ℓ_u and physics-informed residual loss ℓ_f , boundary condition loss ℓ_b . MLP: multilayer perceptron; FF: Fourier features.

sigmoid function²³⁴. For comparison, the performance of an 80×8 MLP and an 80×8 PINN containing the same auxiliary network was tested for ablation study purposes. The number of parameters was approximately consistent in SELFNet and PINN.

5.2.2 TRAINING OF SELFNET

To train SELFNets for each dataset, 40,000 source points from axial particle displacement fields, 25,000 collocation points, 200 points for the initial zero displacement and velocity conditions were used in ℓ_u , ℓ_f and ℓ_b , respectively. The sampling of datapoints was updated each epoch. The weight ratio was $W_u : W_{dif} : W_f : W_b = 1 : 0.001 : 0.0001 : 1$. Each dataset was trained using SELFNet for 80,000 epochs, with the train-

Table 5.1: SELFNet architecture. FFN: Fourier feature network; MLP: Multilayer perceptron.

Name	Layer	Input size	Output size	Output variable
FFN θ_1	Fourier feature mapping 1	2	80	γ_x^1
		1	80	γ_t^1
		1	80	γ_t^2
	Fully connected 1_1-1_7	80	80	$\mathbf{H}_x^{(1)}, \mathbf{H}_t^{(1)}, \mathbf{H}_t^{(2)}$
	Pointwise multiplication 1	2×80	80	$\mathbf{H}^{(1,1)}$
2×80		80	$\mathbf{H}^{(1,2)}$	
Concatenation 1	2×80	160	\mathbf{H}	
Fully connected 1_8	160	4	\mathbf{w}	
MLP θ_2	Fully connected 2_1	2	80	
	Fully connected 2_2-2_5	60	60	
	Fully connected 2_6	60	1	μ

ing epochs for PINNs and MLPs being equivalent. I used an Adam optimizer to search for optimal neural network parameters at an initial learning rate of 0.001. The learning rate decayed by a factor of 0.9 every 2,000 epochs.

In this chapter, all experiments are implemented in PyTorch 1.13.1. The computing platform for this study was a workstation equipped with four NVIDIA RTX A4000 graphics processing units (GPUs).

5.2.3 DATA ACQUISITION

The data processing workflow is illustrated in Fig. 5.2. A Verasonics Vantage 256 system (Verasonics, Kirkland, WA, USA) equipped with a L7-4 transducer was used to collect SWE data. A custom 75-angle plane wave (PW) imaging sequence was programmed to image a CIRS ultrasound phantom (CIRS-049, Norfolk, VA, USA)^{235,236}. The ARF push from the 32 central elements lasted for 192 μs at a setting voltage of 50 V. Five hundred microseconds following the ARF push, the PW imaging sequence for

the phantom started to image at a center frequency of 5.2 MHz and a pulse repetition frequency (PRF) of 10 kHz, and the imaging depth was limited to 47 mm. The pushes were repeated 75 times for different tilted PW imaging angles, evenly ranging from -15° to 15° with a step size of 0.405° . A ground-truth (GT) dataset was built using all 75 angles for CPWC, followed by a spatial Gaussian filter with a standard deviation of 0.15 mm along the x and z directions²³⁷, while a training dataset used 5 tilted PW imaging angles in $[-4^\circ, 2^\circ, 0^\circ, 2^\circ, 4^\circ]$ for compounding. The axial displacements for each frame were extracted using the Loupas autocorrelation algorithm on the IQ data and normalized by the maximum absolute axial displacement of the whole dataset $|w_{\max}|$ ²³⁸. The half-space from the ARF push center to the right edge was used for training, and the propagation direction of the shear wave was from left to right in the context. The final dimension of the region of interest (ROI) in the displacement field was $80 \times 160 \times 48$ (lateral \times axial \times temporal), where the corresponding resolution in wavelength λ and ms is $0.5\lambda \times 0.25\lambda \times 0.1$ ms.

5.2.4 PHANTOM AND EX VIVO TISSUES

The CIRS phantom contained four types of circular lesions of various stiffness. Young's moduli in the lesions were 6.6 (type I), 11 (type II), 34 (type III), and 73 (type VI) compared to the background value of 23 kPa. Four lesions of each stiffness with diameters ranging from 2.5 to 10 mm were imaged using the SWE sequence. In total, 16 particle displacement datasets were collected in this chapter.

A piece of porcine liver was purchased from a local grocery and processed as²¹¹. During imaging, the sample was placed within a water bath, and the transducer was

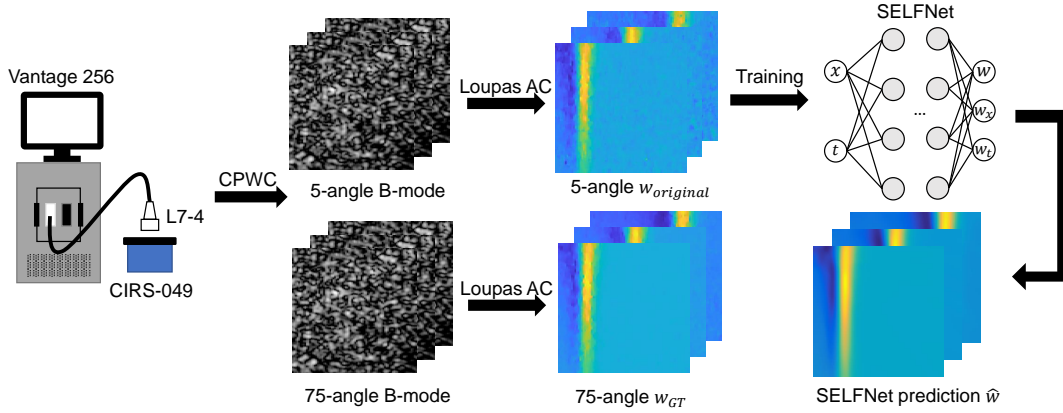


Figure 5.2: Workflow for data acquisition and processing. A Verasonics Vantage 256 equipped with a L7-4 transducer was used to collect data on CIRS-049 phantom. The displacement data $w_{original}$ or w_{GT} were extracted from either 5- or 75-angle CPWC images using Loupas autocorrelator, respectively. The displacement data $w_{original}$ from 5-angle CPWC images were fed into a SELFNet to predict the corrected displacement field \hat{w} . AC: autocorrelator; CPWC: coherent plane wave compounding; GT: ground truth.

placed on the top of the sample. The imaging parameters remained the same as those for the phantom imaging, except the imaging duration was 12 ms. In contrast to the phantom experiment, three training datasets for SELFNet were obtained from compounded data using 5 angles at $[-4^\circ, 2^\circ, 0^\circ, 2^\circ, 4^\circ]$, 3 angles at $[2^\circ, 0^\circ, 2^\circ]$ and non-compounded 0° IQ data.

5.2.5 RECONSTRUCTION

A reconstruction of the elasticity map was implemented based on a cross-correlation method developed by Song *et al.*²³⁹. The shear wave velocities along the x and z directions in a pixel were calculated from a window of $6 \times 6 \lambda^2$ around the center pixel. The

local shear wave velocity v_s was then converted to Young's modulus by

$$E = 3\mu = 3\rho v_s^2, \quad (5.15)$$

where v_s the group speed of shear wave in propagation media, μ the shear modulus of media and ρ the density of media. The range of Young's modulus was limited to 100 kPa²³⁴.

5.2.6 QUANTIFICATION METRICS

Our proposed method is compared with original displacement data, Gaussian filtered data, PINN outputs and MLP outputs. The results of each method were evaluated using the metrics listed below.

1. Relative ℓ_2 error. The displacement fields from each method were individually compared with the ground truth displacement w_{GT} , in terms of relative ℓ_2 error^{69,219},

$$\mathcal{E}(w) = \frac{\sqrt{\sum_{i=1}^N \|w_{GT}^{(i)} - w^{(i)}\|^2}}{\sqrt{\sum_{i=1}^N \|w_{GT}^{(i)}\|^2}}, \quad (5.16)$$

where N is the total number of data points and $w_{GT}^{(i)}$ is the i -th particle displacement derived from the filtered 75-angle CPWC images.

2. Improved SNR²¹¹. The improvement over the unprocessed data $w_{original}$ was assessed by

$$\text{SNR}_{imp}(w) = \frac{1}{N} \sum_{i=1}^N 10 \log_{10} \frac{\|w^{(i)} - w_{GT}^{(i)}\|^2}{\|w_{original}^{(i)} - w_{GT}^{(i)}\|^2}. \quad (5.17)$$

3. Root mean square error (RMSE). The downstream reconstruction elasticity maps were calculated and compared with the ground truth E_{GT} in kPa,

$$\text{RMSE}(E) = \sqrt{\frac{1}{N} \sum_{i=1}^N \|E_{GT}^{(i)} - E^{(i)}\|^2}. \quad (5.18)$$

4. Structural similarity (SSIM) index. Reconstruction elasticity maps from the proposed or other methods were used to calculate with the reference E_{GT} , defined as

$$\text{SSIM}(E) = \frac{(2\bar{E}_{GT}\bar{E} + c_1)(2\sigma_{cov} + c_2)}{(\bar{E}_{GT}^2 + \bar{E}^2 + c_1)(\sigma_{GT}^2 + \sigma^2 + c_2)}, \quad (5.19)$$

where \bar{E} and σ^2 represent the mean and variance of the reconstructed elasticity, respectively, σ_{cov} is the covariance between the ground truth and the reconstructed method, c_1 and c_2 are constants to prevent denominator equal to zero in the division.

5.3 RESULTS

5.3.1 DENOISING DISPLACEMENT FIELD

Snapshots of the displacement field in the phantom of a type III lesion at 1, 2, and 3 ms after ARF push are demonstrated in Fig. 5.3. The original displacement signals $w_{original}$ contained noise, particularly in the deep (second row in Fig. 5.3). A Gaussian filter blurred and averaged the neighboring pixels, thereby enhancing the wavefront. In contrast, SELFNet output filtered out background noise by minimizing physics residuals, while it also learned the details of the wavefront. The relative ℓ_2 errors for this

dataset were 0.227, 0.132 and 0.115 from the original, Gaussian-filtered and SELFNet-denoised data, respectively.

The red dotted particle displacement data w in Fig. 5.3 are shown in Fig. 5.4. The original 5-angle CPWC displacement signal over time at the location was noisy and presented a large oscillation, while the ground truth data were smooth. The relative ℓ_2 error for the original input was 0.413. A Gaussian filter was unable to completely eliminate the oscillation due to the low SNR of the original signal. The relative ℓ_2 error was reduced to 0.223, resulting in an improved SNR_{imp} of 3.8 dB. SELFNet successfully removed the noise of the displacement \hat{w}_{θ_1} at this point. The relative ℓ_2 error was 0.159, with the SNR_{imp} reaching 10.8 dB in this example. SELFNet can infer displacement at any given coordinate and it estimated displacement from 0 to 5.2 ms at a temporal resolution of 0.02 ms in this example.

5.3.2 RECONSTRUCTION RESULTS

The downstream elasticity mappings of phantoms of type II and type VI lesions using the correlation method are illustrated in Figs. 5.5 and 5.6.

In Fig. 5.5, reconstruction artifacts were observed on the left boundary and on the right side of the soft lesion. The reconstruction of the original displacement signals was noisy in the upper region of the background. The other reconstruction offered a smoother estimate. In this type II lesion example, SELFNet achieved the highest performance, with RMSE and SSIM values of 1.78 kPa and 0.977, respectively, compared to the ground truth reconstruction.

In Fig. 5.6, a hard type VI lesion, which is more common in breast cancer or liver

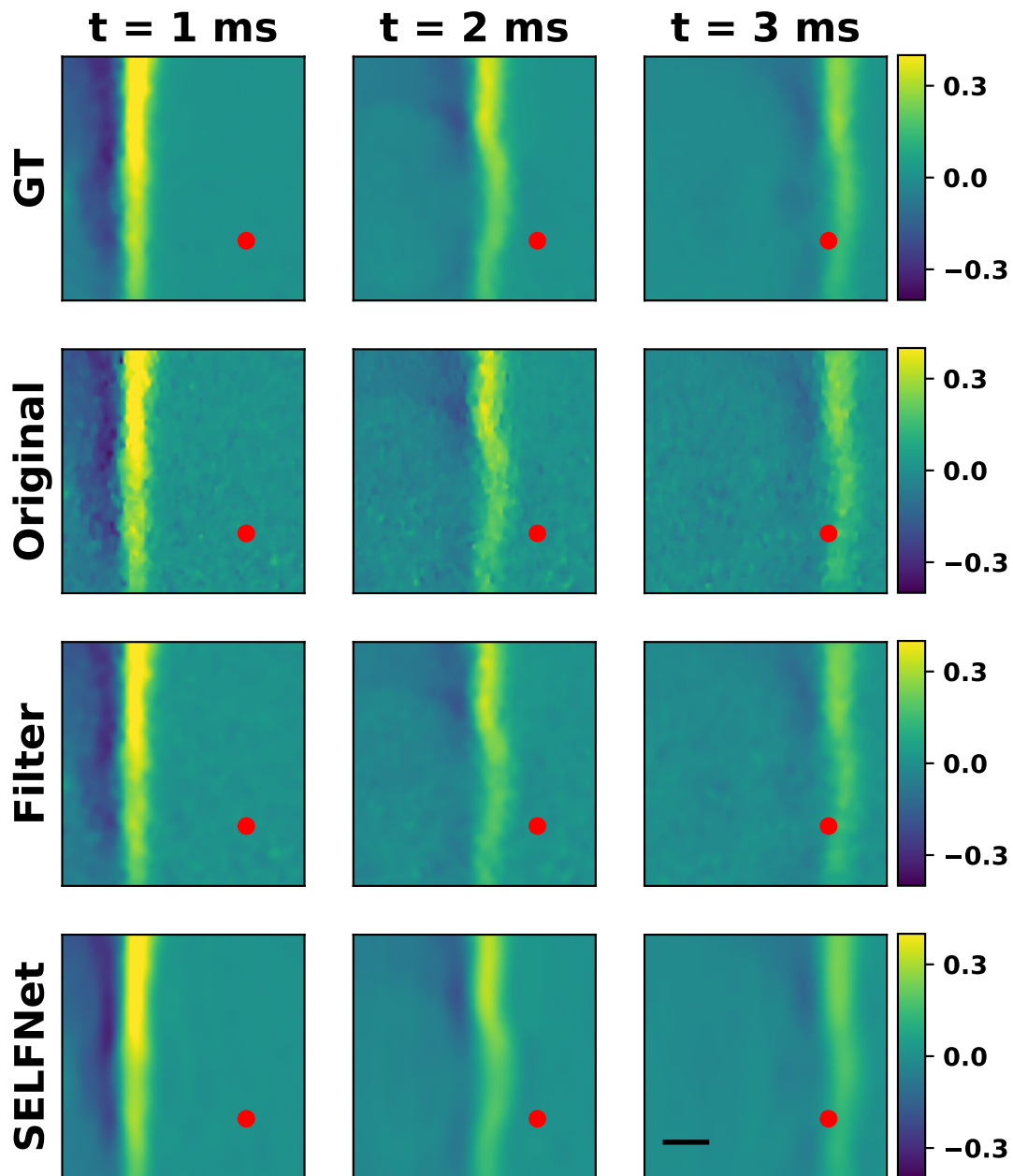


Figure 5.3: Snapshots of normalized displacement field at 1, 2 and 3 ms, in a phantom of a type III lesion. Each row represents the ground-truth, original, Gaussian-filtered or SELFNet-predicted displacement signals. The red dot indicates the location of the point in Figure 4. The scale bar represents 2 mm. GT: ground-truth.

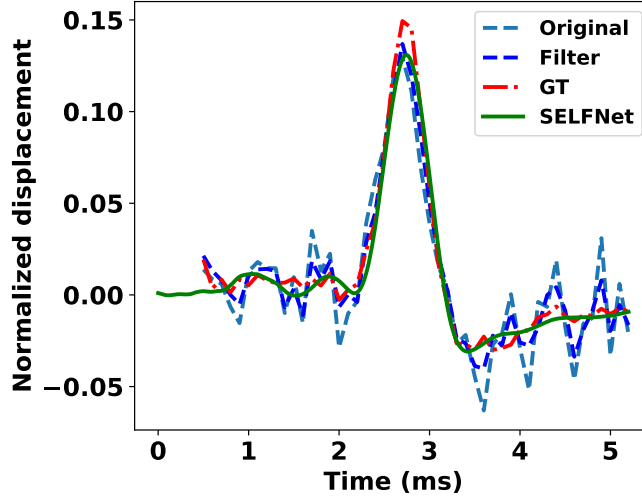


Figure 5.4: Axial displacement at $x = 8.8, z = 31$ mm from 0 to 5.2 ms. The original data are Gaussian filtered or trained using SELFNet. In comparisons with the ground truth, the relative ℓ_2 errors for the original, Gaussian-filtered, and SELFNet predicted displacement are 0.413, 0.223 and 0.159, respectively. The improved SNRs over the original data are 3.8 and 10.8 dB using a Gaussian filter and SELFNet approaches.

disease, was reconstructed using each displacement signal^{240,241}. In the elasticity map from the original signal, insufficient angles for compounding resulted in saturation of Young's modulus within the lesion, stemming from an inaccurate estimation of shear wave velocity. Both the PINN and MLP techniques improved the smoothness of the displacement field and the reconstruction outcomes. However, this increased smoothness led to the formation of a striped pattern extending from the top-left to the bottom-right corner. The SELFNet reconstruction closely matched the reference, achieving a RMSE of 2.04 kPa and an SSIM of 0.922, thus outperforming the performance of alternative methods. Among the other methods, MLP obtained the minimum RMSE of 2.48 kPa, and PINN reached the maximum SSIM of 0.893.

Fig. 5.7 displays the output of the auxiliary network for both type I and type VI

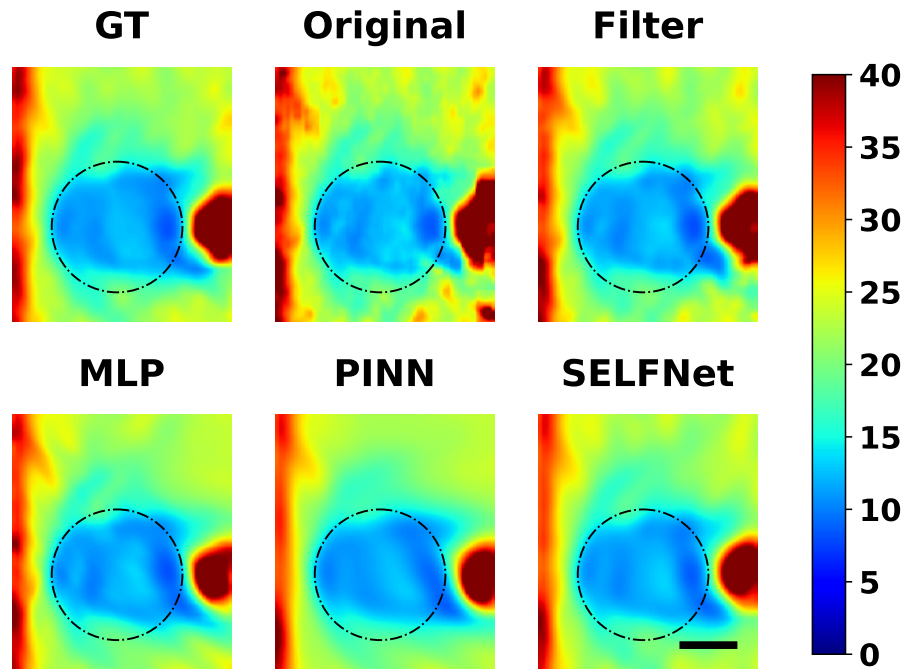


Figure 5.5: Reconstruction of elasticity mappings, where a type II lesion is included. The dash-dotted circle represents the location of the lesion. A 2 mm scale bar is plotted. Filter: Gaussian filter; MLP: multilayer perceptron; PINN: physics-informed neural network.

lesions. The SELFNet and PINN approaches demonstrated the capability to restore elasticity without further processing. They eliminated artifacts on the left boundary and corrected for the error (Fig. 5.7a) that occurred as the wavefront entered the background from the soft lesion. Notably, strip patterns were observed in the PINN’s auxiliary network output in Fig. 5.7b.

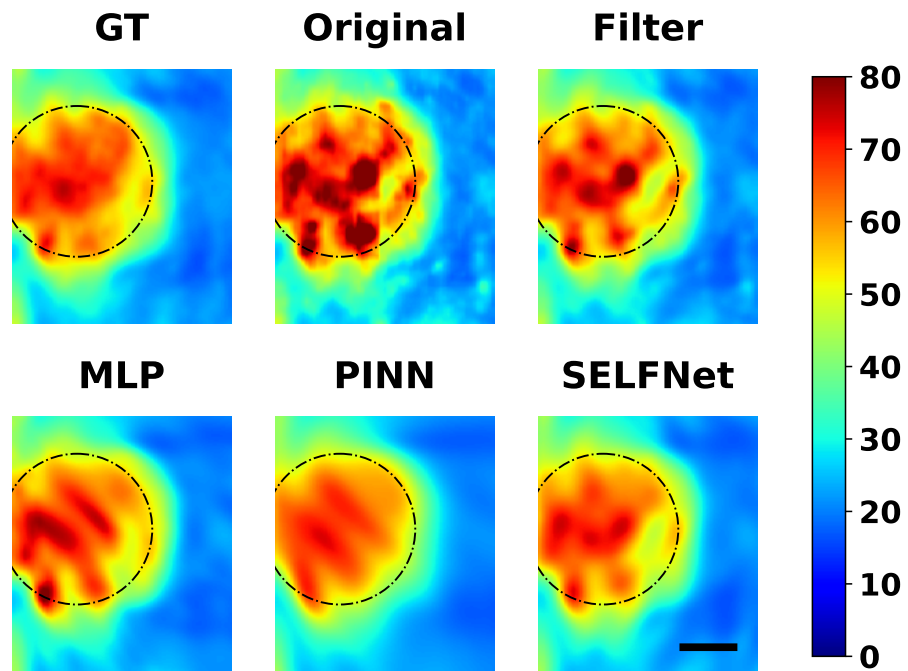


Figure 5.6: Reconstruction of elasticity mappings, where a type VI lesion is included. The dash-dotted circle represents the location of the lesion. A 2 mm scale bar is plotted. Filter: Gaussian filter; MLP: multilayer perceptron; PINN: physics-informed neural network.

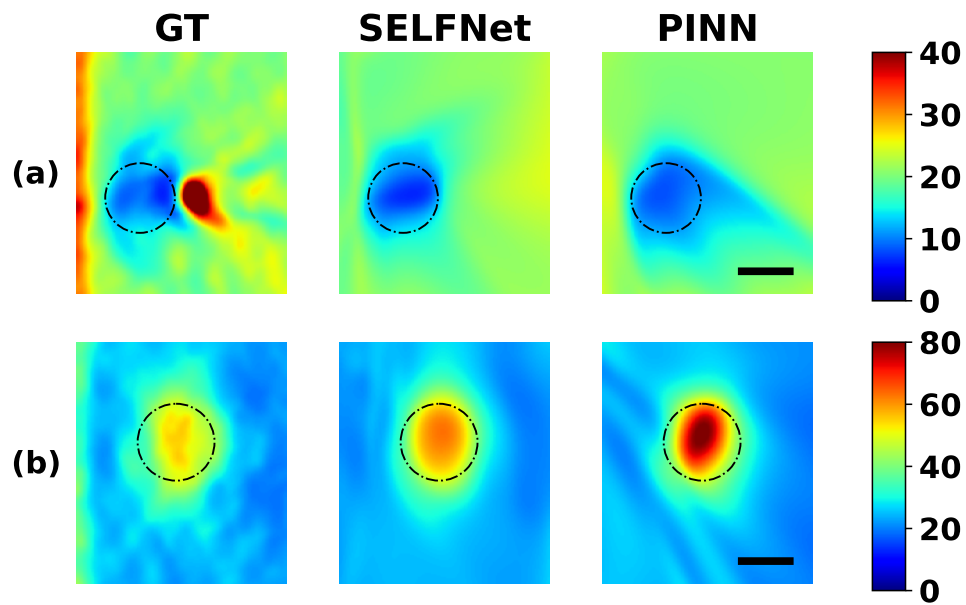


Figure 5.7: The auxiliary network θ_2 generates an approximate elasticity mapping. Displayed are the reconstructed fields of Young's modulus in phantoms with (a) Type I and (b) Type VI lesions. The image from left to right shows the reference, the SELFNet results, and the PINN results. A 2 mm scale bar is included and the dash-dotted line is the boundary of the lesion.

5.3.3 ABLATION STUDY

The summary of quantitative comparisons is listed in Table 5.2 and a detailed boxplot for each metric is plotted in Fig. 5.8. In conclusion, methods based on neural networks outperform traditional filtering techniques. Our SELFNet model documented a relative ℓ_2 error of 0.144, marginally higher than the PINN method 0.140, ranked second among all methods tested. This metric exceeded the original data and Gaussian-filtered data by 51% and 16%, respectively. Additionally, it yielded the lowest RMSE and highest SSIM for elasticity mappings compared to the reference, recording 1.76 kPa and 0.949, respectively. These values improved the unprocessed control by 69% and 0.093, and outperformed the filtering method by 45% and 0.04, respectively.

The minimal relative ℓ_2 error, along with the RMSE and SSIM scores in the downstream reconstruction results, suggested overfitting in the PINN model, as well as in the MLP model. Compared to the MLP and PINN models, the incorporation of Fourier feature mappings served as a critical module that contributed to improved performance. SELFNet outperformed PINN by 20.4% and 0.025 in the RMSE and SSIM of downstream reconstruction, respectively. A sparse representation of the input data alleviated overfitting to the training displacement field, indicating a superior learning ability of high-frequency information in shear wave elastography^{242,230}.

5.3.4 EX VIVO TISSUE RESULTS

The *ex vivo* tissue of the porcine liver exhibits a viscoelasticity property, suggested by the increasing width of the arrival wave in Fig. 5.9. The following Fig. 5.10a shows the reconstruction of Young's modulus using the correlation method. The correlation-based

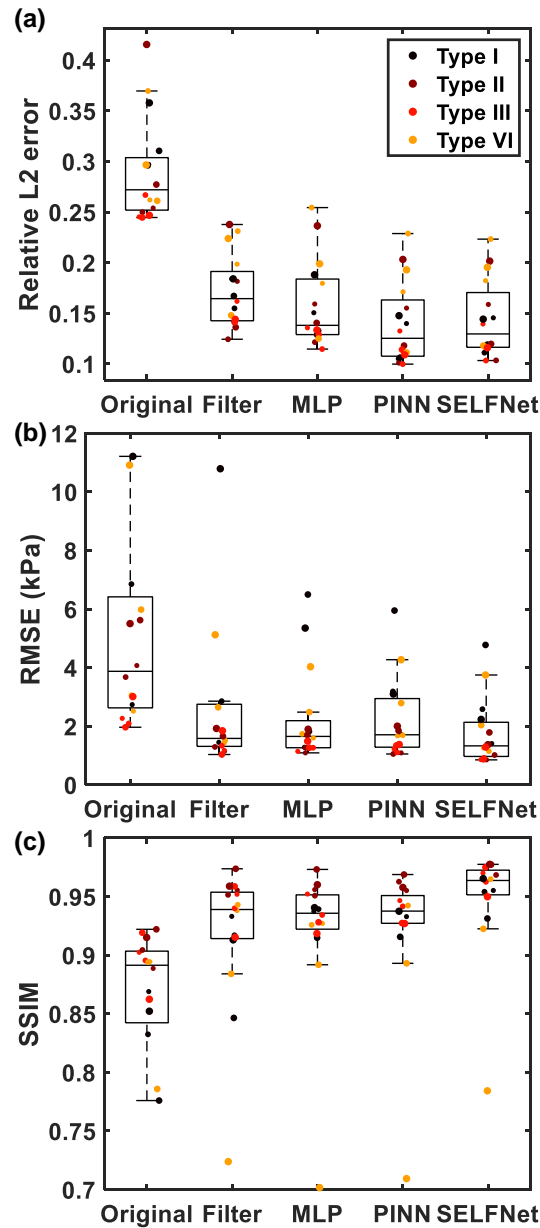


Figure 5.8: Overview of (a) Relative ℓ_2 error, (b) RMSE, and (c) SSIM metrics for qualitative assessment. The box-plots display original data and data processed by a Gaussian filter, MLP, PINN, and SELFNet. The scatter points' color and size reflect the lesions' stiffness and diameter, respectively. SELFNet provides the second least relative ℓ_2 error and the most accurate reconstruction based on RMSE and SSIM metrics. Outliers are not shown for relative ℓ_2 error above 0.45, RMSE above 12 kPa and SSIM below 0.7.

Table 5.2: Quantification summary of phantom data. The unit for RMSE is kPa. $N = 16$. MLP: Multilayer perceptron; PINN: physics-informed neural network; SELFNet: our proposed method; RMSE: root-mean-square error; SSIM: Structural Similarity index.

Metrics		Original	Gaussian Filter	MLP	PINN	SELFNet
$\mathcal{E}(w)$	mean	0.291	0.172	0.158	0.140	0.144
	std	0.051	0.035	0.042	0.040	0.038
RMSE	mean	5.72	3.20	2.24	2.21	1.76
	std	4.77	3.77	1.62	1.35	1.12
SSIM	mean	0.856	0.919	0.922	0.924	0.949
	std	0.086	0.061	0.062	0.060	0.047

reconstruction failed to estimate the elasticity in the deep region due to attenuation. Therefore, a relatively clear ROI of $4 \times 8 \text{mm}^2$ in Fig. 5.10a was selected for measurement purposes.

In the full datasets, the relative ℓ_2 errors using SELFNet in 5-, 3-angle CPWC and non-compounded data were 0.106, 0.123 and 0.194, respectively. For reference, the Gaussian-filtered and original displacement of 5-angle CPWC data were 0.146 and 0.184, respectively. Within the ROI, the RMSE for SELFNet-denoised displacement of 5-angle CPWC data was 0.41 kPa, while RMSE from 3-angle compounded and non-compounded dataset were 0.60 and 1.1 kPa, respectively. The SSIM indexes for SELFNet reconstructions were over 0.92 in all three cases. The findings of the *ex vivo* study indicate that SELFNet is effective for viscoelastic tissues with adequate SNR, such as in 5-angle and 3-angle CPWC B-mode images. However, in more extreme scenarios like non-compounded ultrasound data, obtaining a clean displacement field remains a challenge.

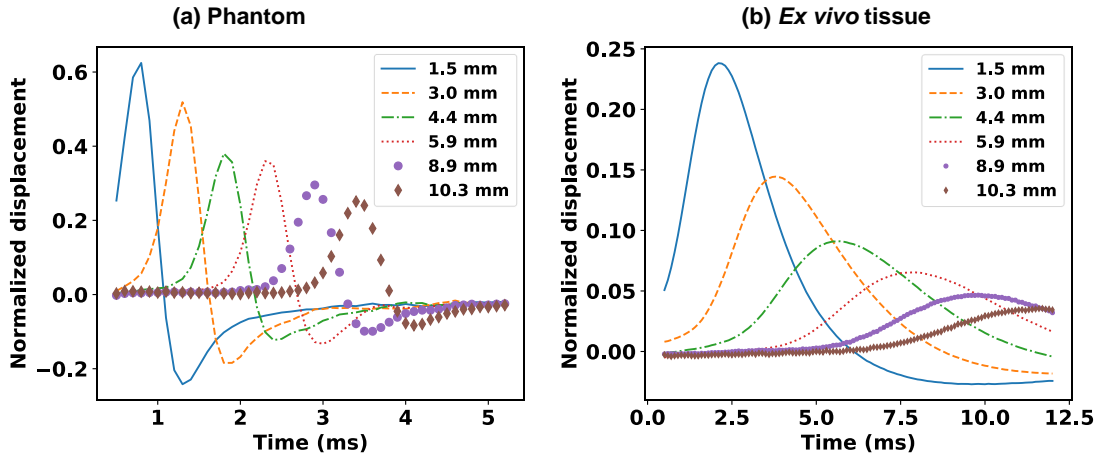


Figure 5.9: The ground-truth axial displacement signals w at various lateral positions and $z = 23$ mm in (a) phantom and (b) *ex vivo* tissue. The width of wavefront in *ex vivo* tissue increases along the shear wave propagation direction.

5.4 DISCUSSIONS

In this chapter, SELFNet is presented for shear wave elastography to denoise particle displacement and to enhance the reconstruction of elasticity in biological tissue. To the best of our knowledge, it is the first application combining the neural tangent kernel and PINN for shear wave elastography. Training data were prepared with a limited number of acquisitions, which were of clinical relevance to avoid long-time pressure exposure and motion artifacts despite increasing noise levels. During performance evaluation, SELFNet’s effectiveness was compared with conventional filtering technique and comparable neural network-based methods. The innovative neural network-based methodology exhibited the capacity to smooth authentic datasets containing noise, as evidenced in Figs. 5.3 and 5.4. Moreover, exploiting the sparse representation of input data through Fourier feature mappings improved the downstream reconstruction, surpassing PINN and MLP (Figs. 5.5 to 5.8). Additionally, I also applied it in a viscoelastic *ex vivo* tissue

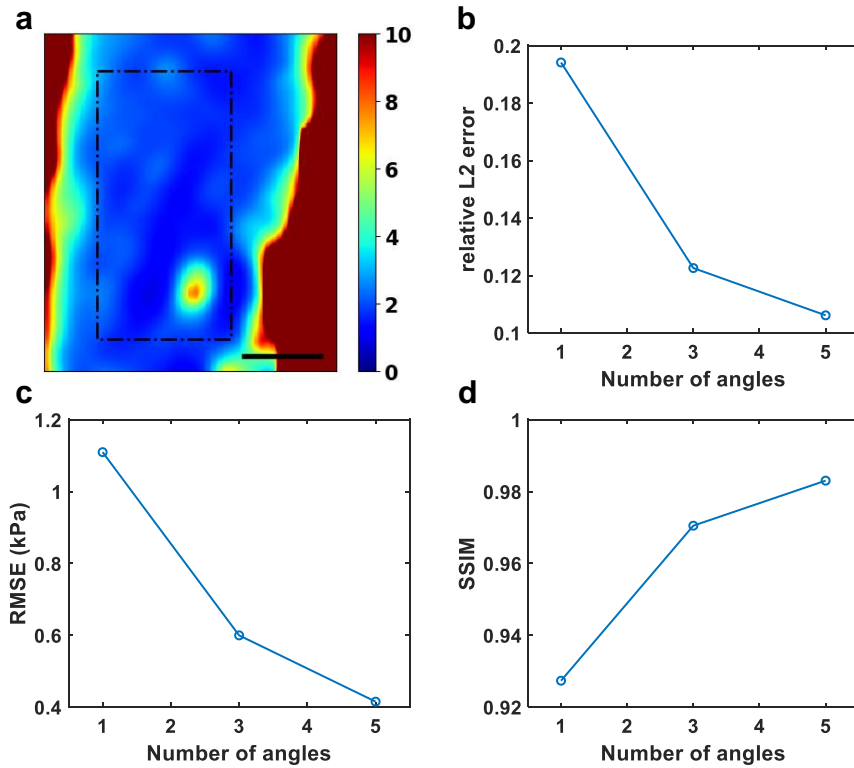


Figure 5.10: *Ex vivo* reconstruction results using SELFNet. (a) The ground truth reconstruction of Young's modulus in a homogeneous sample. Due to the attenuation and dispersion of the shear wave, reconstruction in the bottom-right area is not reliable. The dash-dotted rectangle of 4×8 mm² indicates the ROI used for RMSE and SSIM calculation. (b) Relative ℓ_2 error v.s. the number of acquired angles. (c) RMSE v.s. the number of acquired angles. (d) SSIM v.s. the number of acquired angles.

dataset. The low bias value in Young’s modulus of homogeneous tissue confirmed its robustness in viscoelastic tissue.

The denoising in displacement data is an important intermediate step for the final reconstruction of stiffness. Traditional filtering can reduce spikes in displacement signals, but noise or artifacts due to attenuation in the deep region are inevitable (Fig. 5.4), with fewer angles for compounding²⁴³. In this chapter a minimal problem of the half 2D space is considered. The implementation of SELFNet can be extended to the entire space or sequence with multiple ARF pushes, such as CUSE, since the wave equations remain applicable in these scenarios^{205,207}.

Furthermore, to generate results where the mesh point is not defined, the FEM must use the interpolation method, which adds extra inference time. Conversely, PINN can predict the physics fields at any given input coordinate with the same computational time as for the known inputs. Therefore, neural network-based methods, which are driven by the idea of meshless input and output, have also been reported to achieve super-resolution in a physics system with limited data^{244,245}. SELFNet or PINN-based methods can estimate fields at subpixels or at subframe resolutions, as shown in Fig. 5.4.

In our work, MLP θ_1 also learned the first derivative of particle displacement \hat{w} with respect to x , z and t . Instead of using AD twice to calculate the second derivative, I chose to differentiate the predicted \hat{w}_t , \hat{w}_x and \hat{w}_z to accelerate the training process, as suggested by Rao *et al.*⁶⁹.

The elasticity predicted from SELFNet’s auxiliary network shows the potential to remove artifacts in traditional reconstruction algorithms, as evidenced in Fig. 5.7a²⁴³. SWENet, developed by Yin *et al.*, has used a similar strategy of a subnetwork to suc-

cessfully estimate the shear modulus⁷³. Therefore, exploring reconstruction from neural networks based on physical models could be a future research direction. Two outliers of SELFNet are identified in Figs. 5.8b and 5.8c. These outliers correspond to the phantom of large type I and type VI lesions. The reconstructions of Young's modulus for these two outliers are shown in Fig. 5.11. Removing outliers results in a 20% improvement in RMSE for SELFNet, reducing it to 1.40 kPa. Similarly, the removal of outliers increases SSIM by 0.013 and relative ℓ_2 error by 0.002, respectively. Notably, the reconstructions from the SELFNet-denoised data outperform other methods in terms of RMSE and SSIM. The significant differences between these outliers and other datasets are associated with the geometry of the lesions and reconstruction artifacts.

An alternative to improve the reconstruction results can be to use ARF pushes from two sides of the region of interest²⁴⁶. The average data from two side pushes can mitigate the reconstruction error using the correlation-based method when the shear waves cross the boundary of two media, but the implementation of the multiple push sequence is not the focus of this work. Additionally, SELFNet can be applied for the displacement data for each of the two pushes separately.

The displacement fields from each acquisition need to be re-trained to suit the features of individual data. Previous studies suggest that using pre-trained models for transfer learning or dividing into sub-problems can accelerate the training process^{247,248,73}.

The next steps of the application include validation using additional data from *in vivo* or *ex vivo* models. Real data of viscoelastic tissues will be necessary to improve the robustness of this algorithm. Although I used porcine liver tissue in our *ex vivo* experiment, tissue samples of lesions are desired for the shear wave elastography study.

Other complex equations can be used to model shear wave imaging, such as including viscoelasticity^{225,70,73}, or higher dimensions²⁴⁵. Another possible approach is to develop PDE/ODE-regularized DL methods in a wider range of ultrasound applications. For example, using PDEs for thermal diffusivity to monitor temperature during focused ultrasound therapy could serve as a means of quality assurance. Recent progress in diffusion models has shown potential in the reconstruction of medical images^{249,250,251}. The iterative algorithm can be exploited to solve denoising or reconstruction problems of SWE.

5.5 CONCLUSION

I propose a multi-scale spatial-temporal SELFNet framework to estimate displacement from noisy data. SELFNet introduces a Fourier feature mapping and an additional network for the shear modulus to PINN. The mapping enhances the sparsity of the input data, thus facilitating the learning of high-frequency information in shear wave elastography displacement data. During training, SELFNet simultaneously estimates displacement, its related derivative fields, and shear modulus. Using noisy displacement signals from 5-angle CPWC ultrasound images after an ARF push, SELFNet reduced, by 51% and 17%, the relative ℓ_2 error over the original data and the Gaussian-filtered data, respectively. With the same number of trainable parameters, it improved the elasticity reconstruction compared to PINN and MLP. The reconstructed SELFNet achieved a final RMSE of 1.76 kPa and an SSIM of 0.949, showing strong agreement with the ground truth. Moreover, SELFNet underwent testing on *ex vivo* viscoelastic tissues and continued to produce matched results. Collectively, these results indicate that SELF-

Net effectively reduces noise in SWE with fewer data acquisitions, and the introduction of Fourier feature mapping strengthens the network's learning ability for shear waves, which is potentially beneficial for clinical applications such as DVT or liver disease.

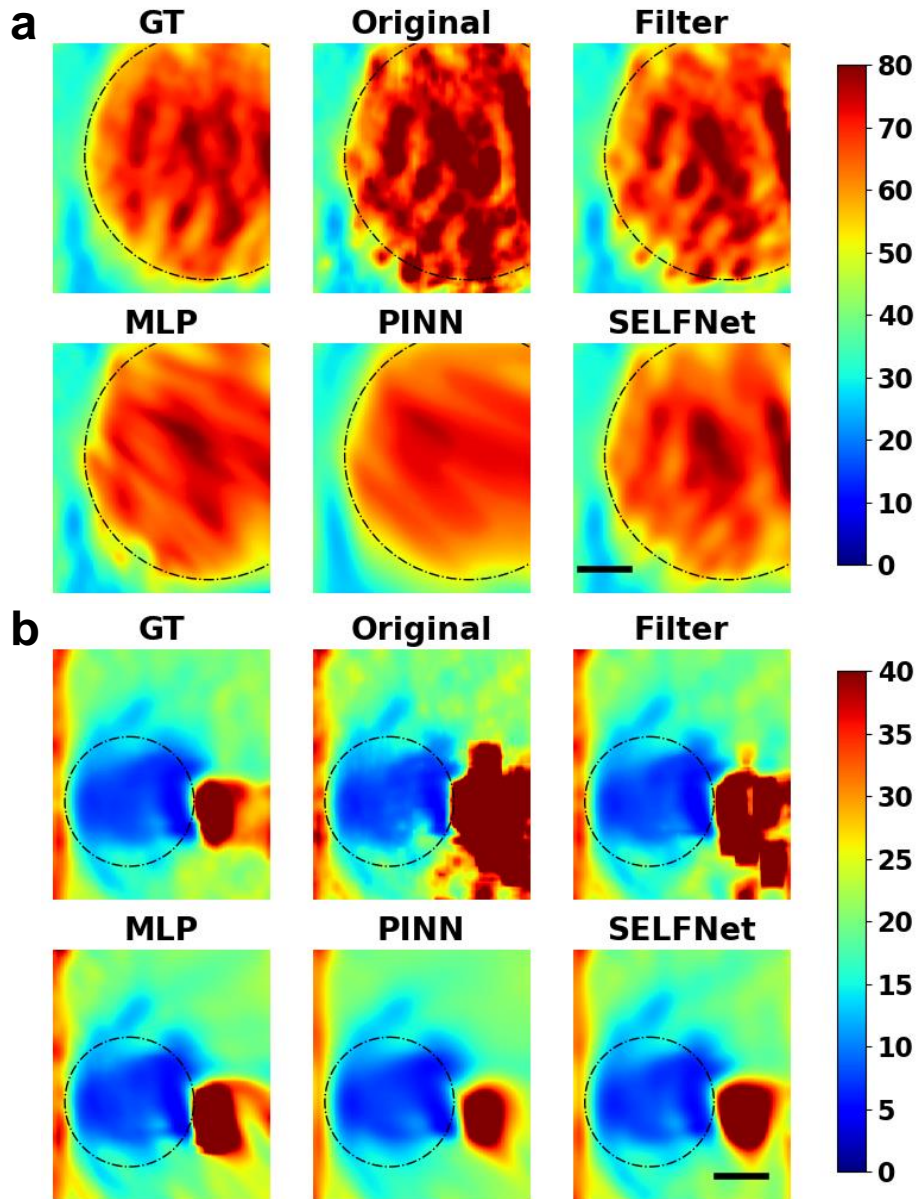


Figure 5.11: Reconstruction of Young's modulus in phantom of (a) a type VI lesion and (b) a type I lesion. (a) The mismatch of pattern inside the lesion decreases SSIM of reconstructed elasticity, with respect to ground-truth. (b) The artifacts occur when the shear wave leaves the lesion, resulting in increasing RMSE. The lesions are indicated by the dash-dotted circle. A scalebar of 2 mm is included.

Conclusion and Future Directions

6.1 SUMMARY

Therapy for deep vein thrombosis (DVT) is a rapidly growing topic of research, given the annual population affected by DVT. Using ultrasound for drug delivery tasks, sonothrombolysis offers accelerated resolution of blood clots and seems to be a potential approach for DVT treatment with reduced bleeding risk. However, the acoustic parameters and the choice of microbubble (MB) have not yet been determined for optimal performance. In this dissertation, microfluidically produced MBs was delivered to blood clots as therapeutic agents for sonothrombolysis. Precise production in terms of size was implemented using a micro Coulter particle counter (μ CPC) and proportional-integral (PI) controller within a microfluidic device. Subsequently, a 3D imaging technique was implemented to allow quantification of the *in vivo* sonothrombolysis experiment in a rodent model of DVT. The efficacy of large-diameter MBs was then validated in the animal model and compared to other control conditions. Finally, a model-based algorithm

was proposed for shear wave elastography, which can be applied for enhanced imaging of DVT.

The results of this dissertation suggest that microfluidically produced MB is a safe and controllable method in DVT therapy. The key results are summarized as follows.

1. **Real-time *in situ* measurement and control of microbubbles from microfluidic devices.** In Chapter 2, I implemented a closed-loop feedback control system in a flow-focusing microfluidic device with integrated on-chip electrodes. Using our system, microbubbles between 13 – 28 μm in diameter were measured and counted, and their diameter was controlled using a PI controller. The measurements were validated against an optical reference with $R^2 = 0.98$ and achieved a maximum production rate of $1.4 \times 10^5/\text{s}$. Using the feedback control system, the device enabled control in microbubble diameter in the range of 14 – 24 μm .
2. **Development of a quantitative method for DVT in a murine model using 3D ultrasound imaging.** In Chapter 3, a quantitative evaluation of the volume of DVT was achieved using 3D high-frequency ultrasound imaging and a segmentation tool in a murine model. The measured 3D volume of blood clots was compared with the *in vitro* blood clot weights, resulting in a R^2 coefficient of 0.89. In the *in vivo* mouse model, this method was confirmed with a cylindrical volume from macroscopic measurement, showing an R^2 coefficient of 0.91.
3. **Validation of efficacy using microfluidically produced microbubbles in sonothrombolysis for DVT.** Chapter 4 demonstrates the use of transiently stable microbubbles and ultrasound to improve the resolution of blood clots in a mouse model of

pre-existing DVT. During therapy, microbubbles and thrombolytic agents were administered through a tail vein catheter, while ultrasound was applied to the abdominal region of the mice. Three-dimensional ultrasound scans were performed before and after therapy for quantification. The therapy using microfluidically produced MBs and ultrasound documented a significant reduction in DVT volume, where the residual volume was 20% versus 52% in the no-therapy control ($p = 0.012 < 0.05$). Histological analysis of tissue sections showed a reduction in DVT volume post-therapy. The findings indicate that large microbubbles generated from a microfluidic device show promise in ultrasound-assisted therapy to address concerns related to venous thromboembolism.

- 4. Design of a physics-model-based denoising method for shear wave elastography.** Chapter 5 introduces a Shear wave ELastography Fourier feature Network (SELFNet) using spatial-temporal random Fourier features to estimate and denoise particle displacement signals. The findings of *in vitro* and *ex vivo* experiments indicate that SELFNet is capable of smoothing out the noise in phantom lesions with different stiffness and sizes, outperforming a reference Gaussian filtering method by 17% in relative ℓ_2 error, 45% in root mean square error (RMSE) and 0.03 in structural similarity (SSIM), respectively. Furthermore, the ablation study suggests that SELFNet can prevent over-fitting through the Fourier feature mapping module. The implementation of SELFNet can denoise shear wave elastography data with limited acquisitions and improve elasticity reconstruction. In this context, subject to successful translation, it has the potential to be extended to clinical applications, such as the diagnosis of DVT, cancer or liver disease.

In Chapter 2, the μ CPC detects the volume of particles based on the Coulter principle²⁵². The measurement system is customized for the geometry of the microfluidic device and the size of the produced MBs. In addition to my application for sonothrombolysis in Chapter 4, microfluidics has the potential for further clinical translation. Nanobubbles at sub-micron size have been produced using microfluidic techniques^{253,254}. Reducing the size of the particles remains a challenge limited by microfabrication techniques and material properties. Microfluidics has also been reported to provide on-demand drug release²⁵⁵, or the targeted function by adding ligands to the continuous phase²⁵⁶. Microfluidics can generate controllable, monodisperse products of high concentration for biomedical applications, such as imaging or drug delivery.

The results in Chapter 5 use a Gaussian filtering method for comparison. The current physics-informed method is an unsupervised deep learning method. Since convolutional neural network (CNN) requires pairwise input and reference data for training, a benchmarking of physics-informed neural network (PINN) with CNN is not fair. However, evaluating the distinction between these two approaches is essential to determine the scenarios of their applications. PINN-based method is appropriate for a small amount of data without knowing the ground-truth, while the CNN-based algorithms are advantageous in inference time.

6.2 FUTURE DIRECTIONS

The findings of this dissertation and other research articles suggest some possible directions for sonothrombolysis therapy, microfluidics techniques, and model-based algorithms for ultrasound imaging.

6.2.1 EVALUATION OF POST THROMBOTIC SYNDROME

Post-thrombotic syndrome (PTS) is the complication developed from DVT. The manifestations of PTS range from mild symptoms such as edema, to pain, and even life-threatening conditions. However, there is still an unmet need for PTS, as it cannot be fully cured. PTS is associated with chronic DVT, therefore, one possible direction of this dissertation involves the removal efficacy of our sonothrombolysis technique for chronic DVT. Sonothrombolysis therapy can be used to resolve the *in vitro* blood clot model mentioned in Chapter 3. After optimizing the MB and ultrasound parameters for chronic DVT, an *in vivo* study will investigate its influence on the vessel walls of the veins. Since there are no treatments that can cure PTS, improving the quality of life through the sonothrombolysis technique will represent a significant advancement.

6.2.2 CATHETER FOR SONOTHROMBOLYSIS THERAPY

The ultrasound transducer and microfluidics can be micro-fabricated in one catheter. There has been growing interest in therapeutic ultrasound compatible with the human cardiovascular system. Side-viewing transducers have been used to assist in thrombolysis in commercial applications and research studies^{116,189,156,190}. Recently, a novel design of forward-viewing transducers has also been developed to enhance sonothrombolysis, evolving from a single element to multiple elements to induce vortex ultrasound^{187,188,165}. One benefit of the micro-Coulter counter approach in Chapter 2 is its operation without microscopic observation. The on-site production of microbubbles with an integrated therapeutic transducer aggressively improves recanalization, thus reducing the duration of therapy. In addition, the ultrasound transducer might be used for

intravascular imaging. Incorporating imaging capability enables real-time monitoring of blood clot volumes, and the dosage of thrombolytic agents can be adjusted as needed to minimize bleeding risks.

6.2.3 DUAL FUNCTION ULTRASOUND FOR DEEP VEIN THROMBOSIS

Non-invasive ultrasound imaging is recommended for thrombolysis therapy. As an alternative to a transducer-integrated catheter, shear wave elastography (SWE) have also shown potential in thrombolysis therapy²⁵⁷. The difference stiffness between a thrombus and its surrounding tissues can enhance image contrast, aiding in estimating the thrombus size. During therapy, real-time estimate of the size and stiffness of a thrombus can offer information such as the lysis rate and the composition of the residual thrombus²⁵⁸. Furthermore, the ARFs applied by the transducer in SWE can induce mechanical effects, to facilitate cavitation of microbubbles or dissolution of the thrombus. Consequently, a transducer can provide therapeutic ultrasound and simultaneously characterize blood clots. However, an appropriate frequency of the transducer has to be chosen as it affects the depth and resolution of the imaging. A custom sequence switching among imaging, therapeutic ARFs and SWE ARFs should be programmed for this application, as illustrated in Fig. 6.1.

6.2.4 MODEL-BASED ALGORITHMS FOR ULTRASOUND IMAGING

In the field of medical imaging, the physics behind each imaging modality forms the foundation for visualizing the interior of the human body. For example, real ultrasound imaging signals are based on propagation of ultrasound waves. PINNs can in-

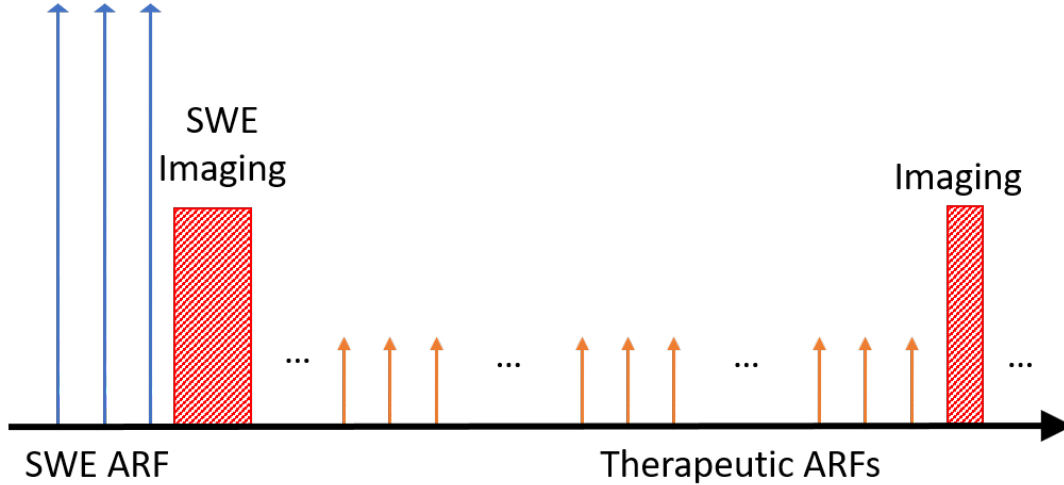


Figure 6.1: Sequence for dual function ultrasound in sonothrombolysis. Ultrasound is switching among SWE ARF, therapeutic ARF and imaging modes.

clude PDEs as a regularization term to estimate unknown data, or provide a solution to forward/reverse problems. With known physical partial differential equations (PDEs), PINN can be extended to enhance MBs in video sequences, or to monitor temperature changes during high-intensity focused ultrasound therapy. Despite these applications, further translation to medical imaging will still require instant display of the processed results. PINN can be accelerated by dividing into sub-problems or pre-training. For practical implementation, fully trained neural networks are recommended as they do not require extra training. Diffusion models, or generative AI models, combine the benefit of iterative methods and data-driven models, becoming a focus of current deep learning research^{259,249}. The diffusion models have been extended to medical imaging reconstruction^{260,251}. The network proposed in Chapter 5 could be rewritten in the diffusion model^{261,262} or incorporated with traditional convolution neural networks²¹⁹. Input images are encoded into a latent space matching the training data, and latent variables are

iteratively decoded from a network trained with physics-informed regularization. Therefore, it can effectively decrease the computation time compared to PINN and generate prediction in near real-time, while still being governed by the laws of physics.

Peer-reviewed Journal Publications

- [1] Y. Xie, Y. Huang, H. C. S. Stevenson, L. Yin, K. Zhang, Z. H. Islam, W. A. Marcum, C. Johnston, N. Hoyt, E. W. Kent, B. Wang, and J. A. Hossack, “A Quantitative Method for the Evaluation of Deep Vein Thrombosis in a Murine Model Using Three-Dimensional Ultrasound Imaging,” *Biomedicines*, vol. 12, no. 1, Art. no. 1, Jan. 2024.
- [2] Y. Huang, E. B. Herbst, Y. Xie, L. Yin, Z. H. Islam, E. W. Kent, B. Wang, A. L. Klibanov, and J. A. Hossack, “In Vivo Validation of Modulated Acoustic Radiation Force–Based Imaging in Murine Model of Abdominal Aortic Aneurysm Using VEGFR-2–Targeted Microbubbles,” *Investigative Radiology*, vol. 58, no. 12, p. 865, Dec. 2023.
- [3] Y. Xie, A. J. Dixon, J. M. R. Rickel, A. L. Klibanov, and J. A. Hossack, “Closed-loop feedback control of microbubble diameter from a flow-focusing microfluidic device,” *Biomicrofluidics*, vol. 14, no. 3, p. 034101, May 2020.
- [4] Y. Xie, Y. Huang, H. C. S. Stevenson, L. Yin, K. Zhang, Z. H. Islam, W. A. Marcum, C. Johnston, N. Hoyt, E. W. Kent, B. Wang, and J. A. Hossack, “Sonothrom-

bolysis using Microfluidically-Produced Microbubbles in a Murine Model of Deep Vein Thrombosis,” *Annals of Biomedical Engineering* (Under review).

- [5] Y. Xie, Y. Huang, J. A. Hossack, ”SELFNet: Denoising Shear Wave elastography using spatial-temporal Fourier Feature Networks,” *Ultrasound in Medicine & Biology* (Submitted).

Conference Abstracts and Presentations

- [1] Y. Xie, Y. Huang, J. A. Hossack, "Sonothrombolysis in a Murine Model of Deep Vein Thrombosis Using Microfluidically Produced Microbubbles." In The 29th European symposium on Ultrasound Contrast Imaging, Jan. 2024, Rotterdam, The Netherlands. (Poster)

- [2] Y. Xie, Y. Huang, J. A. Hossack, "Elevation Direction Deconvolution in 3D Super-Resolution Ultrasound Imaging." In 2023 IEEE International Ultrasonics Symposium (IUS), Sep. 2023, Montreal, Canada. (Poster)

- [3] Y. Huang, Y. Xie, J. A. Hossack, "Validation of Normalized Singular Spectrum Area Measurement by Optical Observation of Adherent Microbubble Displacements and Numerical Simulation." In 2023 IEEE International Ultrasonics Symposium (IUS), Sep. 2023, Montreal, Canada. (Poster)

- [4] Y. Xie, Y. Huang, J. A. Hossack, "Propagation of shear wave in elastography using physics-informed neural network." In 2022 IEEE International Ultrasonics Symposium (IUS), Sep. 2022, Venice, Italy. (Poster)

- [5] P. R. Lozano, K. Kohli, A. Robinson, Y. Xie, F. Zhao, V. Sadri, S. Gooden, M. Samaee, A. Thim, M. Morsy, A. Klibanov, C. M. Kramer, J. A. Hossack, and A. P. Yoganathan, "Functional effects of therapeutic ultrasound for calcific degenerative mitral stenosis," In the American College of Cardiology's 71st Annual Scientific Session and Expo, Mar. 2022, Washington, D.C., USA. (Poster)
- [6] Y. Huang, Y. Xie, J. A. Hossack, "Optical Validation of Normalized Singular Spectrum Area Measurement by Observing Adherent Microbubble Small Displacements." In The 28th European symposium on Ultrasound Contrast Imaging, Jan. 2023, Rotterdam, The Netherlands. (Poster)
- [7] P. Rodriguez Lozano, A. A. Robinson, A. Thim, F. Zhao, Y. Xie, T. Dassanayaka, P. Miller, A. L. Klibanov, C. M. Kramer, and J. A. Hossack, "Feasibility of Therapeutic Ultrasound Delivery for the Treatment of Mitral Stenosis," In American Heart Association Scientific Sessions, Nov. 2021, Boston, USA. (Poster)
- [8] Y. Xie, S. G. Sathyanarayana, and J. A. Hossack, "Hierarchical Compressed Sensing for High Frame Rate Tissue Harmonic Imaging," In 2021 IEEE International Ultrasonics Symposium (IUS), Sep. 2021, pp. 1–3, Xi'an, China (Poster)
- [9] Y. Xie, A. J. Dixon, R. Montayre, and J. A. Hossack, "Controlling microbubble diameters from a flow focusing microfluidics device." In The 25 th European symposium on Ultrasound Contrast Imaging, Jan. 2020, Rotterdam, The Netherlands. (Poster)
- [10] J. R. Rickel, A. J. Dixon, Y. Xie, J. A. Hossack, "Catheter-based, instrumented, flow focusing microfluidics device for production, counting and sizing of monodis-

perse microbubbles optimized for sonothrombolysis.” In The 24th European symposium on Ultrasound Contrast Imaging, Jan. 2020, Rotterdam, The Netherlands. (Poster)

- [11] Y. Xie, A. J. Dixon, J. M. R. Rickel, and J. A. Hossack, “Real-time Control of Microbubble Diameter from a Flow Focusing Microfluidic Device,” In 2019 IEEE International Ultrasonics Symposium (IUS), Oct. 2019, pp. 1074–1076, Glasgow, UK. (Oral)

References

- [1] T. L. Szabo, *Diagnostic Ultrasound Imaging: Inside Out*. Academic Press, Sep. 2004.
- [2] J.-M. Escoffre and A. Bouakaz, Eds., *Therapeutic Ultrasound*, ser. Advances in Experimental Medicine and Biology. Cham: Springer International Publishing, 2016, vol. 880.
- [3] F. M. Abu-Zidan, A. F. Hefny, and P. Corr, “Clinical ultrasound physics,” *Journal of Emergencies, Trauma and Shock*, vol. 4, no. 4, pp. 501–503, 2011.
- [4] P. Laugier and G. Haïat, “Introduction to the Physics of Ultrasound,” in *Bone Quantitative Ultrasound*, P. Laugier and G. Haïat, Eds. Dordrecht: Springer Netherlands, 2011, pp. 29–45.
- [5] J. A. Jensen, “Medical ultrasound imaging,” *Progress in Biophysics and Molecular Biology*, vol. 93, no. 1, pp. 153–165, Jan. 2007.
- [6] D. Savéry and G. Cloutier, “High-frequency ultrasound backscattering by blood: Analytical and semianalytical models of the erythrocyte cross section,” *The Journal of the Acoustical Society of America*, vol. 121, no. 6, pp. 3963–3971, Jun. 2007.
- [7] J. A. Jensen, M. A. Naji, S. K. Præsius, I. Taghavi, M. Schou, L. N. Hansen, S. B. Andersen, S. B. Søgaaard, N. S. Panduro, C. M. Sørensen, M. B. Nielsen, C. Gundlach, H. M. Kjer, A. B. Dahl, B. G. Tomov, M. L. Ommen, N. B. Larsen, and E. V. Thomsen, “Super Resolution Ultrasound Imaging using the Erythrocytes: I: Density Images,” *IEEE Transactions on Ultrasonics, Ferroelectrics, and Frequency Control*, pp. 1–1, 2024.
- [8] M. A. Naji, I. Taghavi, M. Schou, S. K. Præsius, L. N. Hansen, N. S. Panduro, S. B. Andersen, S. B. Søgaaard, C. Gundlach, H. M. Kjer, B. G. Tomov, E. V.

- Thomsen, M. B. Nielsen, N. B. Larsen, A. B. Dahl, C. M. Sørensen, and J. A. Jensen, “Super Resolution Ultrasound Imaging Using the Erythrocytes: II: Velocity Images,” *IEEE Transactions on Ultrasonics, Ferroelectrics, and Frequency Control*, pp. 1–1, 2024.
- [9] E. Franceschini, R. K. Saha, and G. Cloutier, “Comparison of three scattering models for ultrasound blood characterization,” *IEEE Transactions on Ultrasonics, Ferroelectrics, and Frequency Control*, vol. 60, no. 11, pp. 2321–2334, Nov. 2013.
- [10] E. Quaia, “Assessment of tissue perfusion by contrast-enhanced ultrasound,” *European Radiology*, vol. 21, no. 3, pp. 604–615, Mar. 2011.
- [11] A. L. Emanuel, R. I. Meijer, E. van Poelgeest, P. Spoor, E. H. Serné, and E. C. Eringa, “Contrast-enhanced ultrasound for quantification of tissue perfusion in humans,” *Microcirculation*, vol. 27, no. 1, p. e12588, 2020.
- [12] A. A. Doinikov, J. F. Haac, and P. A. Dayton, “Resonance frequencies of lipid-shelled microbubbles in the regime of nonlinear oscillations,” *Ultrasonics*, vol. 49, no. 2, pp. 263–268, Feb. 2009.
- [13] M. Postema and O. H. Gilja, “Contrast-enhanced and targeted ultrasound,” *World Journal of Gastroenterology : WJG*, vol. 17, no. 1, pp. 28–41, Jan. 2011.
- [14] C. Errico, J. Pierre, S. Pezet, Y. Desailly, Z. Lenkei, O. Couture, and M. Tanter, “Ultrafast ultrasound localization microscopy for deep super-resolution vascular imaging,” *Nature*, vol. 527, no. 7579, pp. 499–502, Nov. 2015.
- [15] K. Christensen-Jeffries, R. J. Browning, M.-X. Tang, C. Dunsby, and R. J. Eckersley, “In Vivo Acoustic Super-Resolution and Super-Resolved Velocity Mapping Using Microbubbles,” *IEEE Transactions on Medical Imaging*, vol. 34, no. 2, pp. 433–440, Feb. 2015.
- [16] K. Ferrara, R. Pollard, and M. Borden, “Ultrasound Microbubble Contrast Agents: Fundamentals and Application to Gene and Drug Delivery,” *Annual Review of Biomedical Engineering*, vol. 9, no. Volume 9, 2007, pp. 415–447, Aug. 2007.
- [17] J. M. Tsutsui, F. Xie, and R. T. Porter, “The use of microbubbles to target drug delivery,” *Cardiovascular Ultrasound*, vol. 2, p. 23, Nov. 2004.

- [18] S. Chen, R. V. Shohet, R. Bekeredjian, P. Frenkel, and P. A. Grayburn, "Optimization of ultrasound parameters for cardiac gene delivery of adenoviral or plasmid deoxyribonucleic acid by Ultrasound-Targeted microbubble destruction," *Journal of the American College of Cardiology*, vol. 42, no. 2, pp. 301–308, Jul. 2003.
- [19] Y. Taniyama, K. Tachibana, K. Hiraoka, T. Namba, K. Yamasaki, N. Hashiya, M. Aoki, T. Ogihara, K. Yasufumi, and R. Morishita, "Local Delivery of Plasmid DNA Into Rat Carotid Artery Using Ultrasound," *Circulation*, vol. 105, no. 10, pp. 1233–1239, Mar. 2002.
- [20] C. A. Sennoga, J. S. M. Yeh, J. Alter, E. Stride, P. Nihoyannopoulos, J. M. Seddon, D. O. Haskard, J. V. Hajnal, M.-X. Tang, and R. J. Eckersley, "Evaluation of Methods for Sizing and Counting of Ultrasound Contrast Agents," *Ultrasound in Medicine & Biology*, vol. 38, no. 5, pp. 834–845, May 2012.
- [21] P. Garstecki, M. J. Fuerstman, H. A. Stone, and G. M. Whitesides, "Formation of droplets and bubbles in a microfluidic T-junction—scaling and mechanism of break-up," *Lab on a Chip*, vol. 6, no. 3, pp. 437–446, Feb. 2006.
- [22] A. M. Gañán-Calvo and J. M. Gordillo, "Perfectly Monodisperse Microbubbling by Capillary Flow Focusing," *Physical Review Letters*, vol. 87, no. 27, p. 274501, Dec. 2001.
- [23] P. Garstecki, I. Gitlin, W. DiLuzio, G. M. Whitesides, E. Kumacheva, and H. A. Stone, "Formation of monodisperse bubbles in a microfluidic flow-focusing device," *Applied Physics Letters*, vol. 85, no. 13, pp. 2649–2651, Sep. 2004.
- [24] K. Hettiarachchi, E. Talu, M. L. Longo, P. A. Dayton, and A. P. Lee, "On-chip generation of microbubbles as a practical technology for manufacturing contrast agents for ultrasonic imaging," *Lab on a Chip*, vol. 7, no. 4, p. 463, 2007.
- [25] E. Castro-Hernández, W. van Hoeve, D. Lohse, and J. M. Gordillo, "Microbubble generation in a co-flow device operated in a new regime," *Lab on a Chip*, vol. 11, no. 12, p. 2023, 2011.
- [26] T. Segers, L. de Rond, N. de Jong, M. Borden, and M. Versluis, "Stability of Monodisperse Phospholipid-Coated Microbubbles Formed by Flow-Focusing at High Production Rates," *Langmuir*, vol. 32, no. 16, pp. 3937–3944, Apr. 2016.

- [27] K. W. Pulsipher, D. A. Hammer, D. Lee, and C. M. Sehgal, “Engineering Theranostic Microbubbles Using Microfluidics for Ultrasound Imaging and Therapy: A Review,” *Ultrasound in Medicine & Biology*, vol. 44, no. 12, pp. 2441–2460, Dec. 2018.
- [28] E. Stride, “Physical Principles of Microbubbles for Ultrasound Imaging and Therapy,” *Cerebrovascular Diseases*, vol. 27, no. Suppl. 2, pp. 1–13, Apr. 2009.
- [29] J. L. Chen, A. H. Dhanaliwala, A. J. Dixon, A. L. Klibanov, and J. A. Hossack, “Synthesis and Characterization of Transiently Stable Albumin-Coated Microbubbles via a Flow-Focusing Microfluidic Device,” *Ultrasound in Medicine & Biology*, vol. 40, no. 2, pp. 400–409, Feb. 2014.
- [30] A. H. Dhanaliwala, J. L. Chen, S. Wang, and J. A. Hossack, “Liquid flooded flow-focusing microfluidic device for in situ generation of monodisperse microbubbles,” *Microfluid Nanofluid*, p. 11, 2013.
- [31] A. J. Dixon, J. M. R. Rickel, B. D. Shin, A. L. Klibanov, and J. A. Hossack, “In Vitro Sonothrombolysis Enhancement by Transiently Stable Microbubbles Produced by a Flow-Focusing Microfluidic Device,” *Annals of Biomedical Engineering*, vol. 46, no. 2, pp. 222–232, Feb. 2018.
- [32] A. J. Dixon, J. Li, J.-M. R. Rickel, A. L. Klibanov, Z. Zuo, and J. A. Hossack, “Efficacy of Sonothrombolysis Using Microbubbles Produced by a Catheter-Based Microfluidic Device in a Rat Model of Ischemic Stroke,” *Annals of Biomedical Engineering*, vol. 47, no. 4, pp. 1012–1022, Apr. 2019.
- [33] P. A. Kyrle and S. Eichinger, “Deep vein thrombosis,” *The Lancet*, vol. 365, no. 9465, pp. 1163–1174, Mar. 2005.
- [34] C. W. Tsao, A. W. Aday, Z. I. Almarzooq, C. A. Anderson, P. Arora, C. L. Avery, C. M. Baker-Smith, A. Z. Beaton, A. K. Boehme, A. E. Buxton, Y. Commodore-Mensah, M. S. Elkind, K. R. Evenson, C. Eze-Nliam, S. Fugar, G. Generoso, D. G. Heard, S. Hiremath, J. E. Ho, R. Kalani, D. S. Kazi, D. Ko, D. A. Levine, J. Liu, J. Ma, J. W. Magnani, E. D. Michos, M. E. Mussolino, S. D. Navaneethan, N. I. Parikh, R. Poudel, M. Rezk-Hanna, G. A. Roth, N. S. Shah, M.-P. St-Onge, E. L. Thacker, S. S. Virani, J. H. Voeks, N.-Y. Wang, N. D. Wong, S. S. Wong, K. Yaffe, S. S. Martin, and n. null, “Heart Disease and Stroke Statistics—2023 Update: A Report From the American Heart Association,” *Circulation*, vol. 147, no. 8, pp. e93–e621, Feb. 2023.

- [35] G. Agnelli, H. R. Buller, A. Cohen, M. Curto, A. S. Gallus, M. Johnson, U. Masiukiewicz, R. Pak, J. Thompson, G. E. Raskob, and J. I. Weitz, “Oral Apixaban for the Treatment of Acute Venous Thromboembolism,” *New England Journal of Medicine*, vol. 369, no. 9, pp. 799–808, Aug. 2013.
- [36] “Oral Rivaroxaban for Symptomatic Venous Thromboembolism,” *New England Journal of Medicine*, vol. 363, no. 26, pp. 2499–2510, Dec. 2010.
- [37] P. Prandoni, F. Noventa, A. Ghirarduzzi, V. Pengo, E. Bernardi, R. Pesavento, M. Iotti, D. Tormene, P. Simioni, and A. Pagnan, “The risk of recurrent venous thromboembolism after discontinuing anticoagulation in patients with acute proximal deep vein thrombosis or pulmonary embolism. A prospective cohort study in 1,626 patients,” *Haematologica*, vol. 92, no. 2, pp. 199–205, Feb. 2007.
- [38] L. Watson, C. Broderick, and M. P. Armon, “Thrombolysis for acute deep vein thrombosis,” *Cochrane Database of Systematic Reviews*, no. 11, 2016.
- [39] S. Vedantham, S. Z. Goldhaber, J. A. Julian, S. R. Kahn, M. R. Jaff, D. J. Cohen, E. Magnuson, M. K. Razavi, A. J. Comerota, H. L. Gornik, T. P. Murphy, L. Lewis, J. R. Duncan, P. Nieters, M. C. Derfler, M. Fillion, C.-S. Gu, S. Kee, J. Schneider, N. Saad, M. Blinder, S. Moll, D. Sacks, J. Lin, J. Rundback, M. Garcia, R. Razdan, E. VanderWoude, V. Marques, and C. Kearon, “Pharmacomechanical Catheter-Directed Thrombolysis for Deep-Vein Thrombosis,” *New England Journal of Medicine*, vol. 377, no. 23, pp. 2240–2252, Dec. 2017.
- [40] R. S. Winokur and A. K. Sista, “DVT Intervention in the Post-ATTRACT Era,” *Current Treatment Options in Cardiovascular Medicine*, vol. 20, no. 9, p. 70, Aug. 2018.
- [41] K. B. Bader, M. J. Gruber, and C. K. Holland, “Shaken and Stirred: Mechanisms of Ultrasound-Enhanced Thrombolysis,” *Ultrasound in Medicine & Biology*, vol. 41, no. 1, pp. 187–196, Jan. 2015.
- [42] C. W. Francis, A. Blinc, S. Lee, and C. Cox, “Ultrasound accelerates transport of recombinant tissue plasminogen activator into clots,” *Ultrasound in Medicine & Biology*, vol. 21, no. 3, pp. 419–424, 1995.
- [43] A. V. Alexandrov, M. Köhrmann, L. Soinne, G. Tsivgoulis, A. D. Barreto, A. M. Demchuk, V. K. Sharma, R. Mikulik, K. W. Muir, G. Brandt, J. Alleman, J. C. Grotta, C. R. Levi, C. A. Molina, M. Saqqur, D. Mavridis, T. Psaltopoulou, M. Vosko, J. B. Fiebach, P. Mandava, T. A. Kent, A. W. Alexandrov, and P. D.

- Schellinger, “Safety and efficacy of sonothrombolysis for acute ischaemic stroke: A multicentre, double-blind, phase 3, randomised controlled trial,” *The Lancet Neurology*, vol. 18, no. 4, pp. 338–347, Apr. 2019.
- [44] H. Wu, B. Zhang, J. Kim, G. Owens, G. Stocker, M. Chen, A. Cornett, K. Bautista, P. A. Dayton, Z. Xu, and X. Jiang, “In-vivo sonothrombolysis with a forward-viewing ultrasound balloon catheter in a swine deep vein thrombosis (DVT) model,” in *2023 IEEE International Ultrasonics Symposium (IUS)*, Sep. 2023, pp. 1–4.
- [45] W. Mathias, J. M. Tsutsui, B. G. Tavares, A. M. Fava, M. O. D. Aguiar, B. C. Borges, M. T. Oliveira, A. Soeiro, J. C. Nicolau, H. B. Ribeiro, H. P. Chiang, J. C. N. Sbrano, A. Morad, A. Goldsweig, C. E. Rochitte, B. B. C. Lopes, J. A. F. Ramirez, F. R. Kalil, T. R. Porter, and n. null, “Sonothrombolysis in ST-Segment Elevation Myocardial Infarction Treated With Primary Percutaneous Coronary Intervention,” *Journal of the American College of Cardiology*, vol. 73, no. 22, pp. 2832–2842, Jun. 2019.
- [46] M. O. Aguiar, B. G. Tavares, J. M. Tsutsui, A. M. Fava, B. C. Borges, M. T. Oliveira, A. Soeiro, J. C. Nicolau, H. B. Ribeiro, H. P. Chiang, J. C. Sbrano, A. Goldsweig, C. E. Rochitte, B. B. Lopes, J. A. Ramirez, R. Kalil Filho, T. R. Porter, and W. Mathias, “Sonothrombolysis Improves Myocardial Dynamics and Microvascular Obstruction Preventing Left Ventricular Remodeling in Patients With ST Elevation Myocardial Infarction,” *Circulation: Cardiovascular Imaging*, vol. 13, no. 4, p. e009536, Apr. 2020.
- [47] S. A. N. Doelare, J. H. Nederhoed, J. M. Evers, S. T. Roos, O. Kamp, R. J. P. Musters, W. Wisselink, V. Jongkind, H. P. Ebben, and K. K. Yeung, “Feasibility of Microbubble-Accelerated Low-Dose Thrombolysis of Peripheral Arterial Occlusions Using an Ultrasound Catheter,” *Journal of Endovascular Therapy*, p. 15266028221126938, Sep. 2022.
- [48] R. H. White, J. P. McGahan, M. M. Daschbach, and R. P. Hartling, “Diagnosis of Deep-Vein Thrombosis Using Duplex Ultrasound,” *Annals of Internal Medicine*, vol. 111, no. 4, pp. 297–304, Aug. 1989.
- [49] C. Male, P. Chait, J. S. Ginsberg, K. Hanna, M. Andrew, J. Halton, R. Anderson, P. McCusker, J. Wu, T. Abshire, I. Cherrick, D. Mahoney, and L. Mitchell, “Comparison of Venography and Ultrasound for the Diagnosis of Asymptomatic Deep Vein Thrombosis in the Upper Body in Children,” *Thrombosis and Haemostasis*, vol. 87, no. 4, pp. 593–598, 2002.

- [50] L. Zhao, S. J. Prior, M. Kampmann, J. D. Sorkin, K. Caldwell, M. Braganza, S. McEvoy, and B. K. Lal, "Measurement of thrombus resolution using three-dimensional ultrasound assessment of deep vein thrombosis volume," *Journal of Vascular Surgery: Venous and Lymphatic Disorders*, vol. 2, no. 2, pp. 140–147, Apr. 2014.
- [51] L. Zhao, R. Patel, S. Sikdar, and S. J. Prior, "Comparison of Freehand 3D and 4D Ultrasound to Measure Thrombus Volume in Patients with Acute Deep Vein Thrombosis:," *Journal for Vascular Ultrasound*, Mar. 2018.
- [52] P. Hoang, "Elastography techniques in the evaluation of deep vein thrombosis," *Cardiovascular Diagnosis and Therapy*, vol. 7, no. S3, pp. S238–S245, Dec. 2017.
- [53] M. Fatemi and J. F. Greenleaf, "Ultrasound-Stimulated Vibro-Acoustic Spectrography," *Science*, vol. 280, no. 5360, pp. 82–85, Apr. 1998.
- [54] G. Montaldo, M. Tanter, J. Bercoff, N. Benech, and M. Fink, "Coherent plane-wave compounding for very high frame rate ultrasonography and transient elastography," *IEEE Transactions on Ultrasonics, Ferroelectrics, and Frequency Control*, vol. 56, no. 3, pp. 489–506, Mar. 2009.
- [55] C. Schmitt, E. Montagnon, A. Hadj Henni, S. Qi, and G. Cloutier, "Shear Wave Induced Resonance Elastography of Venous Thrombi: A Proof-of-Concept," *IEEE Transactions on Medical Imaging*, vol. 32, no. 3, pp. 565–577, Mar. 2013.
- [56] G. Bosio, N. Zenati, F. Destrepes, B. Chayer, G. Pernod, and G. Cloutier, "Shear Wave Elastography and Quantitative Ultrasound as Biomarkers to Characterize Deep Vein Thrombosis In Vivo," *Journal of Ultrasound in Medicine*, vol. 41, no. 7, pp. 1807–1816, 2022.
- [57] C. Pellot-Barakat, L. Chami, J. M. Correias, M. Lefort, and O. Lucidarme, "Does motion affect liver stiffness estimates in shear wave elastography? Phantom and clinical study," *European Journal of Radiology*, vol. 85, no. 9, pp. 1645–1650, Sep. 2016.
- [58] H. J. Shin, M.-J. Kim, C.-S. Yoon, K. Lee, K. S. Lee, J.-C. Park, M.-J. Lee, and H. Yoon, "Motion effects on the measurement of stiffness on ultrasound shear wave elastography: A moving liver fibrosis phantom study," *Medical Ultrasonography*, vol. 20, no. 1, pp. 14–20, Feb. 2018.

- [59] K. Hornik, M. Stinchcombe, and H. White, “Multilayer feedforward networks are universal approximators,” *Neural Networks*, vol. 2, no. 5, pp. 359–366, Jan. 1989.
- [60] M. Raissi and G. E. Karniadakis, “Hidden physics models: Machine learning of nonlinear partial differential equations,” *Journal of Computational Physics*, vol. 357, pp. 125–141, Mar. 2018.
- [61] M. Raissi, P. Perdikaris, and G. E. Karniadakis, “Physics-informed neural networks: A deep learning framework for solving forward and inverse problems involving nonlinear partial differential equations,” *Journal of Computational Physics*, vol. 378, pp. 686–707, Feb. 2019.
- [62] L. Sun, H. Gao, S. Pan, and J.-X. Wang, “Surrogate Modeling for Fluid Flows Based on Physics-Constrained Deep Learning Without Simulation Data,” *Computer Methods in Applied Mechanics and Engineering*, vol. 361, p. 112732, Apr. 2020.
- [63] X. Jin, S. Cai, H. Li, and G. E. Karniadakis, “NSFnets (Navier-Stokes Flow nets): Physics-informed neural networks for the incompressible Navier-Stokes equations,” Mar. 2020.
- [64] L. Sun and J.-X. Wang, “Physics-constrained bayesian neural network for fluid flow reconstruction with sparse and noisy data,” *Theoretical and Applied Mechanics Letters*, vol. 10, no. 3, pp. 161–169, Mar. 2020.
- [65] C. Rao, H. Sun, and Y. Liu, “Physics-informed deep learning for incompressible laminar flows,” *Theoretical and Applied Mechanics Letters*, vol. 10, no. 3, pp. 207–212, Mar. 2020.
- [66] M. Rasht-Behesht, C. Huber, K. Shukla, and G. E. Karniadakis, “Physics-informed Neural Networks (PINNs) for Wave Propagation and Full Waveform Inversions,” *Journal of Geophysical Research: Solid Earth*, vol. 127, no. 5, May 2022.
- [67] E. Haghighat, M. Raissi, A. Moure, H. Gomez, and R. Juanes, “A deep learning framework for solution and discovery in solid mechanics,” *arXiv:2003.02751 [cs, stat]*, May 2020.
- [68] —, “A physics-informed deep learning framework for inversion and surrogate modeling in solid mechanics,” *Computer Methods in Applied Mechanics and Engineering*, vol. 379, p. 113741, Jun. 2021.

- [69] C. Rao, H. Sun, and Y. Liu, “Physics-Informed Deep Learning for Computational Elastodynamics without Labeled Data,” *Journal of Engineering Mechanics*, vol. 147, no. 8, p. 04021043, Aug. 2021.
- [70] M. Yin, X. Zheng, J. D. Humphrey, and G. E. Karniadakis, “Non-invasive inference of thrombus material properties with physics-informed neural networks,” *Computer Methods in Applied Mechanics and Engineering*, vol. 375, p. 113603, Mar. 2021.
- [71] G. Kissas, Y. Yang, E. Hwuang, W. R. Witschey, J. A. Detre, and P. Perdikaris, “Machine learning in cardiovascular flows modeling: Predicting arterial blood pressure from non-invasive 4D flow MRI data using physics-informed neural networks,” *Computer Methods in Applied Mechanics and Engineering*, vol. 358, p. 112623, Jan. 2020.
- [72] G.-Y. Li and Y. Cao, “Mechanics of ultrasound elastography,” *Proceedings of the Royal Society A: Mathematical, Physical and Engineering Sciences*, vol. 473, no. 2199, p. 20160841, Mar. 2017.
- [73] Z. Yin, G.-Y. Li, Z. Zhang, Y. Zheng, and Y. Cao, “SWENet: A physics-informed deep neural network (PINN) for shear wave elastography,” *IEEE Transactions on Medical Imaging*, pp. 1–1, 2023.
- [74] M. W. Keller, S. B. Feinstein, and D. D. Watson, “Successful left ventricular opacification following peripheral venous injection of sonicated contrast agent: An experimental evaluation,” *American Heart Journal*, vol. 114, no. 3, pp. 570–575, Sep. 1987.
- [75] K. Wei, A. R. Jayaweera, S. Firoozan, A. Linka, D. M. Skyba, and S. Kaul, “Quantification of Myocardial Blood Flow With Ultrasound-Induced Destruction of Microbubbles Administered as a Constant Venous Infusion,” *Circulation*, vol. 97, no. 5, pp. 473–483, Feb. 1998.
- [76] D. Bardin, T. D. Martz, P. S. Sheeran, R. Shih, P. A. Dayton, and A. P. Lee, “High-speed, clinical-scale microfluidic generation of stable phase-change droplets for gas embolotherapy,” *Lab on a Chip*, vol. 11, no. 23, p. 3990, 2011.
- [77] T. D. Martz, P. S. Sheeran, D. Bardin, A. P. Lee, and P. A. Dayton, “Precision Manufacture of Phase-Change Perfluorocarbon Droplets Using Microfluidics,” *Ultrasound in Medicine & Biology*, vol. 37, no. 11, pp. 1952–1957, Nov. 2011.

- [78] P. Prentice, A. Cuschieri, K. Dholakia, M. Prausnitz, and P. Campbell, “Membrane disruption by optically controlled microbubble cavitation,” *Nature Physics*, vol. 1, no. 2, pp. 107–110, Nov. 2005.
- [79] A. van Wamel, K. Kooiman, M. Hartevelde, M. Emmer, F. J. ten Cate, M. Versluis, and N. de Jong, “Vibrating microbubbles poking individual cells: Drug transfer into cells via sonoporation,” *Journal of Controlled Release*, vol. 112, no. 2, pp. 149–155, May 2006.
- [80] A. J. Dixon, “Enhanced Intracellular Delivery of a Model Drug Using Microbubbles Produced by a Microfluidic Device,” *Ultrasound in Medicine and Biology*, vol. 39, no. 7, p. 10, 2013.
- [81] A. V. Alexandrov, Z. Garami, J. Montaner, and L. A. Moyé, “Ultrasound-Enhanced Systemic Thrombolysis for Acute Ischemic Stroke,” *The New England Journal of Medicine*, p. 9, 2004.
- [82] C. A. Molina, M. Ribo, M. Rubiera, J. Montaner, E. Santamarina, R. Delgado-Mederos, J. F. Arenillas, R. Huertas, F. Purroy, P. Delgado, and J. Alvarez-Sabín, “Microbubble Administration Accelerates Clot Lysis During Continuous 2-MHz Ultrasound Monitoring in Stroke Patients Treated With Intravenous Tissue Plasminogen Activator,” *Stroke*, vol. 37, no. 2, pp. 425–429, Feb. 2006.
- [83] O. A. Berkhemer, P. S. Fransen, D. Beumer, L. A. van den Berg, H. F. Lingsma, A. J. Yoo, W. J. Schonewille, J. A. Vos, P. J. Nederkoorn, M. J. Wermer, M. A. van Walderveen, J. Staals, J. Hofmeijer, J. A. van Oostayen, G. J. Lycklama à Nijeholt, J. Boiten, P. A. Brouwer, B. J. Emmer, S. F. de Bruijn, L. C. van Dijk, L. J. Kappelle, R. H. Lo, E. J. van Dijk, J. de Vries, P. L. de Kort, W. J. J. van Rooij, J. S. van den Berg, B. A. van Hasselt, L. A. Aerden, R. J. Dallinga, M. C. Visser, J. C. Bot, P. C. Vroomen, O. Eshghi, T. H. Schreuder, R. J. Heijboer, K. Keizer, A. V. Tielbeek, H. M. den Hertog, D. G. Gerrits, R. M. van den Berg-Vos, G. B. Karas, E. W. Steyerberg, H. Z. Flach, H. A. Marquering, M. E. Sprengers, S. F. Jenniskens, L. F. Beenen, R. van den Berg, P. J. Koudstaal, W. H. van Zwam, Y. B. Roos, A. van der Lugt, R. J. van Oostenbrugge, C. B. Majoie, and D. W. Dippel, “A Randomized Trial of Intraarterial Treatment for Acute Ischemic Stroke,” *New England Journal of Medicine*, vol. 372, no. 1, pp. 11–20, Jan. 2015.
- [84] T. A. Fritz, E. C. Unger, G. Sutherland, and D. Sahn, “Phase I Clinical Trials of MRX-115: A New Ultrasound Contrast Agent,” *Investigative Radiology*, vol. 32, no. 12, p. 735, Dec. 1997.

- [85] A. L. Klibanov, "Ultrasound Contrast Agents: Development of the Field and Current Status," in *Contrast Agents II: Optical, Ultrasound, X-Ray and Radio-pharmaceutical Imaging*, W. Krause, Ed. Berlin, Heidelberg: Springer, 2002, pp. 73–106.
- [86] M. Emmer, H. J. Vos, D. E. Goertz, A. van Wamel, M. Versluis, and N. de Jong, "Pressure-Dependent Attenuation and Scattering of Phospholipid-Coated Microbubbles at Low Acoustic Pressures," *Ultrasound in Medicine & Biology*, vol. 35, no. 1, pp. 102–111, Jan. 2009.
- [87] D. E. Goertz, N. de Jong, and A. F. van der Steen, "Attenuation and Size Distribution Measurements of Definity™ and Manipulated Definity™ Populations," *Ultrasound in Medicine & Biology*, vol. 33, no. 9, pp. 1376–1388, Sep. 2007.
- [88] J. A. Feshitan, C. C. Chen, J. J. Kwan, and M. A. Borden, "Microbubble size isolation by differential centrifugation," *Journal of Colloid and Interface Science*, vol. 329, no. 2, pp. 316–324, Jan. 2009.
- [89] M. P. Kok, T. Segers, and M. Versluis, "Bubble sorting in pinched microchannels for ultrasound contrast agent enrichment," *Lab on a Chip*, p. 7, 2015.
- [90] T. Segers and M. Versluis, "Acoustic bubble sorting for ultrasound contrast agent enrichment," *Lab Chip*, vol. 14, no. 10, pp. 1705–1714, 2014.
- [91] E. Talu, K. Hettiarachchi, R. L. Powell, A. P. Lee, P. A. Dayton, and M. L. Longo, "Maintaining Monodispersity in a Microbubble Population Formed by Flow-Focusing," *Langmuir*, vol. 24, no. 5, pp. 1745–1749, Mar. 2008.
- [92] J. Choi, J. Feshitan, B. Baseri, Shougang Wang, Yao-Sheng Tung, M. Borden, and E. Konofagou, "Microbubble-Size Dependence of Focused Ultrasound-Induced Blood–Brain Barrier Opening in Mice *In Vivo*," *IEEE Transactions on Biomedical Engineering*, vol. 57, no. 1, pp. 145–154, Jan. 2010.
- [93] S. H. Al-Mutairi, H. A. Nasr-El-Din, A. D. Hill, and A. D. Al-Aamri, "Effect of Droplet Size on the Reaction Kinetics of Emulsified Acid With Calcite," *SPE Journal*, vol. 14, no. 04, pp. 606–616, Dec. 2009.
- [94] W. H. Coulter, "Means for counting particles suspended in a fluid," US Patent US2 656 508A, Oct., 1953.

- [95] S. Gawad, L. Schild, and P. Renaud, "Micromachined impedance spectroscopy flow cytometer for cell analysis and particle sizing," *Lab on a Chip*, vol. 1, no. 1, pp. 76–82, Jan. 2001.
- [96] A. V. Jagtiani, J. Carletta, and J. Zhe, "An impedimetric approach for accurate particle sizing using a microfluidic Coulter counter," *J. Micromech. Microeng.*, p. 11, 2011.
- [97] J. M. R. Rickel, A. J. Dixon, A. L. Klibanov, and J. A. Hossack, "A flow focusing microfluidic device with an integrated Coulter particle counter for production, counting and size characterization of monodisperse microbubbles," *Lab on a Chip*, vol. 18, no. 17, pp. 2653–2664, 2018.
- [98] R. W. DeBlois and C. P. Bean, "Counting and Sizing of Submicron Particles by the Resistive Pulse Technique," *Review of Scientific Instruments*, vol. 41, no. 7, pp. 909–916, Jul. 1970.
- [99] O. A. Saleh and L. L. Sohn, "Quantitative sensing of nanoscale colloids using a microchip Coulter counter," *Review of Scientific Instruments*, vol. 72, no. 12, pp. 4449–4451, Dec. 2001.
- [100] G.-B. Lee, C.-H. Lin, and G.-L. Chang, "Micro flow cytometers with buried SU-8/SOG optical waveguides," *Sensors and Actuators A: Physical*, vol. 103, no. 1-2, pp. 165–170, Jan. 2003.
- [101] E. Miller, M. Rotea, and J. P. Rothstein, "Microfluidic device incorporating closed loop feedback control for uniform and tunable production of micro-droplets," *Lab on a Chip*, vol. 10, no. 10, p. 1293, 2010.
- [102] W. Zeng, S. Li, and Z. Wang, "Closed-loop feedback control of droplet formation in a T-junction microdroplet generator," *Sensors and Actuators A: Physical*, vol. 233, pp. 542–547, Sep. 2015.
- [103] H. Fu, W. Zeng, S. Li, and S. Yuan, "Electrical-detection droplet microfluidic closed-loop control system for precise droplet production," *Sensors and Actuators A: Physical*, vol. 267, pp. 142–149, Nov. 2017.
- [104] S. Gawad, K. Cheung, U. Seger, A. Bertsch, and P. Renaud, "Dielectric spectroscopy in a micromachined flow cytometer: Theoretical and practical considerations," *Lab on a Chip*, vol. 4, no. 3, pp. 241–251, May 2004.

- [105] R. A. Hoffman and W. B. Britt, "Flow-system measurement of cell impedance properties." *Journal of Histochemistry & Cytochemistry*, vol. 27, no. 1, pp. 234–240, Jan. 1979.
- [106] K. Cheung, S. Gawad, and P. Renaud, "Impedance spectroscopy flow cytometry: On-chip label-free cell differentiation," *Cytometry Part A*, vol. 65A, no. 2, pp. 124–132, Jun. 2005.
- [107] J. G. Ziegler and N. B. Nichols, "Optimum Settings for Automatic Controllers," *Journal of Dynamic Systems, Measurement, and Control*, vol. 115, no. 2B, pp. 220–222, Jun. 1993.
- [108] D. R. Roulet, "Pneumatic pressure regulator," US Patent US5 694 965A, Dec., 1997.
- [109] N. Pamme, R. Koyama, and A. Manz, "Counting and sizing of particles and particle agglomerates in a microfluidic device using laser light scattering: Application to a particle-enhanced immunoassay," *Lab on a Chip*, vol. 3, no. 3, p. 187, 2003.
- [110] Q. Xiang, X. Xuan, B. Xu, and D. Li, "Multi-Functional Particle Detection with Embedded Optical Fibers in a Poly(dimethylsiloxane) Chip," *Instrumentation Science & Technology*, vol. 33, no. 5, pp. 597–607, Sep. 2005.
- [111] S. R. Kahn, "The post-thrombotic syndrome," *Hematology: the American Society of Hematology Education Program*, vol. 2016, no. 1, pp. 413–418, Dec. 2016.
- [112] S. D. Grosse, R. E. Nelson, K. A. Nyarko, L. C. Richardson, and G. E. Raskob, "The economic burden of incident venous thromboembolism in the United States: A review of estimated attributable healthcare costs," *Thrombosis research*, vol. 137, p. 3, Jan. 2016.
- [113] A. J. Tomkins, R. J. Hood, C. R. Levi, and N. J. Spratt, "Tissue Plasminogen Activator for preclinical stroke research: Neither "rat" nor "human" dose mimics clinical recanalization in a carotid occlusion model," *Scientific Reports*, vol. 5, p. 16026, Nov. 2015.
- [114] W. Li, C. W. Kessinger, M. Orii, H. Lee, L. Wang, I. Weinberg, M. R. Jaff, G. L. Reed, P. Libby, A. Tawakol, P. K. Henke, and F. A. Jaffer, "Time-Restricted Salutary Effects of Blood Flow Restoration on Venous Thrombosis and Vein Wall Injury in Mouse and Human Subjects," *Circulation*, vol. 143, no. 12, pp. 1224–1238, Mar. 2021.

- [115] R. N. Rys, M. D. Blostein, and C. A. Lemarié, “Deep Vein Thrombosis Induced by Stasis in Mice Monitored by High Frequency Ultrasonography,” *Journal of Visualized Experiments : JoVE*, no. 134, p. 57392, Apr. 2018.
- [116] Z. Wang, Y. Pan, H. Huang, Y. Zhang, Y. Li, C. Zou, G. Huang, Y. Chen, Y. Li, J. Li, and H. Chen, “Enhanced thrombolysis by endovascular low-frequency ultrasound with bifunctional microbubbles in venous thrombosis: In vitro and in vivo study,” *Frontiers in Bioengineering and Biotechnology*, vol. 10, 2022.
- [117] S. Voicu, P. Bonnin, I. Malissin, N. Mohamedi, A. M’Rad, J. M. Ekhérian, L. Sutterlin, G. Naim, T. Lacoste-Palasset, N. Deye, and B. Mégarbane, “Characteristics of deep vein thrombosis in the critically ill COVID-19 patient - an observational cohort study with Doppler ultrasound measurements.” *Eur Rev Med Pharmacol Sci*, pp. 686–694, 2022.
- [118] M.-L. von Brühl, K. Stark, A. Steinhart, S. Chandraratne, I. Konrad, M. Lorenz, A. Khandoga, A. Tirniceriu, R. Coletti, M. Köllnberger, R. A. Byrne, I. Laitinen, A. Walch, A. Brill, S. Pfeiler, D. Manukyan, S. Braun, P. Lange, J. Riegger, J. Ware, A. Eckart, S. Haidari, M. Rudelius, C. Schulz, K. Echtler, V. Brinkmann, M. Schwaiger, K. T. Preissner, D. D. Wagner, N. Mackman, B. Engelmann, and S. Massberg, “Monocytes, neutrophils, and platelets cooperate to initiate and propagate venous thrombosis in mice in vivo,” *The Journal of Experimental Medicine*, vol. 209, no. 4, pp. 819–835, Apr. 2012.
- [119] A. Brill, T. A. Fuchs, A. K. Chauhan, J. J. Yang, S. F. De Meyer, M. Köllnberger, T. W. Wakefield, B. Lämmle, S. Massberg, and D. D. Wagner, “Von Willebrand factor-mediated platelet adhesion is critical for deep vein thrombosis in mouse models,” *Blood*, vol. 117, no. 4, pp. 1400–1407, Jan. 2011.
- [120] M. Okano, T. Hara, M. Nishimori, Y. Irino, K. S. Satomi, M. Shinohara, R. Toh, F. A. Jaffer, T. Ishida, and K.-i. Hirata, “In Vivo Imaging of Venous Thrombus and Pulmonary Embolism Using Novel Murine Venous Thromboembolism Model,” *JACC: Basic to Translational Science*, vol. 5, no. 4, pp. 344–356, Apr. 2020.
- [121] S. A. Shaya, R. J. Westrick, and P. L. Gross, “Thrombus stability explains the factor V Leiden paradox: A mouse model,” *Blood Advances*, vol. 3, no. 21, pp. 3375–3378, Nov. 2019.
- [122] S. A. Shaya, L. J. Saldanha, N. Vaezzadeh, J. Zhou, R. Ni, and P. L. Gross, “Comparison of the effect of dabigatran and dalteparin on thrombus stability

- in a murine model of venous thromboembolism,” *Journal of Thrombosis and Haemostasis*, vol. 14, no. 1, pp. 143–152, Jan. 2016.
- [123] L. Auboire, J.-M. Escoffre, D. Fouan, J.-R. Jacquet, F. Ossant, J.-M. Grégoire, and A. Bouakaz, “Evaluation of high resolution ultrasound as a tool for assessing the 3D volume of blood clots during in vitro thrombolysis,” *Scientific Reports*, vol. 7, p. 6211, Jul. 2017.
- [124] J. Geddings, M. M. Aleman, A. Wolberg, M.-L. von Brühl, S. Massberg, and N. Mackman, “Strengths and weaknesses of a new mouse model of thrombosis induced by inferior vena cava stenosis: Communication from the SSC of the ISTH,” *Journal of Thrombosis and Haemostasis*, vol. 12, no. 4, pp. 571–573, Apr. 2014.
- [125] S. Prakash and N. R. Dhar, “Influence of Electrolytes on the Syneresis and Clotting of Blood,” *The Journal of Physical Chemistry*, vol. 35, no. 2, pp. 629–637, Feb. 1931.
- [126] J. T. Sutton, N. M. Ivancevich, S. R. Perrin, D. C. Vela, and C. K. Holland, “Clot Retraction Affects the Extent of Ultrasound-Enhanced Thrombolysis in an Ex Vivo Porcine Thrombosis Model,” *Ultrasound in Medicine & Biology*, vol. 39, no. 5, pp. 813–824, May 2013.
- [127] E. E. Jansen and M. Hartmann, “Clot Retraction: Cellular Mechanisms and Inhibitors, Measuring Methods, and Clinical Implications,” *Biomedicines*, vol. 9, no. 8, p. 1064, Aug. 2021.
- [128] M. G. Kaul, J. Salamon, T. Knopp, H. Ittrich, G. Adam, H. Weller, and C. Jung, “Magnetic particle imaging for in vivo blood flow velocity measurements in mice,” *Physics in Medicine & Biology*, vol. 63, no. 6, p. 064001, Mar. 2018.
- [129] National Research Council (US) Institute for Laboratory Animal Research, *Guide for the Care and Use of Laboratory Animals*. Washington (DC): National Academies Press (US), 1996.
- [130] G. A. Peyman, C. P. Ingram, L. G. Montilla, and R. S. Witte, “A high-resolution 3D ultrasonic system for rapid evaluation of the anterior and posterior segment,” *Ophthalmic Surgery, Lasers & Imaging: The Official Journal of the International Society for Imaging in the Eye*, vol. 43, no. 2, pp. 143–151, 2012.

- [131] L. Zhu, I. Kolesov, Y. Gao, R. Kikinis, and A. Tannenbaum, “An effective interactive medical image segmentation method using fast growcut,” in *MICCAI Workshop on Interactive Medical Image Computing*, Sep. 2014.
- [132] R. Kikinis, S. D. Pieper, and K. G. Vosburgh, “3D Slicer: A Platform for Subject-Specific Image Analysis, Visualization, and Clinical Support,” in *Intraoperative Imaging and Image-Guided Therapy*, F. A. Jolesz, Ed. New York, NY: Springer, 2014, pp. 277–289.
- [133] J. Puentes, M. Dhibi, L. Bressollette, B. Guias, and B. Solaiman, “Computer-Assisted Venous Thrombosis Volume Quantification,” *IEEE Transactions on Information Technology in Biomedicine*, vol. 13, no. 2, pp. 174–183, Mar. 2009.
- [134] J. Yu, K. Takanari, Y. Hong, K.-W. Lee, N. J. Amoroso, Y. Wang, W. R. Wagner, and K. Kim, “Non-invasive characterization of polyurethane-based tissue constructs in a rat abdominal repair model using high frequency ultrasound elasticity imaging,” *Biomaterials*, vol. 34, no. 11, pp. 2701–2709, Apr. 2013.
- [135] C. D. Ainsworth, C. C. Blake, A. Tamayo, V. Beletsky, A. Fenster, and J. D. Spence, “3D Ultrasound Measurement of Change in Carotid Plaque Volume,” *Stroke*, vol. 36, no. 9, pp. 1904–1909, Sep. 2005.
- [136] A. Landry, J. D. Spence, and A. Fenster, “Quantification of carotid plaque volume measurements using 3D ultrasound imaging,” *Ultrasound in Medicine & Biology*, vol. 31, no. 6, pp. 751–762, Jun. 2005.
- [137] A. Goldberg, P. Pakkiri, E. Dai, A. Lucas, and A. Fenster, “Measurements of aneurysm morphology determined by 3-d micro-ultrasound imaging as potential quantitative biomarkers in a mouse aneurysm model,” *Ultrasound in Medicine & Biology*, vol. 33, no. 10, pp. 1552–1560, Oct. 2007.
- [138] Y. Zhang, H. Xia, Y. Wang, L. Chen, S. Li, I. A. Hussein, Y. Wu, Y. Shang, S. Yao, and R. Du, “The rate of missed diagnosis of lower-limb DVT by ultrasound amounts to 50% or so in patients without symptoms of DVT: A meta-analysis,” *Medicine*, vol. 98, no. 37, p. e17103, Sep. 2019.
- [139] C. Demené, T. Deffieux, M. Pernot, B.-F. Osmanski, V. Biran, J.-L. Gennisson, L.-A. Sieu, A. Bergel, S. Franqui, J.-M. Correias, I. Cohen, O. Baud, and M. Tanter, “Spatiotemporal Clutter Filtering of Ultrafast Ultrasound Data Highly Increases Doppler and fUltrasound Sensitivity,” *IEEE Transactions on Medical Imaging*, vol. 34, no. 11, pp. 2271–2285, Nov. 2015.

- [140] J. Ophir, I. Céspedes, H. Ponnekanti, Y. Yazdi, and X. Li, “Elastography: A quantitative method for imaging the elasticity of biological tissues,” *Ultrasonic Imaging*, vol. 13, no. 2, pp. 111–134, Apr. 1991.
- [141] B. Kainz, M. P. Heinrich, A. Makropoulos, J. Oppenheimer, R. Mandegaran, S. Sankar, C. Deane, S. Mischkewitz, F. Al-Noor, A. C. Rawdin, A. Ruttloff, M. D. Stevenson, P. Klein-Weigel, and N. Curry, “Non-invasive diagnosis of deep vein thrombosis from ultrasound imaging with machine learning,” *npj Digital Medicine*, vol. 4, no. 1, pp. 1–18, Sep. 2021.
- [142] M. Komatsu, A. Sakai, A. Dozen, K. Shozu, S. Yasutomi, H. Machino, K. Asada, S. Kaneko, and R. Hamamoto, “Towards Clinical Application of Artificial Intelligence in Ultrasound Imaging,” *Biomedicines*, vol. 9, no. 7, p. 720, Jul. 2021.
- [143] S. Vijayan, S. Klein, E. F. Hofstad, F. Lindseth, B. Ystgaard, and T. Langø, “Motion tracking in the liver: Validation of a method based on 4D ultrasound using a nonrigid registration technique,” *Medical Physics*, vol. 41, no. 8Part1, p. 082903, 2014.
- [144] F. Bureau, J. Robin, A. Le Ber, W. Lambert, M. Fink, and A. Aubry, “Three-dimensional ultrasound matrix imaging,” *Nature Communications*, vol. 14, no. 1, p. 6793, Oct. 2023.
- [145] K. E. Minges, B. Bikdeli, Y. Wang, R. R. Attaran, and H. M. Krumholz, “National and Regional Trends in Deep Vein Thrombosis Hospitalization Rates, Discharge Disposition, and Outcomes for Medicare Beneficiaries,” *The American Journal of Medicine*, vol. 131, no. 10, pp. 1200–1208, Oct. 2018.
- [146] S. R. Kahn, H. Shbaklo, D. L. Lamping, C. A. Holcroft, I. Shrier, M. J. Miron, A. Roussin, S. Desmarais, F. Joyal, J. Kassis, S. Solymoss, L. Desjardins, M. Johri, and J. S. Ginsberg, “Determinants of health-related quality of life during the 2 years following deep vein thrombosis,” *Journal of Thrombosis and Haemostasis*, vol. 6, no. 7, pp. 1105–1112, Jul. 2008.
- [147] K. T. Delis, D. Bountouroglou, and A. O. Mansfield, “Venous Claudication in Iliofemoral Thrombosis,” *Annals of Surgery*, vol. 239, no. 1, pp. 118–126, Jan. 2004.
- [148] E. D. Avgerinos, E. S. Hager, A. Naddaf, E. Dillavou, M. Singh, and R. A. Chaer, “Outcomes and predictors of failure of thrombolysis for iliofemoral deep venous

- thrombosis,” *Journal of Vascular Surgery: Venous and Lymphatic Disorders*, vol. 3, no. 1, pp. 35–41, Jan. 2015.
- [149] Y. Haig, T. Enden, O. Grøtta, N.-E. Kløw, C.-E. Slagsvold, W. Ghanima, L. Sandvik, G. Hafsahl, P. A. Holme, L. O. Holmen, A. M. Njaaastad, G. Sandbæk, and P. M. Sandset, “Post-thrombotic syndrome after catheter-directed thrombolysis for deep vein thrombosis (CaVenT): 5-year follow-up results of an open-label, randomised controlled trial,” *The Lancet Haematology*, vol. 3, no. 2, pp. e64–e71, Feb. 2016.
- [150] C. Becattini and G. Agnelli, “Acute treatment of venous thromboembolism,” *Blood*, vol. 135, no. 5, pp. 305–316, Jan. 2020.
- [151] J. Hirsh, V. Fuster, J. Ansell, and J. L. Halperin, “American Heart Association/American College of Cardiology Foundation Guide to Warfarin Therapy,” *Circulation*, vol. 107, no. 12, pp. 1692–1711, Apr. 2003.
- [152] S. Schulman, C. Kearon, A. K. Kakkar, S. Schellong, H. Eriksson, D. Baanstra, A. M. Kvanme, J. Friedman, P. Mismetti, and S. Z. Goldhaber, “Extended Use of Dabigatran, Warfarin, or Placebo in Venous Thromboembolism,” *New England Journal of Medicine*, vol. 368, no. 8, pp. 709–718, Feb. 2013.
- [153] J. I. Weitz, A. W. Lensing, M. H. Prins, R. Bauersachs, J. Beyer-Westendorf, H. Bounameaux, T. A. Brighton, A. T. Cohen, B. L. Davidson, H. Decousus, M. C. Freitas, G. Holberg, A. K. Kakkar, L. Haskell, B. van Bellen, A. F. Pap, S. D. Berkowitz, P. Verhamme, P. S. Wells, and P. Prandoni, “Rivaroxaban or Aspirin for Extended Treatment of Venous Thromboembolism,” *New England Journal of Medicine*, vol. 376, no. 13, pp. 1211–1222, Mar. 2017.
- [154] A. Izcovich, J. M. Criniti, F. Popoff, L. Lu, J. Wu, W. Ageno, D. M. Witt, M. R. Jaff, S. Schulman, V. Manja, P. Verhamme, G. Rada, Y. Zhang, R. Nieuwlaat, W. Wiercioch, H. J. Schünemann, and I. Neumann, “Thrombolytics for venous thromboembolic events: A systematic review with meta-analysis,” *Blood Advances*, vol. 4, no. 7, pp. 1539–1553, Apr. 2020.
- [155] M. J. Daley, M. S. Murthy, and E. J. Peterson, “Bleeding risk with systemic thrombolytic therapy for pulmonary embolism: Scope of the problem,” *Therapeutic Advances in Drug Safety*, vol. 6, no. 2, pp. 57–66, Apr. 2015.

- [156] M. Dumantepe, I. A. Tarhan, and A. Ozler, "Treatment of Chronic Deep Vein Thrombosis Using Ultrasound Accelerated Catheter-directed Thrombolysis," *European Journal of Vascular and Endovascular Surgery*, vol. 46, no. 3, pp. 366–371, Sep. 2013.
- [157] S. Z. Goldhaber, E. A. Magnuson, K. M. Chinnakondepalli, D. J. Cohen, and S. Vedantham, "Catheter-directed thrombolysis for deep vein thrombosis: 2021 update," *Vascular Medicine*, vol. 26, no. 6, pp. 662–669, Dec. 2021.
- [158] P. A. Dayton, J. S. Allen, and K. W. Ferrara, "The magnitude of radiation force on ultrasound contrast agents," *The Journal of the Acoustical Society of America*, vol. 112, no. 5, pp. 2183–2192, Nov. 2002.
- [159] Y. Chuang, P. Cheng, and P. Li, "Combining radiation force with cavitation for enhanced sonothrombolysis," *IEEE Transactions on Ultrasonics, Ferroelectrics, and Frequency Control*, vol. 60, no. 1, pp. 97–104, Jan. 2013.
- [160] P. Marmottant and S. Hilgenfeldt, "Controlled vesicle deformation and lysis by single oscillating bubbles," *Nature*, vol. 423, no. 6936, pp. 153–156, May 2003.
- [161] J. Wu, "Theoretical study on shear stress generated by microstreaming surrounding contrast agents attached to living cells," *Ultrasound in Medicine & Biology*, vol. 28, no. 1, pp. 125–129, Jan. 2002.
- [162] C.-D. Ohl, M. Arora, R. Ikink, N. de Jong, M. Versluis, M. Delius, and D. Lohse, "Sonoporation from Jetting Cavitation Bubbles," *Biophysical Journal*, vol. 91, no. 11, pp. 4285–4295, Dec. 2006.
- [163] H. Chen, W. Kreider, A. A. Brayman, M. R. Bailey, and T. J. Matula, "Blood Vessel Deformations on Microsecond Time Scales by Ultrasonic Cavitation," *Physical Review Letters*, vol. 106, no. 3, p. 034301, Jan. 2011.
- [164] K. B. Bader, G. Bouchoux, and C. K. Holland, "Sonothrombolysis," in *Therapeutic Ultrasound*, J.-M. Escoffre and A. Bouakaz, Eds. Cham: Springer International Publishing, 2016, vol. 880, pp. 339–362.
- [165] L. Goel, H. Wu, B. Zhang, J. Kim, P. A. Dayton, Z. Xu, and X. Jiang, "Safety Evaluation of a Forward-Viewing Intravascular Transducer for Sonothrombolysis: An in Vitro and ex Vivo Study," *Ultrasound in Medicine & Biology*, vol. 47, no. 11, pp. 3231–3239, Nov. 2021.

- [166] M. J. Borrelli, W. D. O'Brien, E. Hamilton, M. L. Oelze, J. Wu, L. J. Bernock, S. Tung, H. Rokadia, and W. C. Culp, "Influences of Microbubble Diameter and Ultrasonic Parameters on In Vitro Sonothrombolysis Efficacy," *Journal of Vascular and Interventional Radiology*, vol. 23, no. 12, pp. 1677–1684.e1, Dec. 2012.
- [167] R. P. Engelberger, V. Schroeder, M. Nagler, R. Prince, D. Périard, D. Hayoz, and N. Kucher, "Enhanced Thrombolysis by Ultrasound-Assisted Catheter-Directed Thrombolysis and Microbubbles in an In Vitro Model of Iliofemoral Deep Vein Thrombosis," *Thrombosis and Haemostasis*, vol. 119, no. 07, pp. 1094–1101, Jul. 2019.
- [168] Y. Shi, W. Shi, L. Chen, and J. Gu, "A systematic review of ultrasound-accelerated catheter-directed thrombolysis in the treatment of deep vein thrombosis," *Journal of Thrombosis and Thrombolysis*, vol. 45, no. 3, pp. 440–451, Apr. 2018.
- [169] I. N. Chernysh, C. Nagaswami, S. Kosolapova, A. D. Peshkova, A. Cuker, D. B. Cines, C. L. Cambor, R. I. Litvinov, and J. W. Weisel, "The distinctive structure and composition of arterial and venous thrombi and pulmonary emboli," *Scientific Reports*, vol. 10, no. 1, p. 5112, Mar. 2020.
- [170] G. E. Stocker, J. Shi, K. Ives, A. D. Maxwell, P. A. Dayton, X. Jiang, Z. Xu, and G. E. Owens, "In Vivo Porcine Aged Deep Vein Thrombosis Model for Testing Ultrasound-based Thrombolysis Techniques," *Ultrasound in Medicine & Biology*, vol. 47, no. 12, pp. 3447–3457, Dec. 2021.
- [171] Y. Xie, A. J. Dixon, J. M. R. Rickel, A. L. Klibanov, and J. A. Hossack, "Closed-loop feedback control of microbubble diameter from a flow-focusing microfluidic device," *Biomicrofluidics*, vol. 14, no. 3, p. 034101, May 2020.
- [172] Y. Xie, Y. Huang, H. C. S. Stevenson, L. Yin, K. Zhang, Z. H. Islam, W. A. Marcum, C. Johnston, N. Hoyt, E. W. Kent, B. Wang, and J. A. Hossack, "A Quantitative Method for the Evaluation of Deep Vein Thrombosis in a Murine Model Using Three-Dimensional Ultrasound Imaging," *Biomedicines*, vol. 12, no. 1, p. 200, Jan. 2024.
- [173] P. C. L. Silveira, E. G. Victor, D. Schefer, L. A. Silva, E. L. Streck, M. M. Paula, and R. A. Pinho, "Effects of Therapeutic Pulsed Ultrasound and Dimethylsulfoxide (DMSO) Phonophoresis on Parameters of Oxidative Stress in Traumatized Muscle," *Ultrasound in Medicine & Biology*, vol. 36, no. 1, pp. 44–50, Jan. 2010.

- [174] P. E. Huber and P. Pfisterer, "In vitro and in vivo transfection of plasmid DNA in the Dunning prostate tumor R3327-AT1 is enhanced by focused ultrasound," *Gene Therapy*, vol. 7, no. 17, pp. 1516–1525, Sep. 2000.
- [175] A. J. Comerota, C. Oostra, Z. Fayad, W. Gunning, P. Henke, C. Luke, A. Lynn, and F. Lurie, "A histological and functional description of the tissue causing chronic postthrombotic venous obstruction," *Thrombosis Research*, vol. 135, no. 5, pp. 882–887, May 2015.
- [176] A. Dickhout, P. Van de Vijver, N. Bitsch, S. J. van Hoof, S. L. G. D. Thomassen, S. Massberg, P. Timmerman, F. Verhaegen, R. R. Koenen, I. Dijkgraaf, and T. M. Hackeng, "Molecular Detection of Venous Thrombosis in Mouse Models Using SPECT/CT," *Biomolecules*, vol. 12, no. 6, p. 829, Jun. 2022.
- [177] W.-Y. Shi, S. Wu, L.-Y. Hu, C.-J. Liu, and J.-P. Gu, "Swine Model of Thrombotic Caval Occlusion Created by Autologous Thrombus Injection with Assistance of Intra-caval Net Knitting," *Scientific Reports*, vol. 5, no. 1, p. 18546, Dec. 2015.
- [178] J. I. Weitz and N. C. Chan, "Novel antithrombotic strategies for treatment of venous thromboembolism," *Blood*, vol. 135, no. 5, pp. 351–359, Jan. 2020.
- [179] C. W. Kessinger, J. W. Kim, P. K. Henke, B. Thompson, J. R. McCarthy, T. Hara, M. Sillesen, R. J. P. Margey, P. Libby, R. Weissleder, C. P. Lin, and F. A. Jaffer, "Statins Improve the Resolution of Established Murine Venous Thrombosis: Reductions in Thrombus Burden and Vein Wall Scarring," *PLOS ONE*, vol. 10, no. 2, p. e0116621, Feb. 2015.
- [180] A. S. Nathan and J. Giri, "Reexamining the Open-Vein Hypothesis for Acute Deep Venous Thrombosis," *Circulation*, vol. 139, no. 9, pp. 1174–1176, Feb. 2019.
- [181] J. A. Diaz, P. Saha, B. Cooley, O. R. Palmer, S. P. Grover, N. Mackman, T. W. Wakefield, P. K. Henke, A. Smith, and B. K. Lal, "Choosing a Mouse Model of Venous Thrombosis," *Arteriosclerosis, Thrombosis, and Vascular Biology*, vol. 39, no. 3, pp. 311–318, Mar. 2019.
- [182] I. Singh, K. Burnand, M. Collins, A. Luttun, D. Collen, B. Boelhouwer, and A. Smith, "Failure of Thrombus to Resolve in Urokinase-Type Plasminogen Activator Gene–Knockout Mice," *Circulation*, vol. 107, no. 6, pp. 869–875, Feb. 2003.

- [183] J. Humphries, J. A. Gossage, B. Modarai, K. G. Burnand, T. H. Sisson, C. Murdoch, and A. Smith, “Monocyte urokinase-type plasminogen activator up-regulation reduces thrombus size in a model of venous thrombosis,” *Journal of Vascular Surgery*, vol. 50, no. 5, pp. 1127–1134, Nov. 2009.
- [184] A. Alonso, C.-E. Dempfle, A. Della Martina, M. Stroick, M. Fatar, K. Zohsel, E. Allémann, M. G. Hennerici, and S. Meairs, “In vivo clot lysis of human thrombus with intravenous abciximab immunobubbles and ultrasound,” *Thrombosis Research*, vol. 124, no. 1, pp. 70–74, May 2009.
- [185] X. Wang, C. E. Hagemeyer, J. D. Hohmann, E. Leitner, P. C. Armstrong, F. Jia, M. Olschewski, A. Needles, K. Peter, and I. Ahrens, “Novel Single-Chain Antibody-Targeted Microbubbles for Molecular Ultrasound Imaging of Thrombosis,” *Circulation*, vol. 125, no. 25, pp. 3117–3126, Jun. 2012.
- [186] P. Prathipati, C. Rodriguez-Aguayo, B. L. Walton, A. K. Sood, J. Greaver, C. F. Janssen, and G. Lopez-Berestein, “A Retrospective Analysis for Different Routes of Administration in Mice-Percutaneous Retro-Orbital, Jugular Catheter, Tail Vein and Femoral Cut Down Injections,” *Journal of Biosciences and Medicines*, vol. 08, no. 09, p. 131, Sep. 2020.
- [187] B. Zhang, H. Wu, H. Kim, P. J. Welch, A. Cornett, G. Stocker, R. G. Nogueira, J. Kim, G. Owens, P. A. Dayton, Z. Xu, C. Shi, and X. Jiang, “A Model of High-Speed Endovascular Sonothrombolysis with Vortex Ultrasound-Induced Shear Stress to Treat Cerebral Venous Sinus Thrombosis,” *Research*, vol. 6, p. 0048, Feb. 2023.
- [188] H. Kim, B. Zhang, H. Wu, J. Yao, C. Shi, and X. Jiang, “Vortex-ultrasound for microbubble-mediated thrombolysis of retracted clots,” *Applied Physics Letters*, vol. 123, no. 7, p. 073701, Aug. 2023.
- [189] P. Li, W. Huang, J. Xu, W. Shao, and Y. Cui, “Efficacy Estimation of Microbubble-Assisted Local Sonothrombolysis Using a Catheter with a Series of Miniature Transducers,” *Micromachines*, vol. 12, no. 6, p. 612, Jun. 2021.
- [190] M. Kuliha, M. Roubec, T. Jonszta, J. Krajča, D. Czerny, A. Krajina, K. Langová, R. Herzig, V. Procházka, and D. Školoudfk, “Safety and Efficacy of Endovascular Sonolysis Using the EkoSonic Endovascular System in Patients with Acute Stroke,” *American Journal of Neuroradiology*, vol. 34, no. 7, pp. 1401–1406, Jul. 2013.

- [191] A. M. Handorf, Y. Zhou, M. A. Halanski, and W.-J. Li, “Tissue Stiffness Dictates Development, Homeostasis, and Disease Progression,” *Organogenesis*, vol. 11, no. 1, pp. 1–15, Apr. 2015.
- [192] P. Santini, G. Esposto, M. E. Ainora, A. Lupascu, A. Gasbarrini, M. A. Zocco, and R. Pola, “Ultrasound Elastography to Assess Age of Deep Vein Thrombosis: A Systematic Review,” *Diagnostics*, vol. 13, no. 12, p. 2075, Jan. 2023.
- [193] Y. E. Almalki, M. G. E.-D. Mansour, S. A. Ali, M. A. A. Basha, M. M. Abdelkawi, S. K. Alduraibi, Z. A. Almushayti, A. S. Aldhilan, M. Aboualkheir, D. Amin, M. Metkees, A. M. A. Basha, and N. Y. Ebaid, “Advanced strain elastography is a reliable approach for prostate cancer detection in patients with elevated PSA levels,” *Scientific Reports*, vol. 14, no. 1, p. 2917, Feb. 2024.
- [194] J. Carlsen, C. Ewertsen, S. Sletting, I. Vejborg, F. K. W. Schäfer, D. Cosgrove, and M. B. Nielsen, “Ultrasound Elastography in Breast Cancer Diagnosis,” *Ultraschall in der Medizin - European Journal of Ultrasound*, vol. 36, no. 6, pp. 550–565, Dec. 2015.
- [195] T. Faruk, M. K. Islam, S. Arefin, and M. Z. Haq, “The Journey of Elastography: Background, Current Status, and Future Possibilities in Breast Cancer Diagnosis,” *Clinical Breast Cancer*, vol. 15, no. 5, pp. 313–324, Oct. 2015.
- [196] J. Ding, H. Cheng, C. Ning, J. Huang, and Y. Zhang, “Quantitative Measurement for Thyroid Cancer Characterization Based on Elastography,” *Journal of Ultrasound in Medicine*, vol. 30, no. 9, pp. 1259–1266, 2011.
- [197] G. Azizi, J. M. Keller, M. L. Mayo, K. Piper, D. Puett, K. M. Earp, and C. D. Malchoff, “Thyroid Nodules and Shear Wave Elastography: A New Tool in Thyroid Cancer Detection,” *Ultrasound in Medicine & Biology*, vol. 41, no. 11, pp. 2855–2865, Nov. 2015.
- [198] N. Frulio and H. Trillaud, “Ultrasound elastography in liver,” *Diagnostic and Interventional Imaging*, vol. 94, no. 5, pp. 515–534, May 2013.
- [199] R. G. Barr, “Shear wave liver elastography,” *Abdominal Radiology*, vol. 43, no. 4, pp. 800–807, Apr. 2018.
- [200] M. Tanter, J. Bercoff, L. Sandrin, and M. Fink, “Ultrafast compound imaging for 2-D motion vector estimation: Application to transient elastography,” *IEEE Transactions on Ultrasonics, Ferroelectrics, and Frequency Control*, vol. 49, no. 10, pp. 1363–1374, Oct. 2002.

- [201] L. Sandrin, B. Fourquet, J.-M. Hasquenoph, S. Yon, C. Fournier, F. Mal, C. Christidis, M. Ziol, B. Poulet, F. Kazemi, M. Beaugrand, and R. Palau, "Transient elastography: A new noninvasive method for assessment of hepatic fibrosis," *Ultrasound in Medicine and Biology*, vol. 29, no. 12, pp. 1705–1713, Dec. 2003.
- [202] K. R. Nightingale, M. L. Palmeri, R. W. Nightingale, and G. E. Trahey, "On the feasibility of remote palpation using acoustic radiation force," *The Journal of the Acoustical Society of America*, vol. 110, no. 1, pp. 625–634, Jul. 2001.
- [203] J. Bercoff, M. Tanter, and M. Fink, "Supersonic shear imaging: A new technique for soft tissue elasticity mapping," *IEEE Transactions on Ultrasonics, Ferroelectrics, and Frequency Control*, vol. 51, no. 4, pp. 396–409, Apr. 2004.
- [204] M. Tanter, J. Bercoff, A. Athanasiou, T. Defieux, J.-L. Gennisson, G. Montaldo, M. Muller, A. Tardivon, and M. Fink, "Quantitative Assessment of Breast Lesion Viscoelasticity: Initial Clinical Results Using Supersonic Shear Imaging," *Ultrasound in Medicine and Biology*, vol. 34, no. 9, pp. 1373–1386, Sep. 2008.
- [205] P. Song, H. Zhao, A. Manduca, M. W. Urban, J. F. Greenleaf, and S. Chen, "Comb-push ultrasound shear elastography (CUSE): A novel method for two-dimensional shear elasticity imaging of soft tissues," *IEEE transactions on medical imaging*, vol. 31, no. 9, pp. 1821–1832, 2012.
- [206] P. Song, M. W. Urban, A. Manduca, H. Zhao, J. F. Greenleaf, and S. Chen, "Comb-Push Ultrasound Shear Elastography (CUSE) With Various Ultrasound Push Beams," *IEEE Transactions on Medical Imaging*, vol. 32, no. 8, pp. 1435–1447, Aug. 2013.
- [207] P. Song, M. C. Macdonald, R. H. Behler, J. D. Lanning, M. H. Wang, M. W. Urban, A. Manduca, H. Zhao, M. R. Callstrom, A. Alizad, J. F. Greenleaf, and S. Chen, "Two-dimensional shear-wave elastography on conventional ultrasound scanners with time-aligned sequential tracking (TAST) and comb-push ultrasound shear elastography (CUSE)," *IEEE Transactions on Ultrasonics, Ferroelectrics, and Frequency Control*, vol. 62, no. 2, pp. 290–302, Feb. 2015.
- [208] M. Bruce, O. Kolokythas, G. Ferraioli, C. Filice, and M. O'Donnell, "Limitations and artifacts in shear-wave elastography of the liver," *Biomedical Engineering Letters*, vol. 7, no. 2, pp. 81–89, May 2017.

- [209] M. Palmeri, M. Wang, J. Dahl, K. Frinkley, and K. Nightingale, “Quantifying Hepatic Shear Modulus In Vivo Using Acoustic Radiation Force,” *Ultrasound in Medicine & Biology*, vol. 34, no. 4, pp. 546–558, Apr. 2008.
- [210] S. Ahmed, U. Kamal, and M. K. Hasan, “DSWE-Net: A deep learning approach for shear wave elastography and lesion segmentation using single push acoustic radiation force,” *Ultrasonics*, vol. 110, p. 106283, Feb. 2021.
- [211] X. Chen, N. Chennakeshava, R. Wildeboer, M. Misch, and R. J. G. van Sloun, “Shear-Wave Particle-Velocity Estimation and Enhancement Using a Multi-Resolution Convolutional Neural Network,” *Ultrasound in Medicine & Biology*, vol. 49, no. 7, pp. 1518–1526, Jul. 2023.
- [212] R. G. Barr, “Future of breast elastography,” *Ultrasonography*, vol. 38, no. 2, pp. 93–105, Apr. 2019.
- [213] A. Voulodimos, N. Doulamis, A. Doulamis, and E. Protopapadakis, “Deep Learning for Computer Vision: A Brief Review,” *Computational Intelligence and Neuroscience*, vol. 2018, pp. 1–13, 2018.
- [214] A. Esteva, K. Chou, S. Yeung, N. Naik, A. Madani, A. Mottaghi, Y. Liu, E. Topol, J. Dean, and R. Socher, “Deep learning-enabled medical computer vision,” *npj Digital Medicine*, vol. 4, no. 1, pp. 1–9, Jan. 2021.
- [215] K. R. Chowdhary, “Natural Language Processing,” in *Fundamentals of Artificial Intelligence*, K. Chowdhary, Ed. New Delhi: Springer India, 2020, pp. 603–649.
- [216] W. X. Zhao, K. Zhou, J. Li, T. Tang, X. Wang, Y. Hou, Y. Min, B. Zhang, J. Zhang, Z. Dong, Y. Du, C. Yang, Y. Chen, Z. Chen, J. Jiang, R. Ren, Y. Li, X. Tang, Z. Liu, P. Liu, J.-Y. Nie, and J.-R. Wen, “A Survey of Large Language Models,” Nov. 2023.
- [217] A. G. Baydin, B. A. Pearlmutter, A. A. Radul, and J. M. Siskind, “Automatic differentiation in machine learning: A survey,” *Journal of Machine Learning Research*, vol. 18, 2020.
- [218] L. Wang, H. Wang, L. Liang, J. Li, Z. Zeng, and Y. Liu, “Physics-informed neural networks for transcranial ultrasound wave propagation,” *Ultrasonics*, vol. 132, p. 107026, Jul. 2023.

- [219] L. Wang, J. Li, S. Chen, Z. Fan, Z. Zeng, and Y. Liu, “Finite difference-embedded UNet for solving transcranial ultrasound frequency-domain wavefield,” *The Journal of the Acoustical Society of America*, vol. 155, no. 3, pp. 2257–2269, Mar. 2024.
- [220] A. Mallampati and M. Almekkawy, “Measuring Tissue Elastic Properties Using Physics Based Neural Networks,” in *2021 IEEE UFFC Latin America Ultrasonics Symposium (LAUS)*, Oct. 2021, pp. 1–4.
- [221] M. L. Palmeri, B. Qiang, S. Chen, and M. W. Urban, “Guidelines for Finite-Element Modeling of Acoustic Radiation Force-Induced Shear Wave Propagation in Tissue-Mimicking Media,” *IEEE Transactions on Ultrasonics, Ferroelectrics, and Frequency Control*, vol. 64, no. 1, pp. 78–92, Jan. 2017.
- [222] E. Zhang, M. Yin, and G. E. Karniadakis, “Physics-Informed Neural Networks for Nonhomogeneous Material Identification in Elasticity Imaging,” *arXiv:2009.04525 [cond-mat]*, Sep. 2020.
- [223] M. Liu, L. Liang, and W. Sun, “A generic physics-informed neural network-based constitutive model for soft biological tissues,” *Computer Methods in Applied Mechanics and Engineering*, vol. 372, p. 113402, Dec. 2020.
- [224] V. Tac, V. D. Sree, M. K. Rausch, and A. B. Tepole, “Data-driven modeling of the mechanical behavior of anisotropic soft biological tissue,” *Engineering with Computers*, vol. 38, no. 5, pp. 4167–4182, Oct. 2022.
- [225] S. Thakur, M. Raissi, and A. M. Ardekani, “ViscoelasticNet: A physics informed neural network framework for stress discovery and model selection,” Sep. 2022.
- [226] Y. Cao, Z. Fang, Y. Wu, D.-X. Zhou, and Q. Gu, “Towards Understanding the Spectral Bias of Deep Learning,” Oct. 2020.
- [227] N. Rahaman, A. Baratin, D. Arpit, F. Draxler, M. Lin, F. Hamprecht, Y. Bengio, and A. Courville, “On the Spectral Bias of Neural Networks,” in *Proceedings of the 36th International Conference on Machine Learning*. PMLR, May 2019, pp. 5301–5310.
- [228] R. Basri, D. Jacobs, Y. Kasten, and S. Kritchman, “The convergence rate of neural networks for learned functions of different frequencies,” in *Proceedings of the 33rd International Conference on Neural Information Processing Systems*. Red Hook, NY, USA: Curran Associates Inc., Dec. 2019, no. 428, pp. 4761–4771.

- [229] S. Wang, X. Yu, and P. Perdikaris, “When and why PINNs fail to train: A neural tangent kernel perspective,” *Journal of Computational Physics*, vol. 449, p. 110768, Jan. 2022.
- [230] S. Wang, H. Wang, and P. Perdikaris, “On the eigenvector bias of Fourier feature networks: From regression to solving multi-scale PDEs with physics-informed neural networks,” *Computer Methods in Applied Mechanics and Engineering*, vol. 384, p. 113938, Oct. 2021.
- [231] M. Raissi, P. Perdikaris, and G. E. Karniadakis, “Physics Informed Deep Learning (Part I): Data-driven Solutions of Nonlinear Partial Differential Equations,” *arXiv:1711.10561 [cs, math, stat]*, Nov. 2017.
- [232] ———, “Physics Informed Deep Learning (Part II): Data-driven Discovery of Nonlinear Partial Differential Equations,” *arXiv:1711.10566 [cs, math, stat]*, Nov. 2017.
- [233] A. M. Elmeliegy and M. N. Guddati, “Correlation-based full-waveform shear wave elastography,” *Physics in Medicine & Biology*, vol. 68, no. 11, p. 115001, May 2023.
- [234] A. Nordez and F. Hug, “Muscle shear elastic modulus measured using supersonic shear imaging is highly related to muscle activity level,” *Journal of Applied Physiology*, vol. 108, no. 5, pp. 1389–1394, May 2010.
- [235] H. Liebgott, A. Rodriguez-Molares, F. Cervenansky, J. Jensen, and O. Bernard, “Plane-Wave Imaging Challenge in Medical Ultrasound,” in *2016 IEEE International Ultrasonics Symposium (IUS)*, Sep. 2016, pp. 1–4.
- [236] J.-Y. Lu, P.-Y. Lee, and C.-C. Huang, “Improving Image Quality for Single-Angle Plane Wave Ultrasound Imaging With Convolutional Neural Network Beamformer,” *IEEE Transactions on Ultrasonics, Ferroelectrics, and Frequency Control*, vol. 69, no. 4, pp. 1326–1336, Apr. 2022.
- [237] D. Y. Chan, D. C. Morris, T. J. Polascik, M. L. Palmeri, and K. R. Nightingale, “Deep Convolutional Neural Networks for Displacement Estimation in ARFI Imaging,” *IEEE Transactions on Ultrasonics, Ferroelectrics, and Frequency Control*, vol. 68, no. 7, pp. 2472–2481, Jul. 2021.
- [238] T. Loupas, J. Powers, and R. Gill, “An axial velocity estimator for ultrasound blood flow imaging, based on a full evaluation of the Doppler equation by means

- of a two-dimensional autocorrelation approach,” *IEEE Transactions on Ultrasonics, Ferroelectrics, and Frequency Control*, vol. 42, no. 4, pp. 672–688, Jul. 1995.
- [239] P. Song, A. Manduca, H. Zhao, M. W. Urban, J. F. Greenleaf, and S. Chen, “Fast Shear Compounding Using Robust Two-dimensional Shear Wave Speed Calculation and Multi-directional Filtering,” *Ultrasound in medicine & biology*, vol. 40, no. 6, pp. 1343–1355, Jun. 2014.
- [240] I. Acerbi, L. Cassereau, I. Dean, Q. Shi, A. Au, C. Park, Y. Y. Chen, J. Liphardt, E. S. Hwang, and V. M. Weaver, “Human breast cancer invasion and aggression correlates with ECM stiffening and immune cell infiltration,” *Integrative Biology*, vol. 7, no. 10, pp. 1120–1134, Oct. 2015.
- [241] S. Mueller and L. Sandrin, “Liver stiffness: A novel parameter for the diagnosis of liver disease,” *Hepatic Medicine: Evidence and Research*, vol. 2, pp. 49–67, May 2010.
- [242] M. Tancik, P. P. Srinivasan, B. Mildenhall, S. Fridovich-Keil, N. Raghavan, U. Singhal, R. Ramamoorthi, J. T. Barron, and R. Ng, “Fourier Features Let Networks Learn High Frequency Functions in Low Dimensional Domains,” Jun. 2020.
- [243] H. Naganuma, H. Ishida, A. Uno, H. Nagai, H. Kuroda, and M. Ogawa, “Diagnostic problems in two-dimensional shear wave elastography of the liver,” *World Journal of Radiology*, vol. 12, no. 5, pp. 76–86, May 2020.
- [244] H. Gao, L. Sun, and J.-X. Wang, “Super-resolution and denoising of fluid flow using physics-informed convolutional neural networks without high-resolution labels,” *Physics of Fluids*, vol. 33, no. 7, p. 073603, Jul. 2021.
- [245] E. Ferdian, D. Marlevi, J. Schollenberger, M. Aristova, E. R. Edelman, S. Schnell, C. A. Figueroa, D. A. Nordsletten, and A. A. Young, “Cerebrovascular super-resolution 4D Flow MRI – using deep learning to non-invasively quantify velocity, flow, and relative pressure,” p. 2021.08.25.457611, Aug. 2021.
- [246] P. Kijanka and M. W. Urban, “Local Phase Velocity Based Imaging: A New Technique Used for Ultrasound Shear Wave Elastography,” *IEEE Transactions on Medical Imaging*, vol. 38, no. 4, pp. 894–908, Apr. 2019.

- [247] K. Shukla, A. D. Jagtap, and G. E. Karniadakis, “Parallel physics-informed neural networks via domain decomposition,” *Journal of Computational Physics*, vol. 447, p. 110683, Dec. 2021.
- [248] H. Guan, J. Dong, and W.-N. Lee, “Towards Real-time Training of Physics-informed Neural Networks: Applications in Ultrafast Ultrasound Blood Flow Imaging,” Sep. 2023.
- [249] J. Song, C. Meng, and S. Ermon, “Denoising Diffusion Implicit Models,” Oct. 2022.
- [250] A. Kazerouni, E. K. Aghdam, M. Heidari, R. Azad, M. Fayyaz, I. Hacihaliloglu, and D. Merhof, “Diffusion models in medical imaging: A comprehensive survey,” *Medical Image Analysis*, vol. 88, p. 102846, Aug. 2023.
- [251] B. Song, S. M. Kwon, Z. Zhang, X. Hu, Q. Qu, and L. Shen, “Solving Inverse Problems with Latent Diffusion Models via Hard Data Consistency,” Apr. 2024.
- [252] J. Hurley, “Sizing Particles with a Coulter Counter,” *Biophysical Journal*, vol. 10, no. 1, pp. 74–79, Jan. 1970.
- [253] J. Xu, A. Salari, Y. Wang, X. He, L. Kerr, A. Darbandi, A. C. de Leon, A. A. Exner, M. C. Kolios, D. Yuen, and S. S. H. Tsai, “Microfluidic Generation of Monodisperse Nanobubbles by Selective Gas Dissolution,” *Small (Weinheim an Der Bergstrasse, Germany)*, vol. 17, no. 20, p. e2100345, May 2021.
- [254] A. A. Paknahad, I. O. Zalloum, R. Karshafian, M. C. Kolios, and S. S. H. Tsai, “High throughput microfluidic nanobubble generation by microporous membrane integration and controlled bubble shrinkage,” *Journal of Colloid and Interface Science*, vol. 653, pp. 277–284, Jan. 2024.
- [255] F. Nazly Pirmoradi, J. K. Jackson, H. M. Burt, and M. Chiao, “On-demand controlled release of docetaxel from a battery-less MEMS drug delivery device,” *Lab on a Chip*, vol. 11, no. 16, pp. 2744–2752, 2011.
- [256] R. Bam, A. Natarajan, F. Tabesh, R. Paulmurugan, and J. J. Dahl, “Synthesis and Evaluation of Clinically Translatable Targeted Microbubbles Using a Microfluidic Device for In Vivo Ultrasound Molecular Imaging,” *International Journal of Molecular Sciences*, vol. 24, no. 10, p. 9048, Jan. 2023.

- [257] A. Rayes, J. Zhang, G. Lu, X. Qian, S. T. Schroff, R. Ryu, X. Jiang, and Q. Zhou, “Estimating Thrombus Elasticity by Shear Wave Elastography to Evaluate Ultrasound Thrombolysis for Thrombus With Different Stiffness,” *IEEE Transactions on Biomedical Engineering*, vol. 70, no. 1, pp. 135–143, Jan. 2023.
- [258] C. Czaplicki, H. Albadawi, S. Partovi, R. T. Gandhi, K. Quencer, A. R. Deipolyi, and R. Oklu, “Can thrombus age guide thrombolytic therapy?” *Cardiovascular Diagnosis and Therapy*, vol. 7, no. Suppl 3, pp. S186–S196, Dec. 2017.
- [259] J. Ho, A. Jain, and P. Abbeel, “Denoising Diffusion Probabilistic Models,” in *Advances in Neural Information Processing Systems*, vol. 33. Curran Associates, Inc., 2020, pp. 6840–6851.
- [260] J. Liu, R. Anirudh, J. J. Thiagarajan, S. He, K. A. Mohan, U. S. Kamilov, and H. Kim, “DOLCE: A Model-Based Probabilistic Diffusion Framework for Limited-Angle CT Reconstruction,” in *Proceedings of the IEEE/CVF International Conference on Computer Vision*, 2023, pp. 10 498–10 508.
- [261] D. Shu, Z. Li, and A. Barati Farimani, “A physics-informed diffusion model for high-fidelity flow field reconstruction,” *Journal of Computational Physics*, vol. 478, p. 111972, Apr. 2023.
- [262] J.-H. Bastek, W. Sun, and D. M. Kochmann, “Physics-Informed Diffusion Models,” May 2024.